ABSTRACT

Title of dissertation: LAYER PEELING/ADDING ALGORITHM AND COMPLEX WAVEGUIDE BRAGG GRATING FOR ANY SPECTRUM GENERATION & FIBER-TO-WAVEGUIDE COUPLER WITH ULTRA HIGH COUPLING EFFICIENCY

Tiecheng Zhu, Doctor of Philosophy, 2016

Dissertation directed by: Professor Mario Dagenais
Department of Electrical and Computer Engineering

Part I: Layer Peeling/Adding Algorithm and Complex Waveguide Bragg Grating For Any Spectrum Generation

A Layer Peeling/Adding algorithm for designing optical filters is not only developed theoretically but also demonstrated experimentally. Unlike the conventional design approaches which can handle only limited spectral profiles, the algorithm presented here is capable of generating transmission/reflection spectrum of any shape. As a proof of demonstration, Complex Waveguide Bragg Gratings (CWBG) are designed, fabricated and characterized using the algorithm. The CWBG, which is implemented as a single-mode Si_3N_4/SiO_2 waveguide grating with aperiodic varying waveguide widths, is capable of removing a large number of randomly-distributed

wavelengths simultaneously. Two generations of CWBGs are designed and fabricated to remove 20 and 47 notches respectively, with spectral precision better than ± 0.1 nm, suppression ratios larger than 15 dB, and 3-dB widths of 0.3 nm. Among CWBG's various potential applications, we highlight its use for eliminating the multiple OH emission lines from the Earth's atmosphere for ground-based astronomical observations.

Part II: Fiber-to-Waveguide Coupler With Ultra High Coupling Efficiency

An easy-to-fabricate but very efficient fiber-to-waveguide coupler is theoretically analyzed and experimentally demonstrated. In this design, light from a single-mode UHNA3 fiber can be butt-coupled into a single-mode high-index-contrast Si_3N_4/SiO_2 waveguide with a measured coupling efficiency of 96 % at the wavelength of 1550 nm, and > 90 % in the spectral range from 1450 nm to 1650 nm. Large horizontal and vertical alignment tolerances of 3.8 μm and 3.6 μm respectively are obtained between the fiber and the waveguide coupler. Coupling efficiencies are also characterized using Si_3N_4/SiO_2 waveguides and both SMF28 fiber and SM1500G80 fiber. All these experimental results agree well with simulations. The waveguide coupler also features ease of end-facet cleaving, and can be used in ultra-broadband high coupling efficiency applications.

Layer Peeling/Adding Algorithm and Complex Waveguide Bragg Grating For Any Spectrum Generation
&
Fiber-to-Waveguide Coupler With Ultra High Coupling Efficiency

by

Tiecheng Zhu

Dissertation submitted to the Faculty of the Graduate School of the
University of Maryland, College Park in partial fulfillment
of the requirements for the degree of
Doctor of Philosophy
2016

Advisory Committee:
Professor Mario Dagenais, Chair/Advisor
Professor Sylvain Veilleux, Co-Advisor
Professor Chris Davis
Professor Martin Peckerar
Professor Thomas Murphy

Acknowledgments

First of all, I would like to give thanks to my advisors Prof. Mario Dagenais and Prof. Sylvain Veilleux. Without your support and guidance, I might never have the opportunity to fully explore this fundamental problem of filters and couplers. Without your encouragements and fruitful discussions, I could still be trapped somewhere in the middle of the algorithm.

I can still remember the spring of 2010, when I was then just an undergraduate exchange student to University of Maryland from City University of Hong Kong. During that semester I took the course ENEE496 taught by Prof. Dagenais, who is truly a gentlemen. This course contained both solid mathematical equations and interesting physics intuitions, and they really fascinated me. By the end of that semester, I made an important decision that I should chase for a Ph.D. degree under the guidance of Prof. Dagenais. That goal became reality in the fall of 2011, and I finally became a Ph.D. student at University of Maryland, one of my dream schools. Even in a few years later, sometimes when Prof. Dagenais introduced me to someone new, he would still mention me as the best student in his ENEE496 class. I will not forget his recognition.

University of Maryland is a great place to conduct research, as it has so many well-known scholars, one of the best fabrication facilities, and also a large amount of resources/national laboratories in the Washington DC area. It is definitely the best engineering school in the Greater Washington DC area. I was really honored to be a Ph.D. student in such a good university.

For my research project I am funded by the W. M. Keck Foundation, again without this financial support I would not be able to devote myself fully on the project.

Also as a member in this Keck Photonic Spectrometer (KPS) project, I wish to thank all of our collaborators: Prof. Joss Bland-Hawthorn from University of Sydney, Prof. Stuart Vogel and Prof. Andy Harris from Department of Astronomy, University of Maryland, Dr. Neil Gehrels from NASA, and Dr. John Mather from NASA, who is the 2006 Nobel Laureate in Physics. The reason why this project has been successful so far is because we stand on the shoulders of the giants in the world. The strong collaboration is simply awesome.

Moreover, I want to thank Jim O'Connor, Jonathan A. Hummel, Tom Loughran, John Abrahams and Mark Lecates from the Nano-Fabrication Lab at University of Maryland, for their generous help in my nano-fabrication experiments. I also benefited a lot of help with machining from Jay Pyle, who is a senior and friendly staff from the IREAP Machine Shop. I need to give thanks to Vincent Brulis from Photon Design, for the discussions on using FIMMWAVE / FIMMPROP, and also to Dr. Kevin Burcham from Raith, for his professsional advice on the waveguide Bragg grating patterning using e-beam lithography.

There are also many really friendly colleagues in my group. I want to especially thank my former colleagues Jeyran Amirloo and Guenmin Ryu, who taught me everything about nano-technology fabrications during my first and second year. I also like to give thanks Yiwen Hu, Feifei Chen, Vicki Toy, and Pradip Gatkine for the good research work that we have done together, and also to Tian Li, Yang

Meng, Yang Zhang, Yangyi Yao, Wei-Lun Hsu, Shengjie Xie, Jiahao Zhan, Shahriar Aghaei, Dakang Ma and Daimeng Zhang, for their help and discussions when I encountered problems.

As the only child in the family, I really owe a lot to my parents and my family. I am really proud that I could have a big and happy family both in the city of Ningbo and in the city of Silver Spring in China. However, because of the confidentiality and high sensitivity of my research area, it is very difficult for me to go back for visit during the past five years. I could not go back even when my most beloved aunt passed away. I do wish that I could afford more time with my parents and my big family in the future.

Finally, I would like to thank my wife, Shiyuan (Emma) Fu, for her complete support and sacrifice for my research. We met each other in the campus gospel meeting in University of Maryland in 2012. The most amazing thing is that no matter what happens, there will never be any arguing or temper between us. Emma simply takes care of everything at home, so I am able to fully concentrate on my research. There have been so many situations when I have to sacrifice my time with her for the experiment, but Emma never complains and she always amens to my decision. My wife is the best gift from God in my life.

Table of Contents

List of Figures

List of Abbreviations

CMT	coupled-mode theory
CWBG	complex waveguide Bragg grating
DFT	Discrete Fourier Transform
EBL	E-beam Lithography
FBG	fiber Bragg grating
FDM	Finite Difference Method
FWHM	Full Width at Half Maximum
IS	Inverse Scattering
LA	Layer Adding algorithm
LHS	Laser Height Sensing
LP	Layer Peeling algorithm
LPCVD	Low Pressure Chemical Vapor Deposition
MFD	Mode Field Diameter
PECVD	Plasma-Enhanced Chemical Vapor Deposition
SOI	Silica-on-Insulator
TMM	transfer matrix method
WBG	waveguide Bragg grating
WDM	Wavelength-Division Multiplexing

Part I

Layer Peeling/Adding Algorithm and Complex Waveguide Bragg Grating For Any Spectrum Generation

Chapter 1: Introduction

1.1 Single-Notch Filter vs Multi-Notch Filter

The first part of this thesis is mainly about designing and fabricating optical filters, so it is best to start from one of the simplest optical filters, which is a Fiber Bragg Grating (FBG) [1] [2] [3] [4]. As shown in Fig. 1.1, a FBG is basically a special optical fiber with periodic index variation in its fiber core region. This is generally done with photo-sensitive fibers, excimer lasers and phase-masks. When light passes through a FBG with periodic index variation, one particular wavelength band will be blocked and reflected, while all the other wavelengths will not be affected and will be transmitted. The central reflected wavelength λ_B, which is called Bragg wavelength, can be calculated using the following phase-matching equation:

$$\lambda_B = 2n_e\Lambda \tag{1.1}$$

Here, n_e is the effective index of the FBG, and Λ is the period for the index variation. Wavelength satisfying the above equation will satisfy constructive interference for reflection. Thus this wavelength will be reflected by the Bragg grating. The degree of reflection and the 3-dB bandwidth of the reflection band, will depend

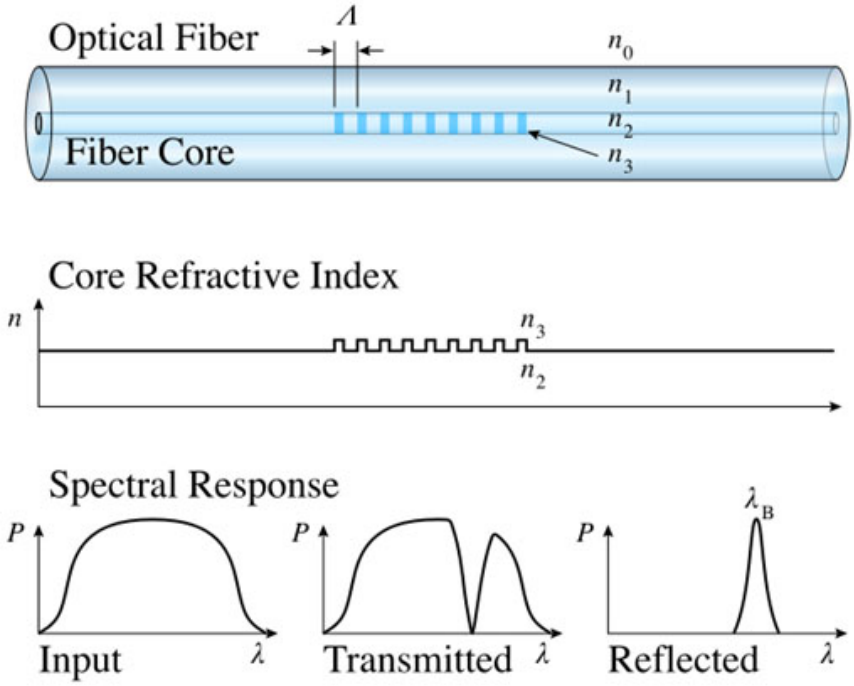

Figure 1.1: A simple fiber Bragg grating (FBG) reflects one particular wavelength, and lets all the other wavelengths pass through. The limitation is that there is only one notch in its transmission spectrum. This figure was from Wikipedia: https://en.wikipedia.org/wiki/Fiber_Bragg_grating

on the number of periods and the amount of effective index variation.

Waveguide Bragg Grating (WBG) is the counterpart of FBG on a planar platform [5] [6] [7]. Compared with FBGs which have the benefits of ultra-low propagation loss and perfect polarization independence, the major advantage of WBGs is their compactness and thus the capabilities of integration with other devices. In our later experiments, all our complex waveguide and grating devices can be fabricated on a small chip of only finger-nail size. Also, because fibers and integrated waveguides both have its pros and cons (waveguides are lossy but compact, fibers have low loss but take more space), the interaction between them becomes an important and popular topic. This is also the subject of the second half of this thesis. We will discuss the coupling mechanism between fibers and waveguides in great details.

There is a common limitation for both FBG and WBG: they can remove just one single wavelength band in the transmission spectrum. For most practical applications, the removal of that particular spectral band may be already good enough. However, there are still some applications which require the removal of more than just one single wavelength. For instance, as shown in Fig. 1.2, quite a few wavelengths need to be removed simultaneously in the transmission spectrum [8]. In this case, the idea of simple FBG or WBG is not sufficient. Several main reasons are explained below.

First of all, when some of the target wavelengths to be removed are distributed very closely in the spectral domain, it will be hard to realize these close spectral notches on a physical device. Assuming the task is that we want to remove both the wavelengths of $1550nm$ and $1551nm$ with a $3-dB$ width of only $0.2nm-0.3nm$.

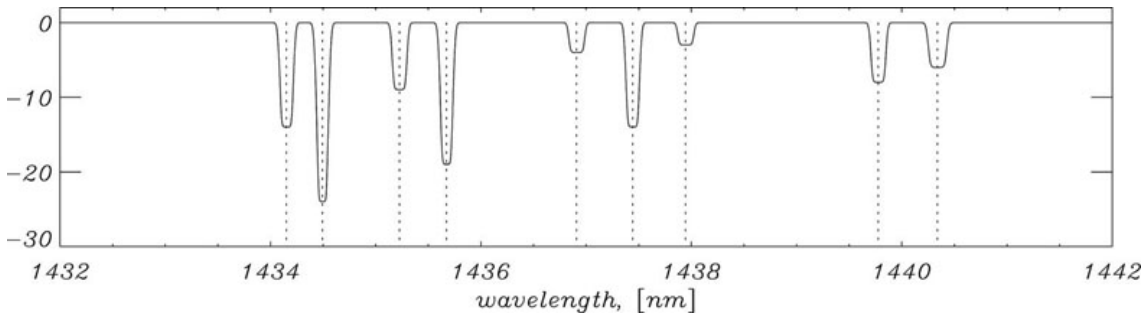

Figure 1.2: An application which requires the removal of multiple randomly-distributed wavelengths.

That means if we are going to use one grating to filter out $1550nm$, and another grating for $1551nm$, assuming an average effective index of 1.500, the periods of these two gratings are

$$\Lambda_1 = \frac{\lambda_{B1}}{2n_e} = 516.67nm \tag{1.2}$$

$$\Lambda_2 = \frac{\lambda_{B2}}{2n_e} = 517.00nm \tag{1.3}$$

Leaving alone the fact that whether a period of $516.67nm$ can be written accurately or not, just look at the length difference between two periods of the 1_{st} grating and the 2_{nd} grating, which is only $0.33nm$ in this example. That is to say, the period of the 2_{nd} grating needs to be only $0.33nm$ larger than the period of the 1_{st} grating. In real fabrication, it is impossible to fabricate two separate gratings whose periods are just $0.33nm$ different.

The second reason why connecting many simple FBGs or WBGs in series is not a good idea for multi-notch filtering applications lies in the total size and the overall loss. Connecting all these gratings together will give a long device overall (especially

for FBG), and it will result in very low throughput correspondingly (especially for WBG).

Moreover, there are also potential problems of narrow-band filtering and side-lobes. If the bandwidths of the spectral notches need to be very narrow, say only $0.3nm$ for the 3-dB width, then a long grating is required with a large number of periods and very small effective index variations. Finally, if we want to generate a very smooth transmission/reflection spectrum without any obvious spectral side-lobes, then the techniques of apodization should be added to the design of gratings, which adds up the complexity of the design and fabrication.

1.2 The Fundamental Problem of Optical Filter Design

Now let's go one step back from the notch filters, and let us think a little more generally. Here, we want to think of some fundamental and general theory suitable for all the various applications, not just notch filters. Although we discussed single-notch and multi-notch filters, the filtering function itself doesn't have to be limited to one single spectral type. Thus one of the fundamental problems for designing optical filters is whether it is possible to realize any arbitrary filtering function. A traditional optical filter, either a FBG or a WBG, removes only one particular spectral band in its transmission spectrum. But what if the target spectrum has an irregular shape such as shown in Fig. 1.3? Or what if we want to realize a filter that needs to remove hundreds of spectral bands simultaneously? Are there complex filters available for such general purposes? And if so, then how should the black box be constructed both theoretically and experimentally?

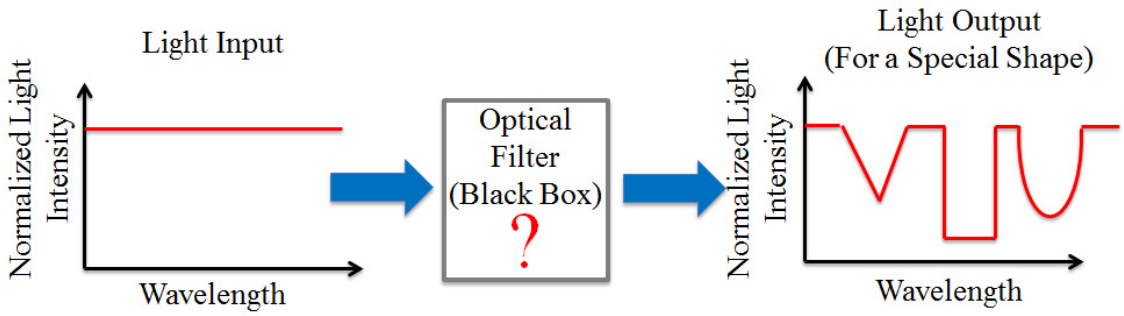

Figure 1.3: Assuming we want to design and build an optical filter that gives a very special filtering function, which has a triangle, a rectangle and an arc in its transmission spectrum, how should we design the optical filters? What should be in the black box physically?

1.3 An Important Application in Astrophysics

Fig. 1.4(a) gives an example where such arbitrary on-chip optical filters could be of great use [9, 10]. When Earth-based telescopes collect light from celestial objects, the collected light contains not only useful spectral information from these objects, but also foreground light emitted by the Earth's own atmosphere. In the near-infrared region, particularly between wavelengths of $1\mu m$ and $1.8\mu m$, the night sky spectrum is dominated by bright spectral lines due to hydroxyl (OH) emission from the atmosphere. As shown in Fig. 1.4(b), there are hundreds of randomly-distributed OH emission lines over this wavelength range, and each of these lines is very narrow. The signal from these lines completely dominates over that of most astronomical targets, particularly faint distant sources whose emission is red-shifted into the near-infrared window due to cosmological expansion. As a result, astrophysicists have long sought to reduce or eliminate altogether the effects of the Earth's atmosphere by having facilities operating at very high altitudes (e.g., *Stratospheric Observatory for Infrared Astronomy*) or in space (e.g., *Hubble Space Telescope*). These facilities are, however, much more expensive than ground-based telescopes of the same sizes.

A potentially cheaper solution is to use ground-based telescopes but eliminate the OH emission lines using complex optical filters. At first thought, thin-film optical filters, fabricated using the optical thin-film coating technology [11], may be a good starting point. However, as will be shown later, to realize a complex filter that removes multiple narrow spectral lines, the filter itself has to be constituted

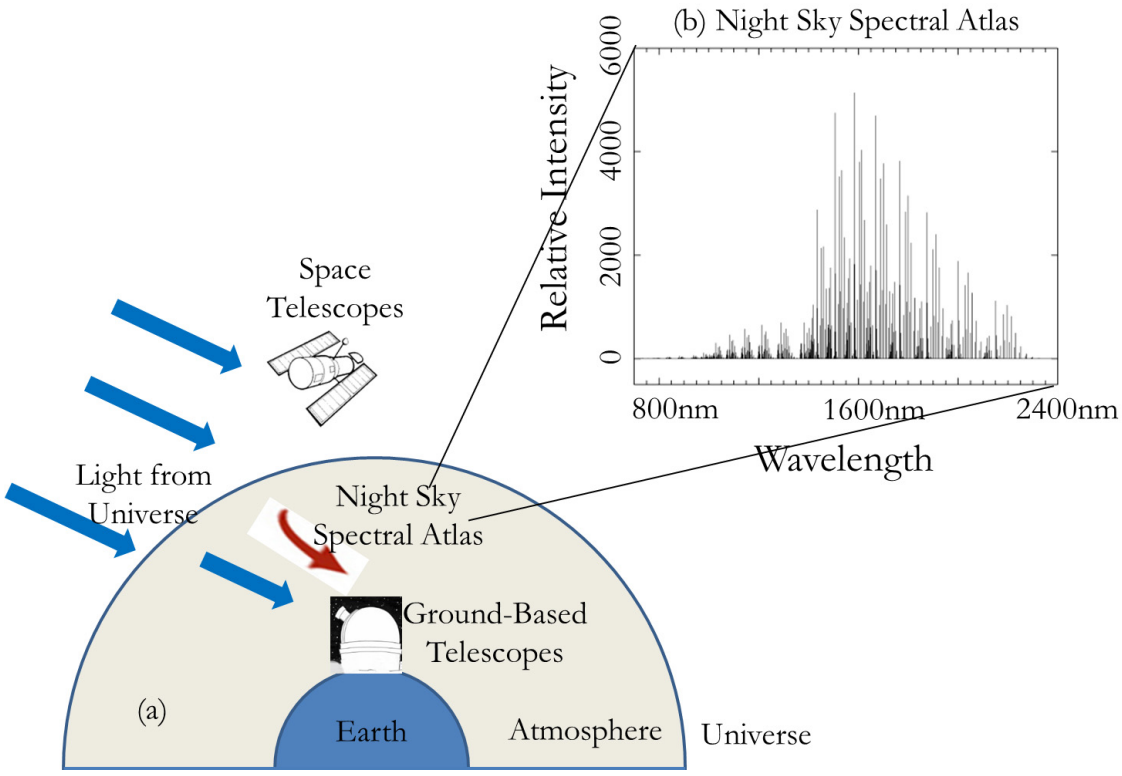

Figure 1.4: (a) The bright OH emission lines in the night sky are the main obstacles preventing ground-based telescopes from reaching the sensitivity levels of space-borne telescopes at near-infrared wavelengths. (b) Night sky spectrum from Ref. 7, dominated by hundreds of randomly-distributed OH emission lines, whose absolute and relative intensities are highly time-variable. In the astrophysics experiment, these narrow and highly time-variable OH-lines (of order 400 lines) of spectral width of 0.3-0.4 nm have to be removed simultaneously with a large suppression ratio of at least 15 dB. Reproduced with permission from P. Rousselot, C. Lidman, J.-G. Cuby, G. Moreels, and G. Monnet, Astron. Astrophys. 354, 1134 (2000), ©ESO.

of as many as 200,000 segments/layers, whose index variations have no regularity. This makes it unpractical for thin-film filters.

In a previous paper, our colleague Prof. Joss Bland-Hawthorn showed that the OH emission lines can be filtered out using an aperiodic Bragg grating implemented on a fiber platform [12]. An aperiodic fiber Bragg grating (FBG) with a total length of $5cm$ is capable of removing ~ 100 narrow OH emission lines simultaneously. Such aperiodic FBG devices have been tested on ground-based telescopes and delivered promising results [8] [13] [14] [15].

Later on in this thesis, we will propose an alternative approach based on Bragg gratings on planar waveguide platforms for applications requiring integration and compactness. In the astrophysics experiment, a large number (of order 400) of narrow OH lines with spectral width of 0.3-0.4 nm and spectral precision better than $\pm$ 0.1 nm have to be removed simultaneously with a large suppression ratio of at least 15 dB, as they all contribute to a broad and highly time-variable background light level in the spectrometer. Such a background has to be removed in order to study faint objects in the night sky. This paper presents the theoretical and experimental approaches for realizing such a complex waveguide Bragg grating (CWBG). As we discuss below, this type of CWBG may find applications not only in the field of astrophysics, but also potentially in the areas of ultra-fast pulse generation [16] [17] and slow-light [18].

1.4 Searching for An Integrated Optical Filter for Any Spectrum

Therefore, the question lying in front of us is: how should we design a single grating which can realize basically any spectral shape? Fortunately, if we just focus on the theory and disregard the difficulty of implementation, there are indeed some very good theoretical models and methods to solve this problem [19] [20]. In general, all these methods are called inverse scattering (IS) algorithms, as they are just the reverse process of finding the spectrum from the effective index profile, which is categorized as forward scattering problems. According to the IS algorithm, one single complex-shaped grating is already enough to remove multiple spectral lines with various depths and bandwidths. The input here is the desired spectral shape, and the output of the theory shows the grating profile or the effective index distribution along the grating. To get some better knowledge of all these theories, a nice comparison between various methods of grating synthesis is made by our collaborators at University of Sydney, and it can be found in [21]. Now the next question is, how can we go from the algorithm to making a real complex grating or complex optical filter?

Such optical filters have already been realized successfully on the fiber platform by our collaborators at University of Sydney, to get rid of many spectral lines [12]. However, the size of this aperiodic fiber Bragg gratings (AFBG) is not very compact and the approach does not lead to ease of integration with other integrated photonic devices. Compared with FBG, WBG is implemented on the waveguide platform, and has much smaller footprint and is suitable for dense-integration applications in

the future. The fabrication process of WBG is also CMOS-compatible, which makes it really promising. In some recent papers published by the Ghent University, WBG were also written by deep-UV lithography experimentally for random spectral tailoring [22] [23], however their algorithm only assumes low index variation and neglects second-order and higher-order reflections. Moreover, the fabricated WBG is based on a 2-layer waveguide structure, which requires two lithography and two etching steps, giving some difficulty of precise pattern overlap between multiple lithography steps. More lithography steps also indicate bigger cost in the fabrication or manufacturing, thus limiting the future potential of mass production and commercialization.

Here, we proposed a physical 3D WBG structure as shown in Fig. 1.5. The fabrication process is CMOS-compatible and is easy to implement. Our grating only has one single layer and the only varying parameter here is the waveguide width. The Si_3N_4/SiO_2 waveguide material system has compact size, low propagation loss, high coupling efficiency and an ultra-broadband transparency window. It is an elegant structure with just scales like a small chip.

The rest of this part of the thesis will be organized as follows: in Chapter 2, a Layer Peeling/Adding algorithm, which is the core theoretical portion of this thesis, will be developed and presented in great details. In Chapter 3, the effective index variations are mapped to a real 3D integrated waveguide grating structure. Then in Chapter 4, the nano-fabrication process, the measurement setup and the experimental results will be demonstrated. Finally in Chapter 5 and Chapter 6, we will conclude and discuss future work.

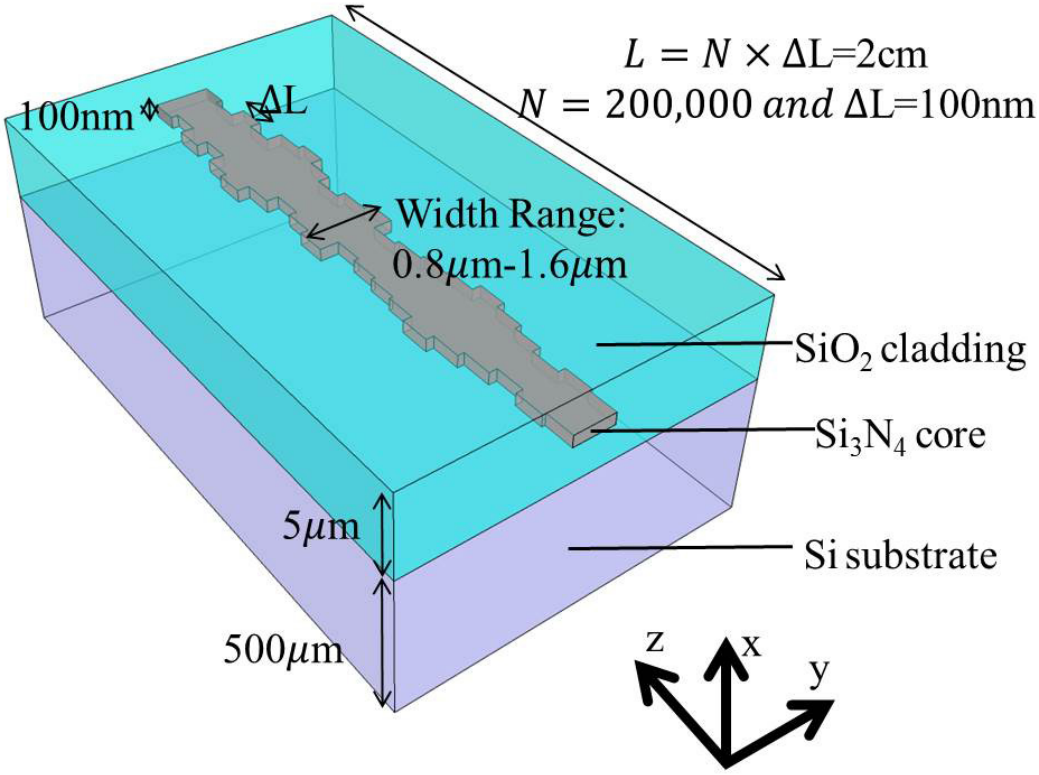

Figure 1.5: 1-layer Structure of CWBG on Si_3N_4/SiO_2 waveguide platform. The width of the CWBG varies in an aperiodic way. This is the experimental waveguide grating structure used in this thesis.

Chapter 2: Layer Peeling & Adding Algorithm

This chapter mainly discusses the theoretical algorithm for designing the optical filter. In order to explain the algorithm clearly, some introduction and derivations of the coupled mode theory and the transfer matrix method will be given at first. Then the the Layer Peeling/Adding Algorithm will be discussed in great details. Finally, in the end of this chapter, several real filter design examples will be demonstrated to show not only the effectiveness of our algorithm and but also the effective index variations for realizing specific spectra.

2.1 Coupled Mode Theory

Coupled mode theory (CMT) is one of the most successful theory for investigating any type of grating structures. The grating is essentially an optical fiber or waveguide structure with an effective index perturbation. In a medium which has a constant refractive index everywhere, different optical modes are orthogonal to each other in principle. But as long as an effective index perturbation occurs, different modes will start talking to each other. For instance, some optical power of the forward-propagating mode may be transferred to that of the backward-propagating mode, the degree of which depends on the amount of the effective index variation.

CMT is presented and described elegantly in a number of papers and books, and some of those references can be found in [24] [25] [26] [27] [28]. It is noted that the scientific notations are slightly different between these references. For simplicity, the notation in this thesis follows [24] closely. In this notation, light propagates along only $+z$ (forward) and $-z$ (backward) direction. The x and y are both traverse directions. Also, the implicit time dependence is $exp(-i\omega t)$, so the forward propagating wave with the propagation constant β will have the form with the term $exp[i(\beta z - \omega t)]$.

To start with, several reasonable assumptions are made here. First of all, in the algorithm we assume the waveguide is lossless. In other words, the refractive index is a real number. Secondly, we assume that single-mode condition is observed in the entire spectral range, which means no higher order radiating mode occurs. This indicates that only forward-propagating mode and backward-propagating mode should be considered in the theory. It is also the real situation in FBGs and WBGs. Thirdly, the index variation is assumed to be much smaller than the average effective index n_0. Let us first recall our memory of the four Maxwell's Equations:

$$\begin{aligned} \vec{\nabla} \cdot \vec{D} &= \rho \\ \vec{\nabla} \cdot \vec{B} &= 0 \\ \vec{\nabla} \times \vec{E} &= -\frac{\partial \vec{B}}{\partial t} \\ \vec{\nabla} \times \vec{H} &= \vec{J} + \frac{\partial \vec{D}}{\partial t} \end{aligned} \tag{2.1}$$

where $\vec{E}$ and $\vec{H}$ are electric and magnetic field vectors, and $\vec{D}$ and $\vec{B}$ are electric and magnetic flux densities, respectively. $\vec{J}$ is the current density and ρ is the free charge density.

Then we can go with the derivations. The scalar wave equation (deduced directly from the above Maxwell's equations assuming $\rho = 0$ and $J = 0$) tells us that

$$\{\nabla^2 + k^2 n^2(x, y, z)\}E(x, y, z) = 0 \tag{2.2}$$

This can be further written as

$$\{\nabla_t^2 + k^2 n^2(x, y, z) + \partial^2/\partial z^2\}E(x, y, z) = 0 \tag{2.3}$$

Here $\nabla_t^2 = \partial^2/\partial x^2 + \partial^2/\partial y^2$, and $k = \omega/c$ is the vacuum wavenumber. Here, n is the overall effective index which includes both the average effective index and the effective index variation. As a comparison, we will now define another parameter n_0 to represent the average effective index, which is a constant for the grating.

Since we are considering the coupling between the forward-propagating mode and the backward-propagating mode, the electric field can be written as

$$E(x, y, z) = b_1(z)\Psi(x, y) + b_{-1}(z)\Psi(x, y) \tag{2.4}$$

The whole electric field $E(x, y, z)$ should satisfy (2.3), and $\Psi(x, y)$ should satisfy the wave equation with average index n_0 below

$$\{\nabla_t^2 + k^2 n_0^2 - \beta^2\}\Psi(x,y) = 0 \tag{2.5}$$

To reach (2.5), just remember that the electric field in a medium with constant index has a propagation term which is either $exp(+i\beta z)$ or $exp(-i\beta z)$.

From (2.3) (2.4) (2.5) we can obtain

$$\frac{d^2}{dz^2}(b_1 + b_{-1})\Psi + [\beta^2 + k^2(n^2 - n_0^2)](b_1 + b_{-1})\Psi = 0 \tag{2.6}$$

Multiplying (2.6) by Ψ and integrating over the whole xy-plane, we can get

$$\frac{d^2}{dz^2}(b_1 + b_{-1}) + [\beta^2 + 2kn_0 D_{11}(z)](b_1 + b_{-1}) = 0 \tag{2.7}$$

where

$$D_{11}(z) \approx k(n - n_0) \tag{2.8}$$

because $n^2 - n_0^2 \approx 2n_0(n - n_0)$, with the third assumption we made before.

Now, (2.7) can be decomposed into a set of first order differential equations

$$\frac{db_1}{dz} = i(\beta + D_{11})b_1 + iD_{11}b_{-1} \tag{2.9}$$

$$\frac{db_{-1}}{dz} = -i(\beta + D_{11})b_{-1} - iD_{11}b_1 \tag{2.10}$$

If there is no index variation, $n = n_0$, $D_{11} = 0$, then $b_1(z) \propto exp(i\beta z)$ and $b_{-1}(z) \propto exp(-i\beta z)$. Then $b_1(z)$ will have no interaction with $b_{-1}(z)$ at all. On

the other hand, if there is an index variation, then $D_{11} \neq 0$, so the forward and backward modes will start to interact with each other.

For our grating, we can represent the index variation as

$$n - n_0 = \Delta n(z) cos(\frac{2\pi}{\Lambda} z + \theta(z)) \tag{2.11}$$

and we can rewrite $D_{11}(z)$ as

$$D_{11}(z) = \kappa(z) exp(i\frac{2\pi}{\Lambda} z) + \kappa^*(z) exp(-i\frac{2\pi}{\Lambda} z) \tag{2.12}$$

where $\kappa(z)$ is a complex and slowly varying function of z. To further simplify (2.9) and (2.10), we will define the new field amplitude u and v as

$$b_1(z) = u(z) exp(i\frac{\pi}{\Lambda} z) \tag{2.13}$$

$$b_{-1}(z) = v(z) exp(-i\frac{\pi}{\Lambda} z) \tag{2.14}$$

Using (2.9) (2.10) (2.12) (2.13) (2.14) we finally obtain the coupled mode equations

$$\frac{du}{dz} = i\delta u + q(z) v \tag{2.15}$$

$$\frac{dv}{dz} = -i\delta v + q^*(z) u \tag{2.16}$$

where $\delta = \beta - \pi/\Lambda$ is the wavenumber detuning with respect to the central wavelength $\lambda_0 = 2n_0\Lambda$, and $q(z)$ is the complex coupling coefficient $q(z) = i\kappa(z)$

In the latter text, we will show that from the Layer Peeling/Adding algorithm, we can calculate all the values of $q(z)$, but for a physical optical filter, knowing $q(z)$ is far from being satisfactory. To design a real optical filter, it is most important to know the effective index $n(z)$ along that filter. The relation between $q(z)$ and $n(z)$ is given below:

$$\mid q(z) \mid = \frac{\pi \Delta n(z)}{\lambda} \tag{2.17}$$

$$arg(q(z)) = \theta(z) + \pi/2 \tag{2.18}$$

Now that we know the coupled-mode equations and the relation between $q(z)$ and $n(z)$. The coupled mode equations derived above are a set of elegant and classic equations. They form the basis for the theory that will be used later.

2.2 Transfer Matrix Method

Transfer matrix method (TMM) is the typical method used in the forward-scattering problems, as it calculates the transmission/reflection spectrum starting from the effective indices. It is a simple and straightfoward approach shown in many books [27] [28]. On the other hand, the Layer Peeling algorithm, which will be deduced later, allows us to calculate the effective index from the final spectrum.

Transfer matrix method uses a discretized model, where it discretizes the whole grating into a sufficient number N of small segments. Each segment is so short that it can be treated as having just a constant effective index variation intensity. In other words, the effective index of each Δ segment will vary sinusoidally according to (3.2) with $\Delta n(z)$ to be constant. $\Delta n(z)$ of different Δ segment may not be the same, and in our cases it can be very aperiodic. If the overall length of the grating is L, then the length of each segment will be

$$\Delta = L/N \tag{2.19}$$

Derived from the coupled mode equations before, the electric fields can be written as

$$\begin{bmatrix} u(z+\Delta) \\ v(z+\Delta) \end{bmatrix} = \begin{bmatrix} cosh(\gamma\Delta) + i\frac{\delta}{\gamma}sinh(\gamma\Delta) & \frac{q}{\gamma}sinh(\gamma\Delta) \\ \frac{q^*}{\gamma}sinh(\gamma\Delta) & cosh(\gamma\Delta) - i\frac{\delta}{\gamma}sinh(\gamma\Delta) \end{bmatrix} \begin{bmatrix} u(z) \\ v(z) \end{bmatrix} \tag{2.20}$$

Here, light propagates along the z direction, $u(z)$ and $v(z)$ are the forward-

propagating and backward-propagating field amplitude at location z, $u(z+\Delta)$ and $v(z+\Delta)$ are the forward-propagating and backward-propagating field amplitude at location $z+\Delta$. q is the complex coupling coefficient in accordance with the previous section, $\delta = \beta - \pi/\Lambda$ is the wavenumber detuning, and γ is defined as $\gamma^2 = \mid q \mid^2 - \delta^2$. (2.20) calculates $u(z+\Delta)$ and $v(z+\Delta)$ from the information of $u(z)$ and $v(z)$, given the effective index variation in this Δ segment. Note here that the effective index variation is not shown in (2.20) explicitly, and instead it is contained in q.

From the above equation for a single segment, the overall transfer matrix of the grating is

$$T = T_N T_{N-1} T_{N-2} \cdots T_2 T_1 \tag{2.21}$$

Therefore

$$\begin{bmatrix} u(L) \\ v(L) \end{bmatrix} = T \begin{bmatrix} u(0) \\ v(0) \end{bmatrix} = \begin{bmatrix} T_{11} & T_{12} \\ T_{21} & T_{22} \end{bmatrix} \begin{bmatrix} u(0) \\ v(0) \end{bmatrix} \tag{2.22}$$

Notice that in (2.22), $v(L) = 0$ since the light will only go forward at $z = L$. The transfer matrix T is also wavelength dependent, and the wavelength information is already contained in the γ and δ parameter. Finally, the reflection coefficient can be obtained from T as

$$r(\delta) = -T_{21}/T_{22} \tag{2.23}$$

As a brief conclusion of the transfer matrix method, I want to emphasize its main purpose one more time: it calculates the transmission/reflection spectrum from the effective indices of the gratings/filters for all the wavelengths. It also means the direction of calculation is from the space domain to the frequency domain. It is

considered as a forward-scattering method.

2.3 Layer Peeling/Adding Algorithm

Layer Peeling/Adding algorithm actually contains two sub-algorithms which use very similar approaches but totally opposite directions. The Layer Peeling (LP) algorithm receives the target spectrum as the input and output the distribution of the effective indices. The Layer Adding (LA) algorithm receives the effective index distribution as the input, and gives the spectrum as the output. In this sense, Layer Adding and Transfer Matrix Method have the same purpose, although Layer Adding is much faster than the Transfer Matrix Method. The details of LP and LA are discussed below. This thesis follows the notation from [19]. Some other good references of LP and LA can also be found in [24] [29] [30].

First of all, starting from (2.20), the transfer matrix T_j of the j_{th} segment is decomposed as the multiplication of two sub-matrices.

$$T_j = T^{\Delta} T_j^{\rho} \tag{2.24}$$

where

$$T^{\Delta} = \begin{bmatrix} exp(i\delta\Delta) & 0 \\ 0 & exp(-i\delta\Delta) \end{bmatrix} \tag{2.25}$$

$$T_j^{\rho} = (1- \mid \rho_j \mid^2)^{-1/2} \begin{bmatrix} 1 & -\rho_j^* \\ -\rho_j & 1 \end{bmatrix} \tag{2.26}$$

This is done by simplifying the transfer matrix of each segment into a propagation matrix T^{Δ} and a reflection matrix T_j^{ρ}. In the propagation matrix T_j^{ρ}, we only consider the propagation of light, so only the optical phase changes by $exp(i\delta\Delta)$. In the reflection matrix T_j^{ρ}, light from the j_{th} segment sees the effective index of the $(j+1)_{th}$ segment, so some of the forward-propagating power might be reflected. T^{Δ} is obtained from T by letting $q \to 0$, and T_j^{ρ} is obtained from T by letting $q \to \infty$ while holding $q\Delta$ to be a constant. ρ is the complex reflection coefficient, and it is related to q in the following equations:

$$\rho_j = -tanh(\mid q_j \mid \Delta)\frac{q_j^*}{\mid q_j \mid} \tag{2.27}$$

$$q_j = -\frac{1}{\Delta}tanh^{-1}(\mid \rho_j \mid)\frac{\rho_j^*}{\mid \rho_j \mid} \tag{2.28}$$

From (2.24) (2.25) (2.26) we can write $u(z+\Delta)$ and $v(z+\Delta)$ as

$$\begin{bmatrix} u(z+\Delta,\delta) \\ v(z+\Delta,\delta) \end{bmatrix} = \begin{bmatrix} exp(i\delta\Delta) & 0 \\ 0 & exp(-i\delta\Delta) \end{bmatrix} (1- \mid \rho_j \mid^2)^{-1/2} \begin{bmatrix} 1 & -\rho_j^* \\ -\rho_j & 1 \end{bmatrix} \begin{bmatrix} u(z,\delta) \\ v(z,\delta) \end{bmatrix} \tag{2.29}$$

Please also note that the reflectivity is a function of z and δ and it can be written as

$$r(z,\delta) = \frac{v(z,\delta)}{u(z,\delta)} \tag{2.30}$$

$$r(z+\Delta,\delta) = \frac{v(z+\Delta,\delta)}{u(z+\Delta,\delta)} \tag{2.31}$$

Therefore, from (2.29) (2.30) (2.31) we obtain the following two key equations

$$r(z+\Delta,\delta) = exp(-i2\delta\Delta)\frac{r(z,\delta)-\rho(z)}{1-\rho^*(z)r(z,\delta)} \tag{2.32}$$

$$r(z,\delta) = \frac{r(z+\Delta,\delta)+\rho(z)exp(-i2\delta\Delta)}{exp(-i2\delta\Delta)+\rho^*(z)r(z+\Delta,\delta)} \tag{2.33}$$

These two equations above are the key equations in this thesis. (2.32) is the Layer Peeling equation, and (2.33) is the Layer Adding equation. (2.32) allows us to obtain the reflectivity and the effective index of the $(j+1)_{th}$ segment, if we already have the reflectivity and the effective index of the j_{th} segment. (2.33) does the reverse. It calculates the reconstructed spectrum (for comparision with the original target spectrum) from the calculated effective indices.

A key point to note here is the physical meaning of Δ, δ and $r(z,\delta)$. As discussed before, Δ is the physical length of each segment used in LP/LA algorithm. δ is the wavelength detuning from the central resonance wavelength. So although the wavelength λ does not appear in (2.32) and (2.33), it has been implicitly represented by the term δ. $r(z,\delta)$ is the reflectivity r versus wavelength δ (now we know δ is just another expression of λ) at position z. So $r(0,\delta)$ is the original reflectivity spectrum seen from the beginning of the whole grating, $r(\Delta,\delta)$ is the reflectivity spectrum seen from the beginning of the 1_{st} grating segment, and $r(2\Delta,\delta)$ is the reflectivity spectrum seen from the beginning of the 2_{nd} grating segment, etc.

A simple analogy is shown below so the readers can understand the LP/LA algorithm better. Suppose we have an onion in front of us with a special shape (it may not be perfectly spherical, just like the fact that real applications may not

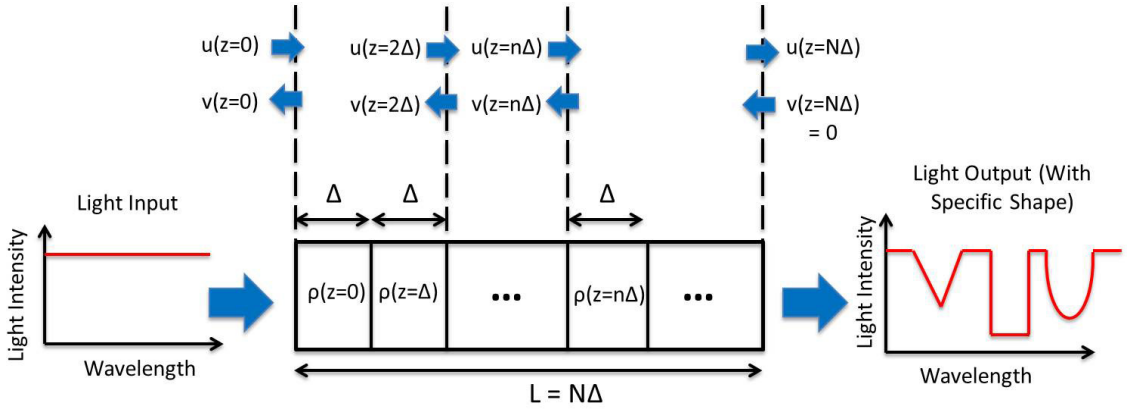

Figure 2.1: In LP/LA algorithm, the overall grating is discretized into many small segments, each with a length of Δ. The total length of the grating is $L = N\Delta$. Effective indices for all these segments can be calculated precisely using (2.32) one by one. The reconstructed spectrum can then be checked using (2.33).

have good-looking simple spectra). The onion is composed of many many layers, and each layer of the onion carries some specific information (thickness, any spot or irregularity for that layer, etc) about that layer, so if we peel this onion layer by layer we could know how the onion is constructed in detail. There is only one rule: to see the j_{th} layer we first have to peel off the $(j-1)_{th}$ layer. So first of all, the outermost layer (the 1_{st} segment) is peeled off, and its information (q, ρ and n_{eff}) is written down (for later reconstruction), revealing the 2_{nd} layer. Then the 2_{nd} layer is peeled off and recorded, and then the 3_{rd} layer, the 4_{th} layer, so on and so forth. The peeling occurs in an iterative and sequential order. Finally, all the layers of the onion are peeled off, and the complete information of the onion is recorded. From these recorded information of layers we are able to reconstruct the same onion perfectly later on. This is exactly how the Layer Peeling works.

In this analogy, the original shape of the onion (without any peeling) is the target reflection spectrum which usually has a special shape, and the information of

different layers is the effective indices of different discretized segments in the grating.

As shown in Fig. 2.1, LP/LA algorithm works exactly in the same way. From the initial target reflectivity spectrum $r(z = 0, \delta)$, $\rho(z = 0)$ is obtained, which corresponds to the coupling coefficient of the 1st segment of the grating. Then using Eqn. 2.32, $r(z = \Delta, \delta)$ can be calculated, which is essentially the reflectivity spectrum seen from the beginning of the 2nd segment of the grating. Then $\rho(z = \Delta)$ is obtained from the value of $r(z = \Delta, \delta)$. As a next step, $r(z = 2\Delta, \delta)$ and $\rho(z = 2\Delta)$ are calculated. This procedure can be iterated until information of all those grating segments are found.

LA is just the reverse of LP, and it is used to evaluate the performance of a grating, assuming the effective index profile is obtained already. It is like obtaining the overall shape of a complete onion by assembling all the layers together. At first, we start from the innermost layer (which corresponds to the last segment of the grating). Then the 2nd layer is added on top of the innermost layer. Then the 3rd innermost layer is added. This iterative process comes in a reverse sequence compared to LP. Finally, when all the layers are assembled together, the outer surface of the onion will be presented to us in a specific shape (which corresponds to the reconstructed reflection spectrum). Hopefully, this is the desired shape that we need to design.

We have covered a lot of details in this section of the thesis, but these are the core part of the whole algorithm. The importance of LP/LA is that by using the LP/LA algorithm, any types of onions (optical filters) can be designed, analyzed and reconstructed.

Before we finish with this segment, let me state one more property of the LP/LA algorithm. It is worth noting that (2.32) only gives the distribution of effective index of the grating, but it does not indicate the exact material system and platform upon which the grating will be implemented. Therefore, the LP/LA algorithm introduced here can be applied to all the optical filter structures and platforms. In practise, this algorithm can be applied for both FBG and WBG platforms.

2.4 Discrete Fourier Transform & Target Spectrum Preparation

In the previous section, we derived equations for Layer Peeling and Layer Adding algorithms. And it should be clear now that $q(z)$, $\rho(z)$ and $n_{eff}(z) - n_0(z)$ actually all indicate the same thing: the effective index variation. The current question is: what is the relation between the effective index $n_{eff}(z)$ of a certain segment and the term $r(z, \delta)$, the reflectivity spectrum seen from the beginning of that segment?

In order to answer this question, let's write the equation of the inverse Discrete Fourier Transform (DFT) in the following way:

$$h(j) = \frac{1}{M} \sum_{m} r(m) exp(-\frac{i2\pi jm}{M}), j = 0, 1, 2, ... \tag{2.34}$$

(2.34) is the inverse DFT equation which gives the impulse response $h(j)$, starting from the discretized reflectivity spectrum. M is the number of spectral points in the algorithm. Let us recall that $r(z, \delta)$ is the reflectivity spectrum seen from the beginning of the location z versus wavelength δ. And it is important to notice that the effective index of the segment in the location z corresponds only to the first element of the impulse response $h(0)$. The reason is that if we send an impulse to the grating, $h(0)$ will be affected by the 1_{st} segment of the grating only, since light at that time does not have enough time to travel to the other (2_{nd})

segments. This rule applies for all the layers, so $\rho(z) = h(0)$. Therefore

$$\rho(z) = \frac{1}{M} \sum r(z, \delta) \tag{2.35}$$

Also, in order for the DFT to work correctly, there is a relation between Δ in the time domain and the overall spectral detuning range δ_ω in the frequency domain, which is shown below in (2.36). A whole step-by-step process of the algorithm and all these parameters will be discussed in the next section.

$$\Delta = \frac{\pi}{\delta_\omega} \tag{2.36}$$

There is one last problem before we can run the algorithm correctly: the target spectrum needs some special treatment [19] [20]. If we take the inverse DFT to the original target spectrum (the default reflectivity spectrum is only a list of real numbers, without any imaginary part), the impulse response will probably have components for $t < 0$. Such an impulse response does not exist in real filters and gratings. For real gratings, the impulse function $h(t)$ always starts from $t = 0$. Otherwise if $h(t < 0) \neq 0$, it simply indicates that even before the impulse sees the grating, it already has some type of response from that grating!! That is not possible physically. In a physical world, we can never know what's inside a mysterious treasure box unless we first check its contents. No matter what detection methods we use (hands, eyes, or even X-rays), we have to first check it somehow. For a physical optical filter, the impulse response at time $t < 0$ should always be zero.

Because of this consideration, the reflectivity spectrum used for the algorithm needs to be treated in the following way. We will use a apodizing window (such as a Hanning function) to force the impulse function to become zero beyond a certain limit. Then the whole impulse response is shifted so that the first non-zero element starts at $t = 0$. This new impulse response is then converted back to the new reflectivity spectrum using DFT. Finally, the new reflectivity spectrum can be used as a valid input to the Layer Peeling/Adding algorithm, so we can start our calculation and design.

2.5 Step-by-Step Guide of Layer Peeling/Adding Algorithm

Let's summarize all the steps of the Layer Peeling/Adding algorithm below:

1) We start from a target reflection/transmission spectrum which can have any spectral shape. The spectrum is converted to a reflectivity spectrum so it could be used for the LP/LA algorithm.

2) An inverse discrete Fourier transform is performed on the reflectivity spectrum to get the impulse function. A Hanning function is then multiplied to the impulse function to force it to become zero beyond a certain range. The truncated impulse function is then shifted so that it starts at $t = 0$. This becomes the realizable impulse function of the grating structure.

3) A forward discrete Fourier transform converts the realizable impulse function to the reflectivity spectrum $r(z = 0, \delta)$.

4) $\rho(z = 0)$ is calculated from (2.35).

5) $r(z = \Delta, \delta)$ is obtained from $r(z = 0, \delta)$ and $\rho(z = 0)$ using (2.32).

6) Steps 4 and 5 are repeated to iteratively calculate the $\rho(z)$ throughout the whole grating.

7) The effective index of the grating is derived from ρ_z using (2.17) (2.18) (2.28).

8) As long as the effective index and $\rho(z)$ are available, the reconstructed spectrum can be obtained with either the Transfer Matrix Method or the Layer Adding Method in (2.33).

The time complexity of this algorithm is $O(MN)$, where M is the number of

spectral sampling points in the spectrum, N is the number of discretized segments in the grating. Up to now, we can say that although the inverse-scattering problem seems quite difficult in the beginning, but with the LP/LA algorithm is just as simple as the forward-scattering program.

2.6 Design Examples of Layer Peeling/Adding Algorithm

Generally speaking, LP/LA algorithm can be applied to the synthesis of any random spectrum. As a comparison, traditional design methods can only regenerate spectrum of very limited shapes. To prove the capability of the LP/LA algorithm, two design examples are demonstrated below, showing the reliability and accuracy of the proposed LP/LA algorithm. For each design, we always start with a target transmission/reflection spectrum, then LP algorithm would tell us the effective index variation. Then the LA algorithm or the Transfer Matrix Method will show us the reconstructed spectrum. If the parameters of the grating are chosen appropriately, then the reconstructed spectrum should look very similar to the original target spectrum.

The calculated effective index usually looks "weird" and very aperiodic, and seen from naked eyes there seems to be no regularity at all. The beauty of our approach is that, with such seemingly "weird" effective index variations, different wavelengths will respond exactly as what we want them to respond.

2.6.1 Design Example 1: An Arbitrary Spectrum

In the first example, a single grating is designed whose filtering function has a special shape, with a rectangle, a triangle and an arc in its transmission spectrum. Fig. 2.2 (a) shows the original target spectrum, Fig. 2.2 (b) is the calculated effective index variation, and Fig. 2.2 (c) shows the spectrum calculated from the reconstructed grating. To obtain the grating profile, the LP algorithm is first applied

to the target spectrum, then the LA algorithm is employed to calculate the spectrum from the synthesized grating. The synthesized grating is able to regenerate the target spectrum in this case.

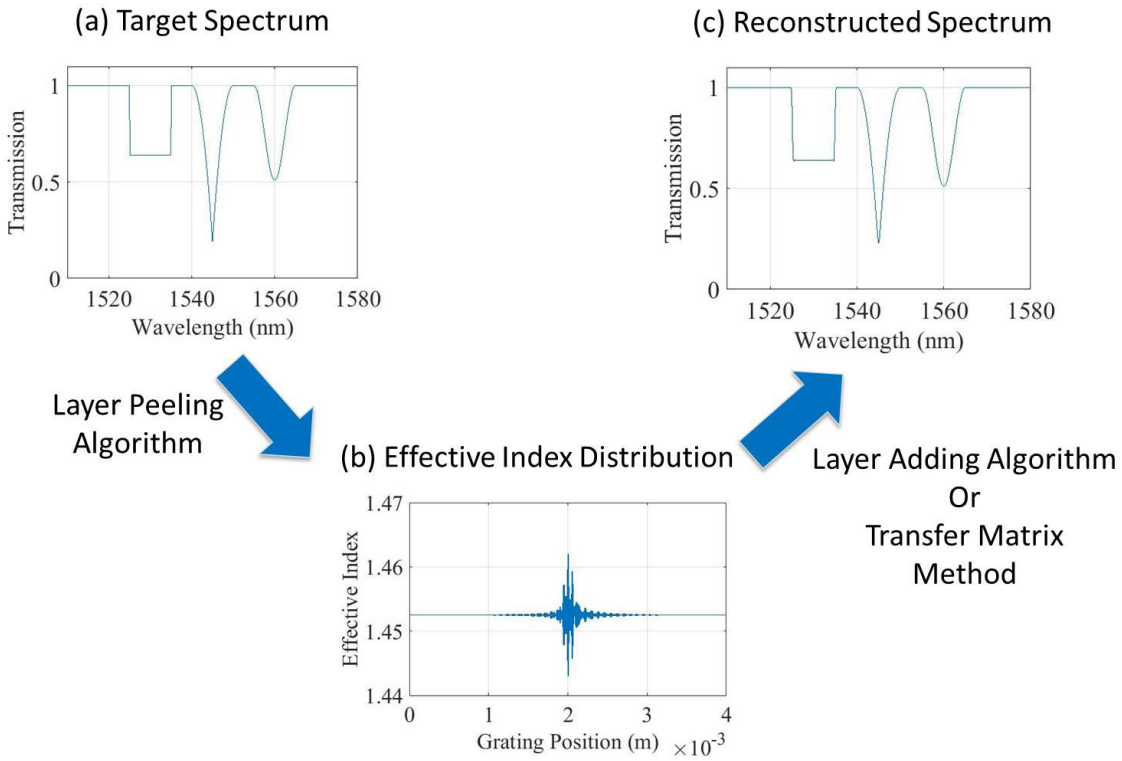

Figure 2.2: Synthesis of a grating with a special spectrum. (a) The target transmission spectrum has a profile with a rectangle, a triangle and an arc. (b) The effective index variation calculated using the Layer Peeling algorithm. (c) The reconstructed spectrum obtained from the calculated effective index. Note the similarity between (a) and (c).

2.6.2 Design Example 2: A Multi-Notch Filter with 150 Lines

The second design is even more persuasive. In this example, a very complex grating is to be synthesized, which has 150 randomly-distributed narrow notches in the transmission spectrum. To make it more random and arbitrary, each of the notches will have its own suppression ratio. Fig. 2.3 shows the original spectrum, the

calculated effective index, and the reconstructed spectrum. Again, the reconstructed grating regenerates the original target spectrum successfully. LP/LA algorithm still works perfectly in this case.

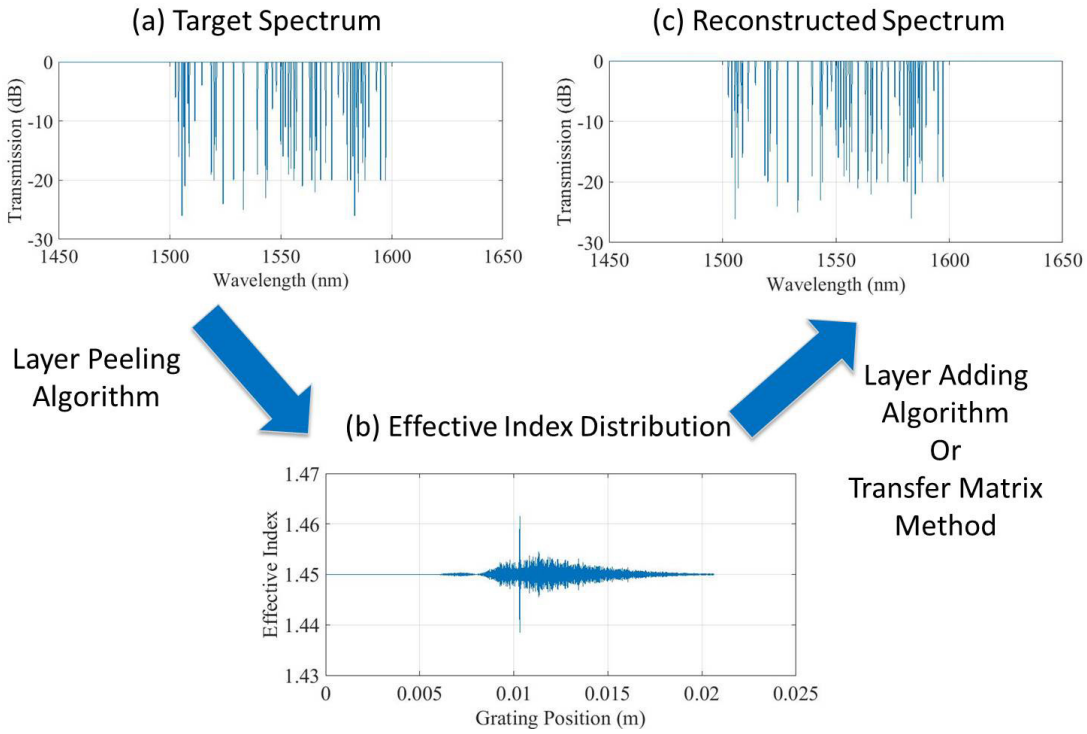

Figure 2.3: Synthesis of a grating whose transmission spectrum (in dB) has 150 randomly-distributed notches between 1500 nm and 1600 nm, while each notch has its own specific suppression ratio. (a) The target transmission spectrum with 150 notches. (b) The effective index variation calculated using the Layer Peeling algorithm. (c) The reconstructed spectrum obtained from the calculated effective index.

From these two examples, the power and potential of our LP/LA algorithm is fully demonstrated. In the theory which is assumed to be lossless, the target spectrum can be either a reflection spectrum or a transmission spectrum, since they just add up to unity. In reality however, if a WBG is fabricated, some of the incoming light may experience the scattering loss or the radiation loss, which can be caused by the stepped waveguide widths due to the discretization process. Therefore, in

the next chapter the detailed shape of the grating (e.g. the profile of the widths of the WBG) has to be determined. The information of the effective index variation obtained from the LP/LA is just a start for designing the real grating device, a 3-dimensional structure that can be fabricated and tested experimentally.

Chapter 3: Design & Simulation

3.1 From the LP/LA to Designing a Real CWBG

From the last chapter, it has been proved that by using the LP/LA algorithm, a grating profile can be calculated for any random spectrum. The output of the LP/LA algorithm gives the coupling coefficient q(z) (also sometimes called the grating profile) of the grating directly, but that does not indicate anything about the detailed structure of the grating. To realize a physical grating, we need to obtain the profile of the effective index of refraction along the z direction. In this chapter, a design procedure is described so a real CWBG can be synthesized.

The core part of designing a CWBG is to find an appropriate waveguide structure so that the grating profile q(z) can be realized by fabrication. The amplitude of q(z) reflects the change of the effective index at location z, which also denotes the strength of reflection at that point. q(z) and the change of the effective index are related by the following equation:

$$\mid q(z) \mid = \frac{\pi \Delta n(z)}{\lambda} \tag{3.1}$$

while the effective index of the waveguide at position z can be written as

$$n - n_0 = \Delta n(z) cos(\frac{2\pi}{\Lambda} z + \theta(z)) \tag{3.2}$$

Here, n_0 is the average effective index, and the real effective index is varying in a sinusoidal way, controlled by the amplitude Δn(z), the period Λ and the phase θ(z). For a practical CWBG, q(z) will vary aperiodically along the z direction of the grating. To analyze the real change of the effective index, let us assume that the maximum amplitude of q(z) is about 40 cm^{-1} [8]. As a consequence, Δn(z) will also vary according to q(z). At the wavelength of 1550 nm, the maximum value of Δn(z) is about

$$\Delta n(z)_{max} = \frac{\mid q(z)_{max} \mid \lambda}{\pi} \sim 0.002 \tag{3.3}$$

Therefore, the difference between the maximum effective index and the minimum effective index needs to be about 0.002×2 = 0.004, which is the range over which n(z) can vary. Considering the limitation of practical e-beam lithography, it is reasonable at first to assume that 20 discrete waveguide widths are written in order to realize a CWBG, whose effective indices cover this region of about 0.004. Therefore, at first thought we can roughly divide 0.004 by 20, which means that the real effective indices need to vary as n_{avg} - 0.002, n_{avg} - 0.0018, n_{avg} - 0.0016, . . . , n_{avg}, . . . , n_{avg} + 0.002. The number 20 is just an assumption in the beginning, and if a more precise CWBG is required in the future, 100 or even more discrete

waveguide widths may be necessary. For a FBG which is photosensitive, the effective index variation can be realized by adjusting the intensity of the interferometer, or the period/phase of the phase mask. On the other hand, for a WBG with a planar structure, the effective index variation is made possible by changing some parameters of the waveguide, for example, by varying the width of the waveguide core in different positions of the grating. Obviously, if the width of the waveguide can only change by a very small range, for instance if the width can only vary from 1.000 μm to 1.001 μm, then such a narrow waveguide width step will be impossible even using the state-of-the-art e-beam lithography (EBL). On the other hand, if the width is made to change too much, say from 0.5 μm to 1.5 μm, then the scattering loss caused from the many periods of the CWBG will be too large and will affect the overall transmission severely. A delicate balance needs to be established here.

In [7], a comparison between a ridge waveguide (2-layer structure) and a strip waveguide (1-layer structure) was made on the SOI platform. A ridge waveguide cross-section was determined to be preferable, since the change of the waveguide width was large enough to be written by lithography. Ref. [22] [23] is also utilizing this kind of ridge waveguide for implementing a weak WBG. In this thesis, we propose that a 1-layer strip waveguide of Si_3N_4/SiO_2 is actually more appropriate, which also has the additional advantage of only one lithography step and one etching step.

To explain in more details, some simulation is done and the results are shown in Fig. 3.1. The figure shows the theoretically expected change of the effective index as the width of the Si_3N_4 waveguide varies, when the thickness of the Si_3N_4

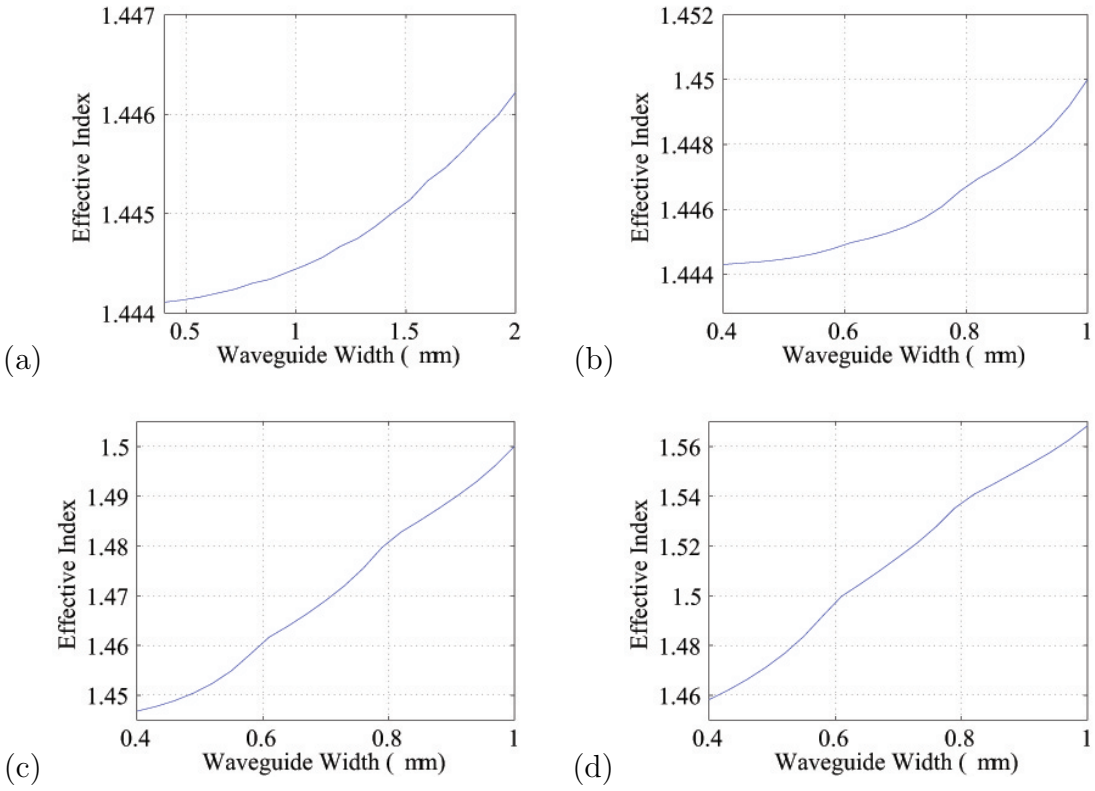

Figure 3.1: Theoretically expected effective index of the Si_3N_4/SiO_2 waveguide as the width and the thickness of the waveguide core vary. (a) the core width of the Si_3N_4/SiO_2 waveguide varies but its core thickness is kept constant as 50nm. (b) the core width of the Si_3N_4/SiO_2 waveguide varies but its core thickness is kept constant as 100nm. (c) the core width of the Si_3N_4/SiO_2 waveguide varies but its core thickness is kept constant as 200nm. (d) the core width of the Si_3N_4/SiO_2 waveguide varies but its core thickness is kept constant as 300nm.

waveguide is 50 nm, 100 nm, 200 nm and 300 nm respectively. Suppose now that a Si_3N_4 waveguide thickness of 200 nm or 300 nm is used to fabricated the WBG. In order to get an effective index change of 0.004, the width can only vary by $\sim$ 50 nm and $\sim$ 20 nm, respectively. If we simply divide this number by 20, this gives a width step of 2.5 nm and 1 nm, respectively. This means that in order to fabricate this CWBG, a series of waveguide widths such as 1 μm, 1.001μm, 1.002 μm, . . ., etc, need to be patterned clearly. It is impossible to write such small steps of the waveguide widths, even with the state-of-the-art EBL system. On the other hand, if the thickness of the Si_3N_4 waveguide is only 50 nm, then even when the waveguide width varies from 0.4 μm to 2 μm, the change of the effective index is only about 0.002. As a consequence, large scattering losses will occur if the thickness of the WBG is only 50 nm.

Fortunately, if the thickness of the Si_3N_4 waveguide is 100 nm, then, when the waveguide width changes from 0.4 μm to 0.9 μm, the effective index is changed by about 0.004. In this case, it is possible to write various waveguide widths varying between 0.4 μm and 0.9 μm using EBL with enough resolution, and the scattering loss may also be tolerable in practise. Moreover, later on in this thesis, we will prove that such Si_3N_4/SiO_2 grating is inherently compatible with the high coupling efficiency of a Si_3N_4/SiO_2 waveguide coupler, since 100 nm thick, 500 nm wide Si_3N_4 waveguide will give a coupling efficiency of 84 % to SMF28 fiber, 100 nm thick, 700 nm wide Si_3N_4 waveguide will give a coupling efficiency of 92 % to SM1500G80 fiber, and 100 nm thick, 900 nm wide Si_3N_4 waveguide will give a coupling efficiency of 96 % to UHNA3 fiber. The required waveguide widths would then need to be within

the range of 0.4 - 0.9 μm in order to realize the required range of effective index variation. Therefore, the high-efficiency, easy-to-fabricate Si_3N_4 waveguide couplers presented in the first part would be completely compatible with the fabrication of the CWBG here.

3.2 Assembling & Simulation of CWBG

The procedure to design the real CWBG is now pretty straightforward: from the LP/LA algorithm, the grating profile $q(z)$ or $\rho(z)$ is obtained initially, which can be related to the effective index variation $n(z)$ along the grating. This range of the effective index variation is then mapped to a 1-layer waveguide structure with varying widths. It means one specific waveguide width will correspond to one specific effective index. In reality, the mapping is realized by a Matlab script with a loop.

This mapping process is realized by using FIMMWAVE / FIMMPROP from Photon Design. A simple 1-layer waveguide is drawn in the software, and the effective index is plotted versus the width of the waveguide. So the mapping process can be executed, which converts the output of LP/LA algorithm to an aperiodic array of width for a complex waveguide.

For a real CWBG which is about $2cm-3cm$ in length, it is generally discretized into $200'000-300'000$ small individual segments. Each segment is a tiny rectangle, with a length of 100 nm and a fixed width obtained from the mapping process before. The segment number $200'000-300'000$ is not a fixed constant in the algorithm. In

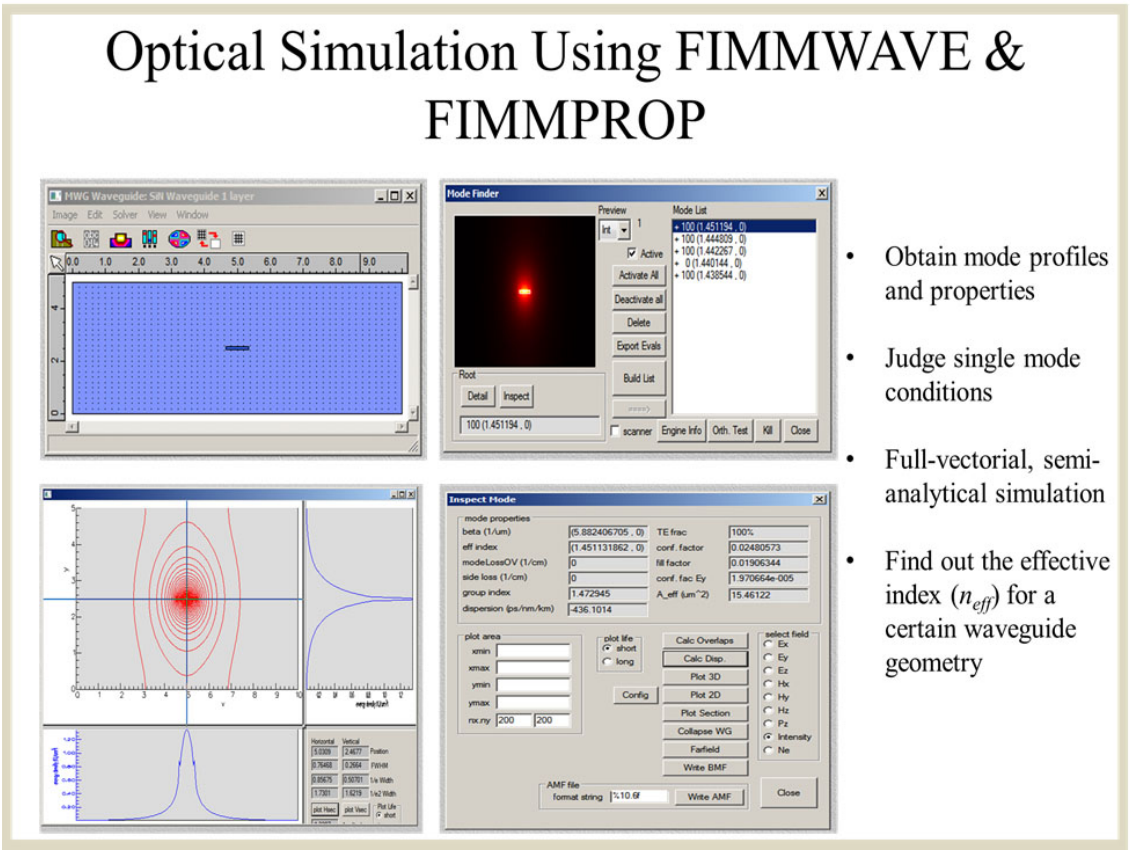

Figure 3.2: Optical simulation using FIMMWAVE / FIMMPROP: calculating the mode profile parameters and mapping the effective index to a real waveguide shape.

fact, the most appropriate segment number depends on the application. In the following text, we assume that we are dealing with 200'000 segments in our design. The number of waveguide segments equals to the numbers in the grating's effective index array. In other words, if there is 200'000 points in the effective index profile, there will also be 200'000 small segments which constitute the whole CWBG.

So far, it is possible to obtain the widths of the grating, and now a complete GDSII file is required for the subsequent EBL. Since these 200'000 segments are not periodic at all, another Matlab script is written to remotely control the assembling of CWBG in FIMMWAVE / FIMMPROP. The advantage is that, after the grat-

ing assembling, the 3D aperiodic grating structure can be simulated using Finite Difference Method (FDM) and Eigen Mode Expansion (EME) in FimmPROP. The process of effective index mapping, grating assembling and 3D simulation is shown in Fig. 3.2 and Fig. 3.3.

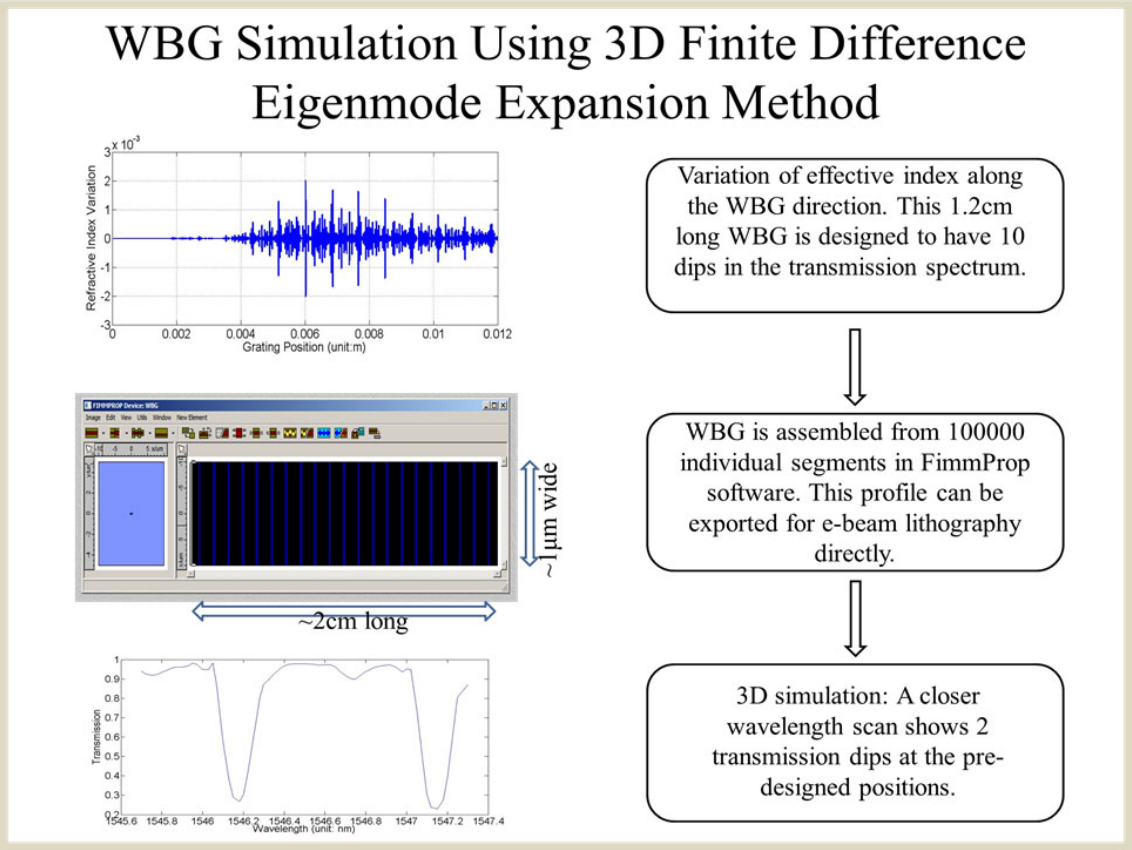

Figure 3.3: Assembling & 3D simulation of CWBG in FIMMWAVE / FIMMPROP with the help of Matlab scripts. As shown in the first sub-figure, the width/profile of the CWBG is highly aperiodic for a random spectrum. The 3D simulation also shows spectral notches at their prescribed positions in the spectrum.

To be honest, we are the first group in the world who attempts to construct a complex waveguide grating with 200'000 aperiodic segments. Although FIMMWAVE / FimmPROP is a good and reliable software, it is still really time-consuming to assemble all the 200'000 individual segments in FIMMWAVE / FIMM-

PROP. As far as we are concerned, no other group has ever simulated such a complex waveguide grating with so many aperiodic segments. In the 3D simulation, we need to calculate each one of the 200'000 segments (because of aperiodicity) for all the wavelength points. Therefore the 3D simulation takes a even longer time (from a few days to a few weeks 24/7 unceasingly) to execute, as FIMMWAVE / FIMMPROP has to calculate the overlap integral for all the interfaces of the 200'000 segments one by one. And each run is only for a single wavelength. In the spectrum, there may be 10′000 or even more spectral points, so the overall time is just 10′000 times that. A future powerful upgrade of FIMMWAVE / FIMMPROP to support such intensive calculations will give much faster simulation results.

Chapter 4: Fabrication & Experimental Results

4.1 Nano-Fabrication Process

The fabrication starts with a silicon wafer with a 5 μm thermal SiO_2 layer on top. A 100 nm thick Si_3N_4 layer is first deposited using low-pressure chemical vapor deposition (LPCVD). Then the profile of the CWBG is patterned by e-beam lithography (using a Raith e-line instrument), and a chromium hard mask is made by e-beam deposition and subsequent lift-off. After that, reactive-ion etching (RIE) is performed, followed by chromium removal and another 5 μm SiO_2 film deposition from plasma-enhanced chemical vapor deposition (PECVD), as the upper cladding layer. Finally, the thickness of the sample is polished to about 100 μm from the back-side, which facilitates ease of subsequent end-facet cleaving. Because the CWBG has a simple one-layer structure, the fabrication process requires only one lithography step and one etching step. We control the stitching error by doing very precise writefield (WF) alignment, and also by overlapping neighboring WFs slightly with each other. The whole device is stitched and connected without any stitching gaps between two WFs. It typically takes about 1-1.5 hours to write a CWBG.

For those readers who are interested, the whole nano-fabrication process is listed step by step in the Appendix.

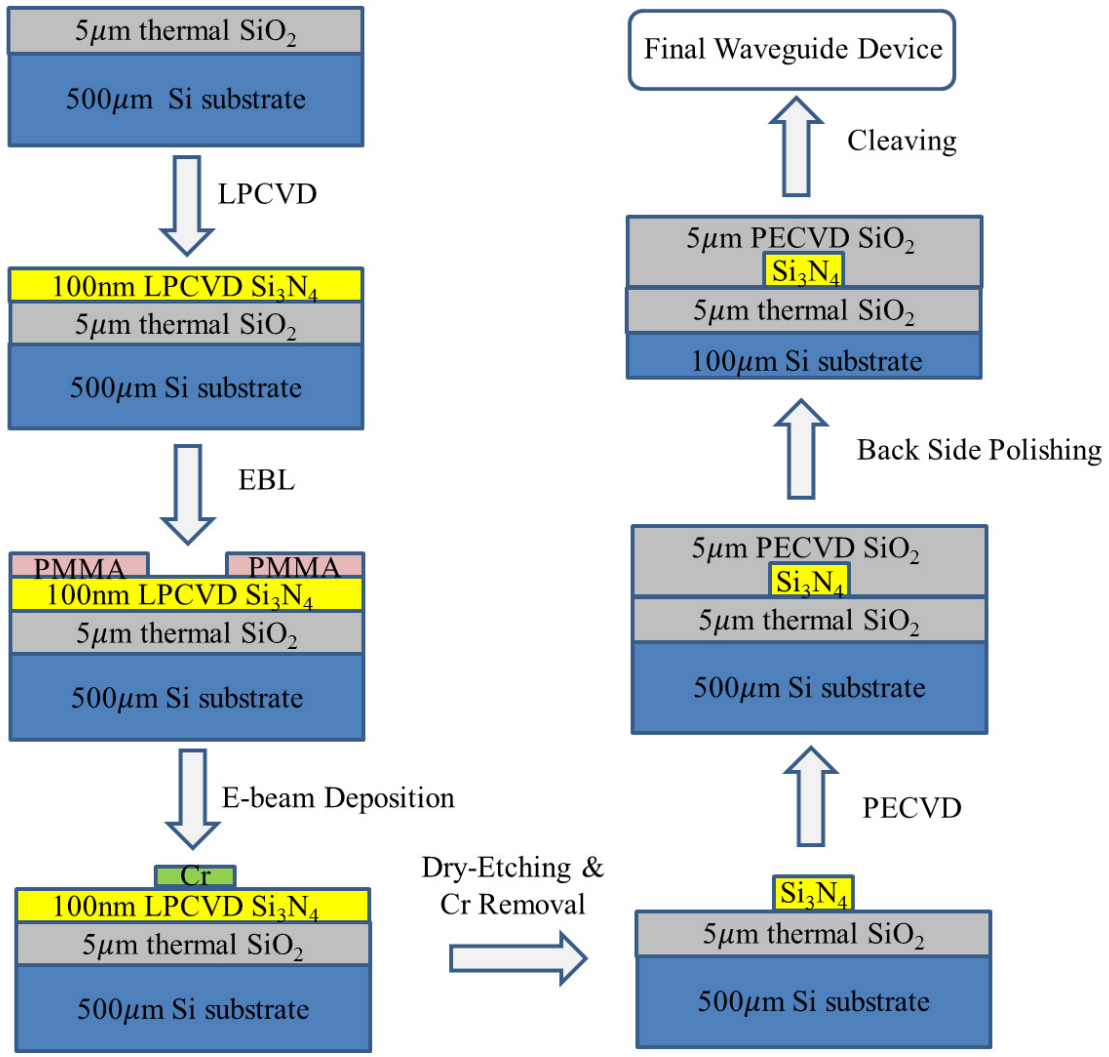

Figure 4.1: Fabrication procedures of the Si_3N_4/SiO_2 waveguide coupler with waveguide core thickness of 100 nm. The end-facet cleaving process does not need high position accuracy, because we add a narrow straight waveguide on both ends of the device. We optimized the end-waveguide geometry to achieve high coupling efficiency, and the cleaving should be fine as long as it occurs somewhere along the straight waveguide.

4.2 Some Tricks and Discussions about E-beam Lithography (EBL)

As we are doing nano-fabrications, it is important to show some Scanning Electron Microscope (SEM) figures of our real waveguide patterns. For our CWBGs which have continuously-varying waveguide widths and small theoretical feature size of less than 10 nm, a stable EBL with high resolution will be really beneficial.

4.2.1 Settings for Focus, Stigma and Aperture

One of the major issues with our current Raith EBL system is not even the machine itself, but the person who actually operates the machine. The reason is that all the adjustments about focus, stigma and aperture are judged and optimized manually by that person. These adjustments (especially stigma adjustments) can be a little tricky for people without too much SEM experience. It does take quite a lot of practise and real sample processings to learn and get familiarized.

Fig. 4.2 demonstrates a good contamination-spot with decent focus, aperture and stigma. The contamination spot, burned here using left-click quick-burn in the Raith system, should have a diameter of about only $20 - 30nm$. This spot should be sharp and clear under the magnification of at least $100K$. This is an important step before real patterning begins.

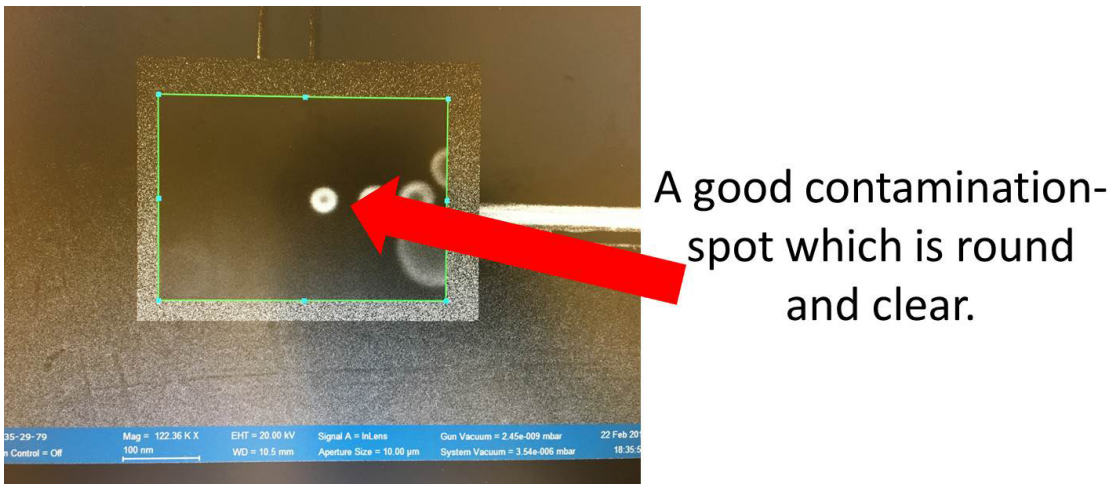

Figure 4.2: The settings/adjustments about focus, stigma and aperture are important for a successful EBL pattern. On our Raith e-line EBL system, the best way of judging these settings is to burn small contamination-spots. Under at least $100K$ magnification, a good contamination-spot (with a radius of about 20 - 30 nm) should look round, clear and sharp all over its outer circumference.

4.2.2 Active Focus-Adjustment for Large Patterns: Laser Height Sensing (LHS)

Another small but really useful trick I always use is the Laser Height Sensing (LHS). It is a active focus-adjustment technique for large patterns with big dimensions and many writefields, especially our centimeter-sized waveguides and waveguide gratings. Fig. 4.3 demonstrates very clearly why LHS is beneficial for large patterns.

The basic principle of LHS is quite simple: a laser is projected onto the sample surface and is reflected and detected by the detector, which measures the height of the current writefield. The system then adjusts either the height of the sample or the working distance of the beam to guarantee perfect focus condition. Once it is switched on, LHS will be performed for focus-adjustment before the patterning of

every writefield. Fig. 4.4 shows the principle and operation of LHS clearly.

Although LHS is optional in our Raith EBL system, I still highly recommend using this function if the pattern has dimensions larger than a few millimeters. It is worth noting that on some of the newer EBL systems, such as the new 100kV EBL system used in Joint Quantum Institute (JQI), University of Maryland, LHS becomes a necessary step.

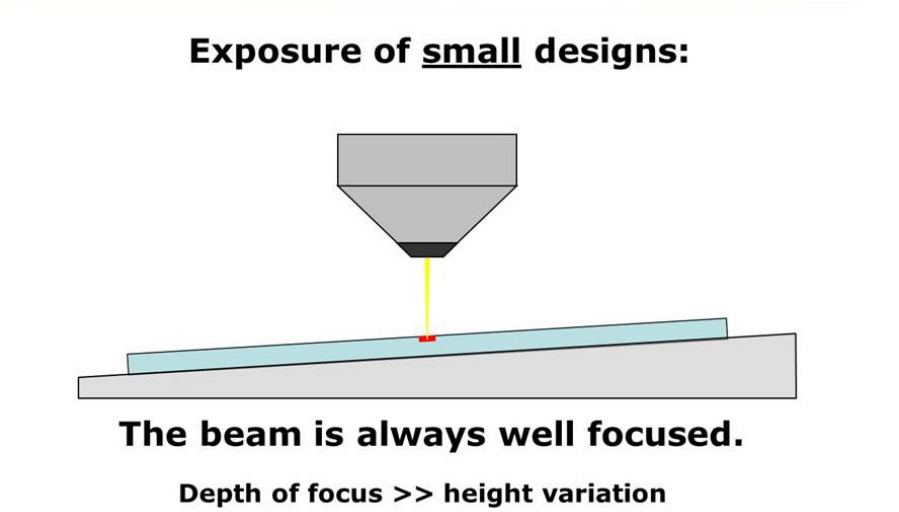

(a)

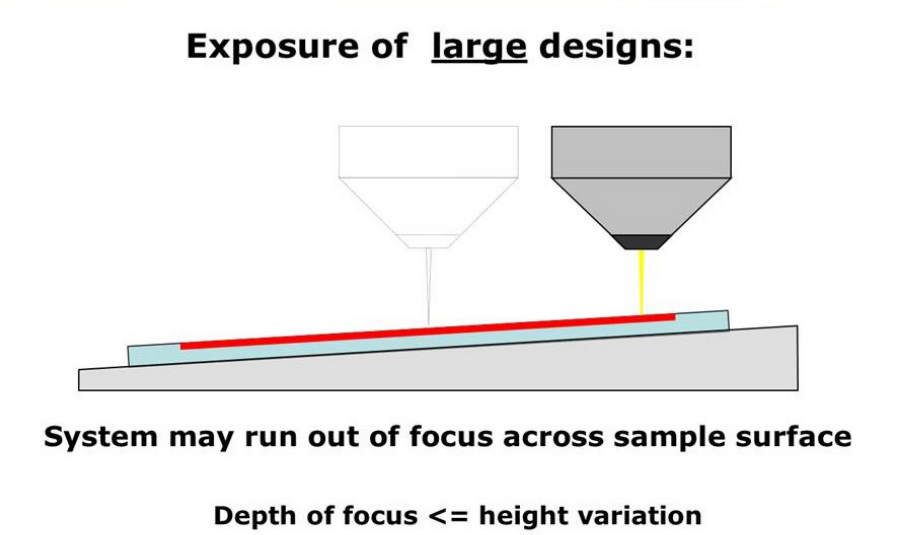

(b)

Figure 4.3: The reason why active focus-adjustment is really beneficial for large patterns. (a) For small pattern within only one writefield, the beam is always well focused. (b) For large patterns, the beam will only be perfectly focused in one writefield. At other writefields, the beam will be out of focus.

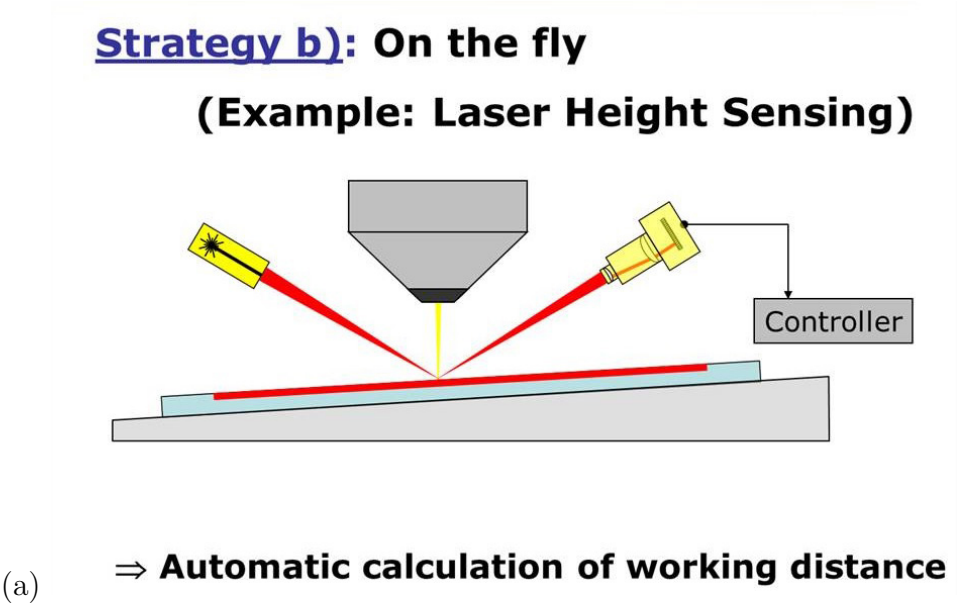

(a)

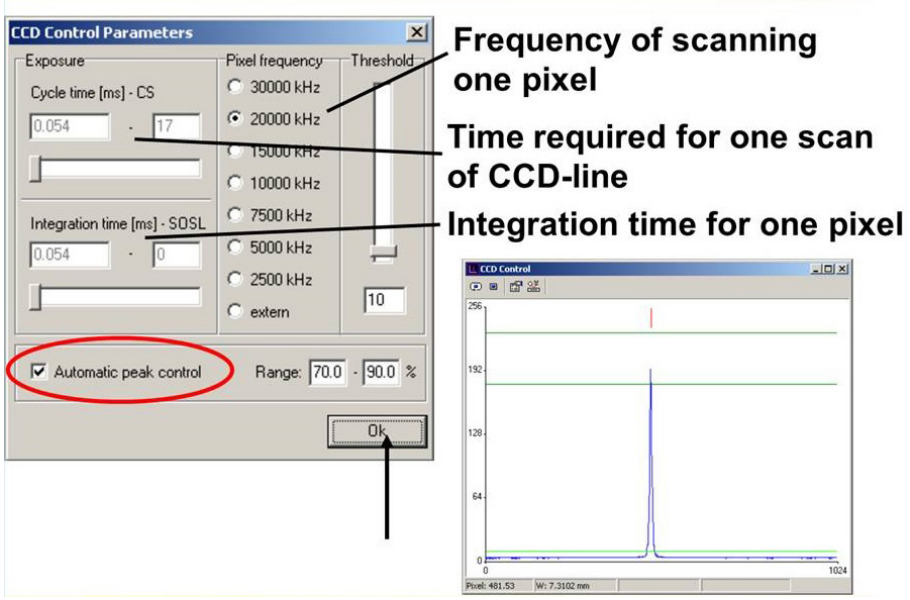

(b)

Figure 4.4: Principles and settings/operations of LHS. (a) Principle of LHS. (b) Operation window for LHS. It is recommended that LHS be switched on for large patterns.

4.2.3 Stitching Error

Stitching error is also a very common problem in e-beam lithography, and it can be due to a lot of reasons. The beam will jump between neighboring writefields, and this can cause the two writefields to be stitched with an offset, as shown in Fig. 4.5.

On our Raith machine, there is a Fixed Beam Moving Stage (FBMS) configuration which can eliminate the stitching error. The reason behind it is actually quite simple: FBMS commands the beam to go from the beginning to the end without any jumps. A beam jump from one writefield to the next writefield causes the stitching error. When using the FBMS feature, the whole big pattern is no longer separated into small writefields. Instead, the beam will move continuously from one end of the waveguide to the other end with no jump.

FBMS does not come for free, and it does have two big trade-offs. The first trade-off is the limitations of the patterns FBMS can handle. It handles only simple patterns, such as straight waveguides and circles. FBMS cannot write a CWBG with $200,000$ individual segments, each with its own width. Secondly, FBMS does not allow the Laser Height Sensing, which is the feature of active focus-adjustment. The consequence is that using FBMS, the pattern will be perfectly focused only in one location, and will be more or less defocused in other positions.

Personally, I will not recommend using FBMS (unless stitching error is a very severe problem), because it cannot write complex waveguide gratings with constantly-varying widths, and it does not support LHS for active focus-adjustment.

To overcome the stitching error, a layer of conducting polymer (such as aqua-save) on top of the sample surface and a careful EBL process will help a lot already.

Finally, two SEM figures of a real 47-notch grating are shown below in Fig. 4.6. A EBL patterning like this will be proper for subsequent experimental characterizations.

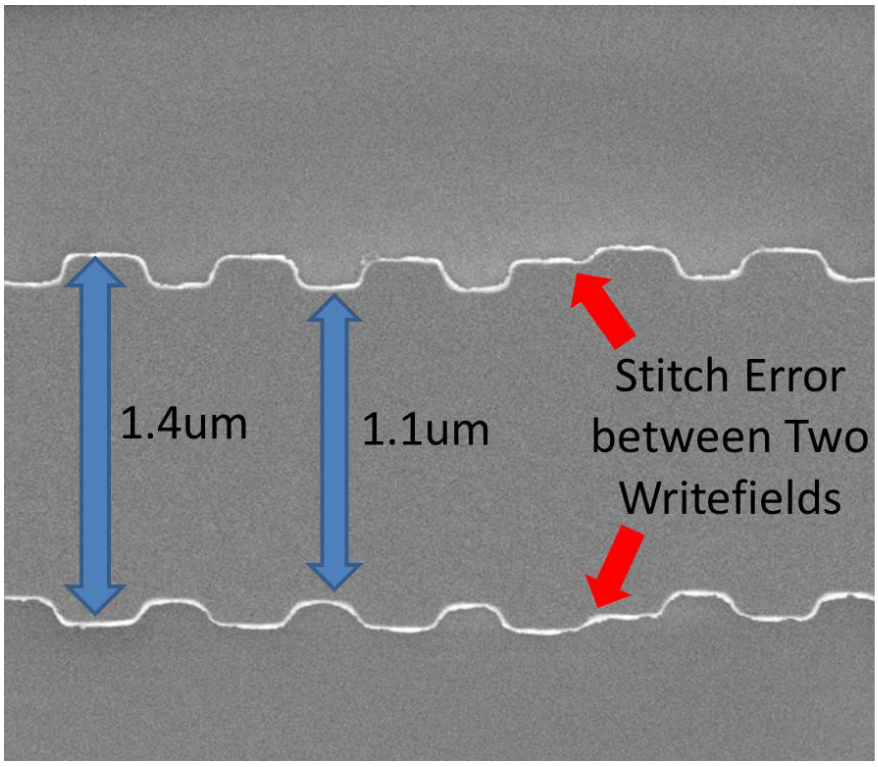

Figure 4.5: A demonstration of stitching errors between two neighboring writefields (WF), caused during improper setting/alignment in the e-beam lithography.

(a)

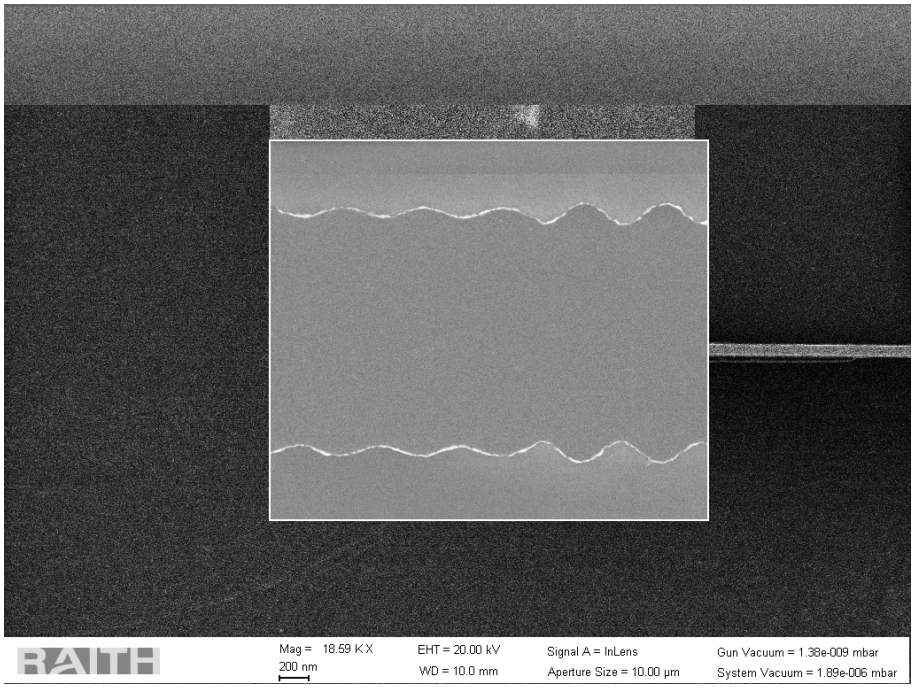

(b)

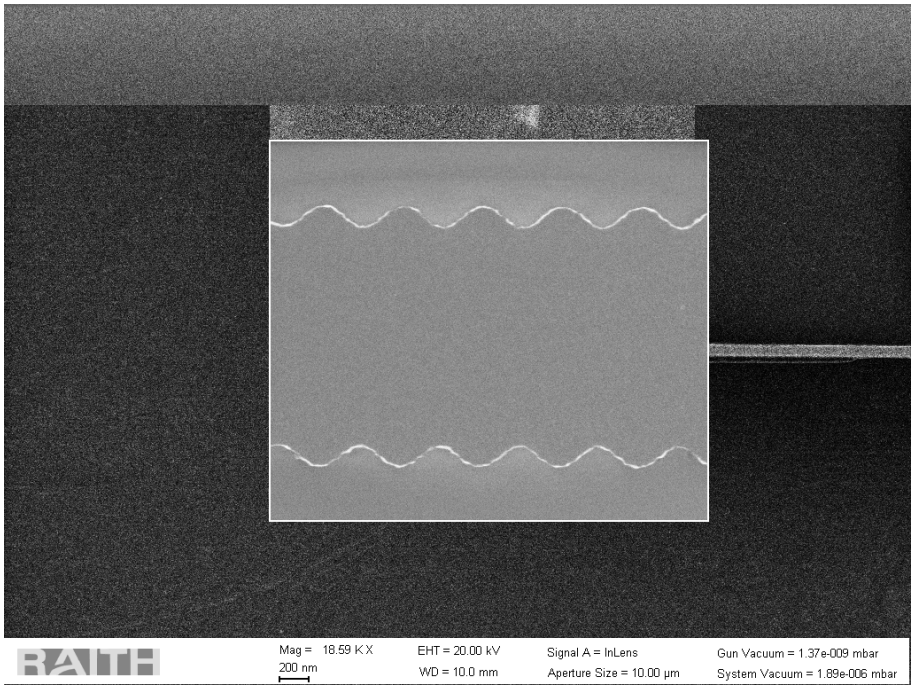

Figure 4.6: SEM figures of a real 47-notch grating. (a) The joint section between two Δ segments (see Chapter 2 for definition of Δ) which have different complex coupling efficiencies $q(z)$. (b) A section within one Δ segment.

4.3 Experimental Set-up

To characterize the transmission spectrum of the CWBG, a TE polarized broadband light source covering 1500 nm − 1600 nm is used. The light travels in a polarization-maintaining (PM) fiber, PM1550-XP, and is launched into the CWBG with an automatic XYZ stage. The output light is collected from the other end of the CWBG with another XYZ stage, and is finally analyzed by an Optical Spectral Analyzer (OSA, YOKOGAWA AQ6370C). The resolution of our OSA is 0.004 nm. In this case, the effective index is taken from the fundamental TE waveguide mode in the design, so both the fiber-rotator and the PM fibers are employed to guarantee the TE polarization of the input light.

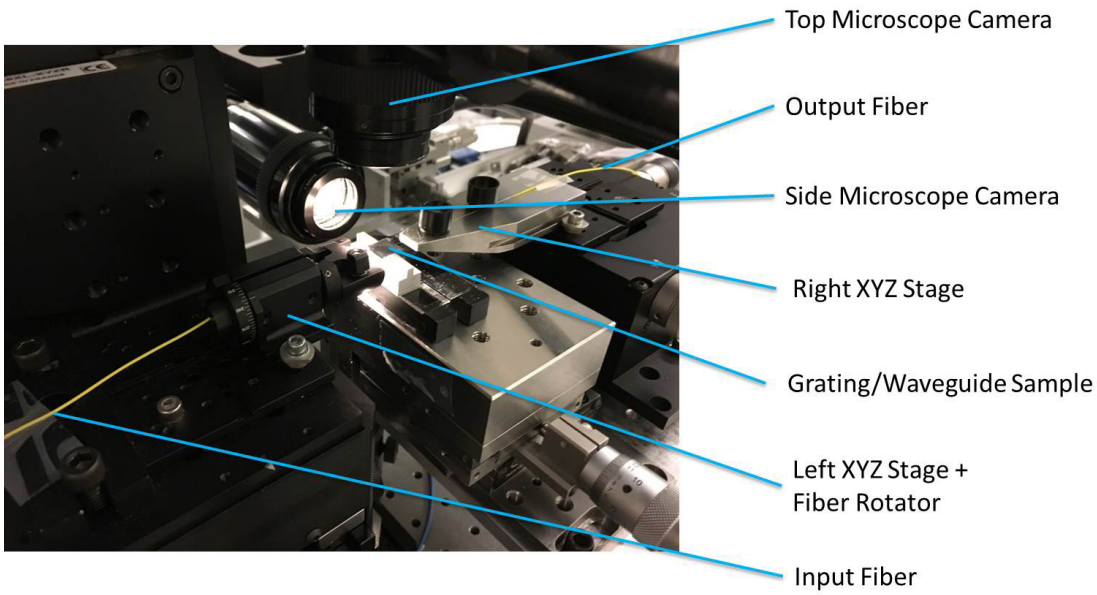

Figure 4.7: Experimental set-up for the waveguide performance measurement, showing two XYZ stages which hold input and output fibers, two microscope cameras for fiber/waveguide alignment and a waveguide sample mounted in the middle.

4.4 Flow-Diagram of the Whole Theoretical and Experimental Procedures

Before we move on to some of our experimental results, let's first summarize all the steps from theory to experiment. Fig. 4.4 shows a complete flow diagram of the calculation, design, fabrication and characterization processes.

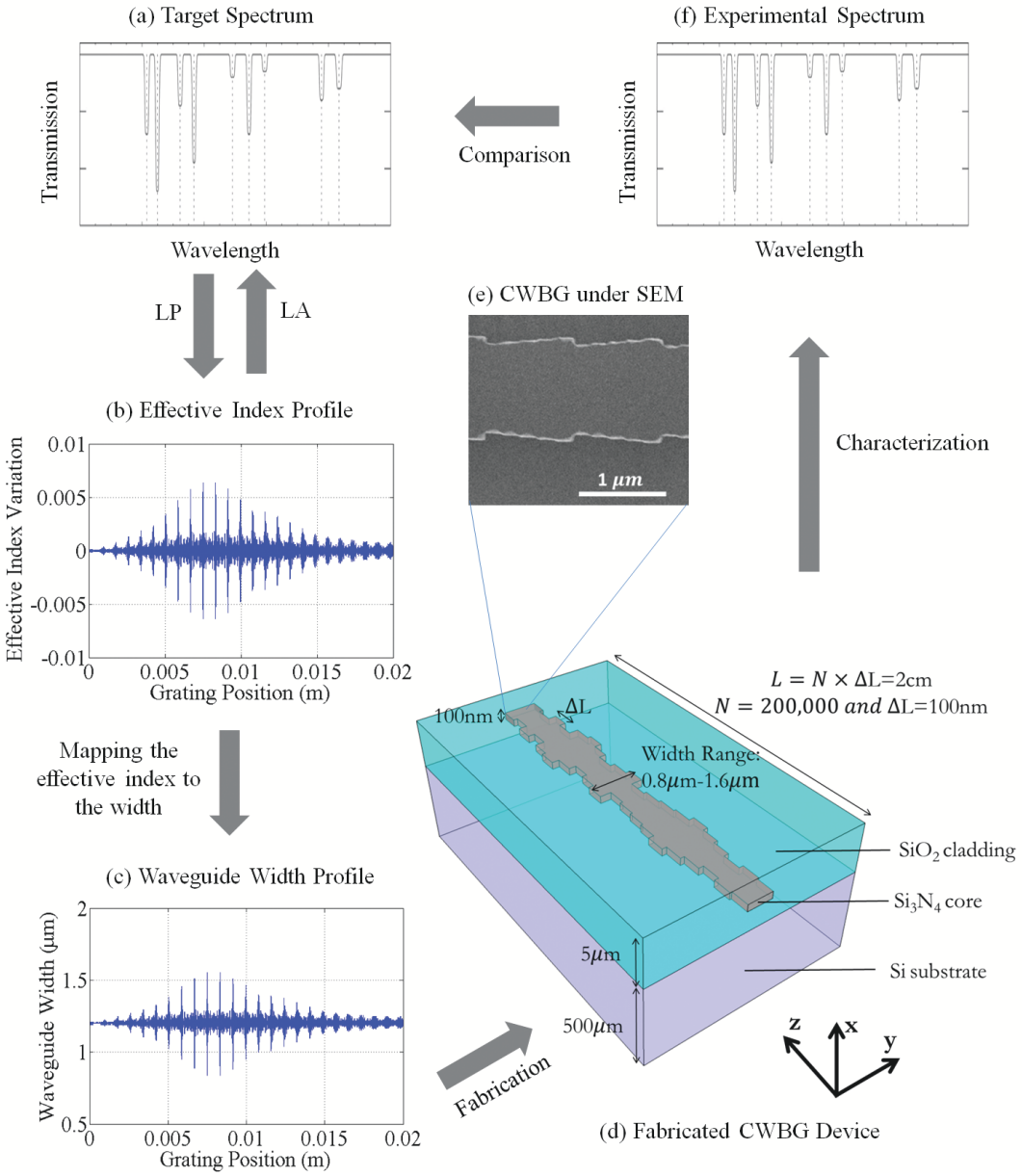

Figure. 4.4 (a) The design of a specific CWBG device starts with a target transmission spectrum with an arbitrary shape. (b) The effective index profile is calculated/examined using LP/LA algorithm. (c) The effective index is mapped to the actual width profile of the CWBG. (d) One-layer CWBG device implemented on a silica-on-silicon platform. In this case, the width is continuously varying in the y-direction, while the thickness remains the same. Light propagates along the z-direction. (e) SEM picture showing a portion of the actual CWBG with continuously varying width. (f) The performance of the CWBG device is characterized experimentally.

4.5 Experimental Results

4.5.1 First Generation: 20-Notch CWBG

Fig. 4.8 shows both the simulation and the experimental transmission spectrum for our current CWBG device, which removes 20 randomly distributed narrow spectral lines between 1530 nm and 1560 nm simultaneously. The 3 dB bandwidths for all these spectral notches are $0.3 - 0.4$ nm, in agreement with the simulation results. The sloping transmission vs wavelength in Fig. 4.8 is due to the losses from O-H and N-H bonds near 1.5 μm associated with the PECVD process; these losses will be reduced in the future via thermal annealing. The remaining losses are due to fiber-to-waveguide coupling at the two facets of the CWBG device and propagation/scattering loss through the waveguide.

Table 4.1 summarizes and compares the positions of the experimental transmission notches of the CWBG with its theoretical values. And Table 4.2 lists the major parameters and experimental performance of the CWBG device. All the spectral lines are suppressed by at least 15 dB, while some of the deepest notches reach as much as 33.6 dB. The variance in the suppression ratios is due to the limited resolution of the current fabrication process. To explain it briefly, just recall that our designed CWBG has a width that varies between 800 nm and 1.6 μm, corresponding to the range of effective index variation (± 0.0064). In order to further map each discretized width to the varying effective index precisely, a small width step is desirable. In our case, the actual waveguide widths are designed to be 800 nm, 808 nm, 816 nm,

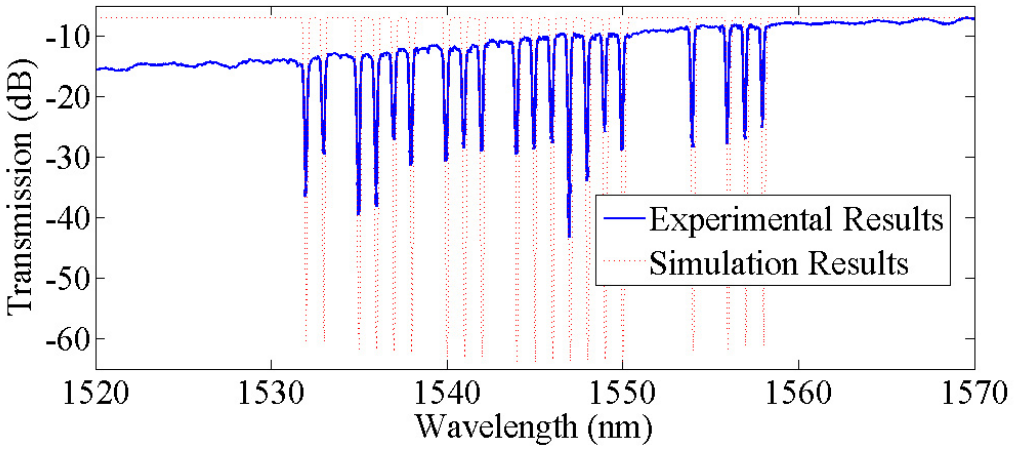

Figure 4.8: Experimental Transmission Spectrum of a fabricated CWBG device, showing the removal of 20 prescribed narrow spectral lines simultaneously. Simulation results are also plotted as a comparison. As a proof-of-principle demonstration, these 20 lines are designed to be randomly distributed. See Table 4.1 for detailed comparisons between target wavelengths and experimental wavelengths. The slope in the transmission is due to the O-H and N-H bond absorption that can be corrected via annealing in the future. The major parameters of this CWBG device are listed in Table 4.2.

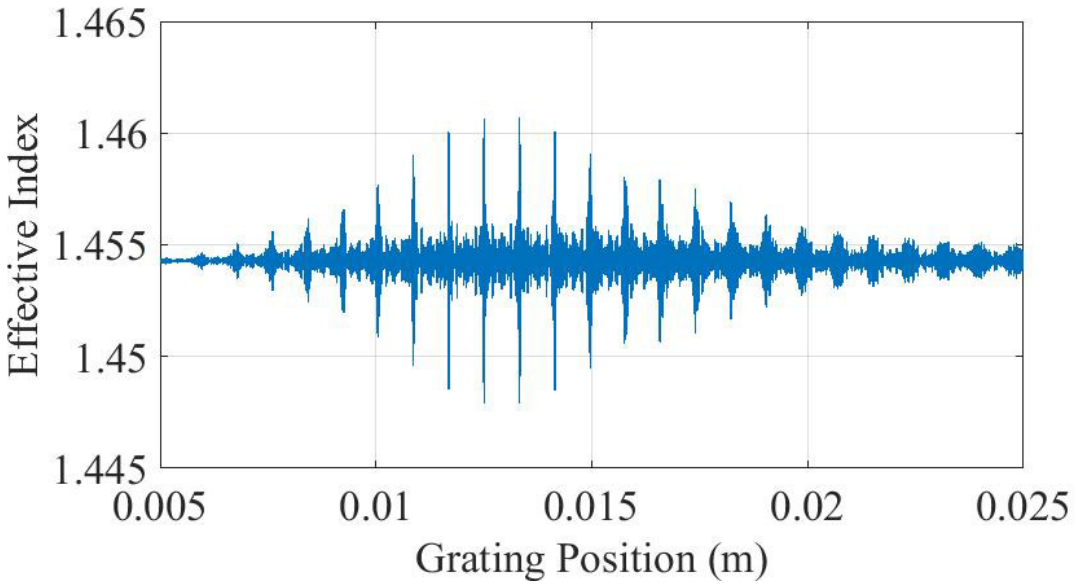

Figure 4.9: The effective index variation along the grating whose spectrum is shown in Fig. 4.8. The effective index is calculated from the Layer Peeling algorithm, and is varying in an aperiodic way.

..., 1592 nm, 1600 nm, with a step of 8 nm. In other words, the continuously-varying effective index of ± 0.0064 is sampled into $(1600 - 800)/8 + 1 = 101$ discretized values. We have also found out that smaller steps (e.g. 4 nm or 2 nm) do not improve the CWBG performance in our simulations. This 8 nm width step can be considered ideal for our CWBG design, but in practice, such a small step cannot easily be patterned using a state-of-the-art e-beam lithography, because this length resolution stretches the capability of the instrument. This is why the suppression ratios in our experiment is not exactly the same for all the 20 notches.

It is worth noting that other authors have approached this same problem from the point of view of volume holography, using a 2-layer SOI waveguide structure fabricated by deep-UV lithography [22,23]. Large differences between the theory and the experimental realization are observed. The theory assumes small index variation so the second-order reflections are neglected, which is good enough for weak gratings, but not suitable for gratings with both deep and narrow notches. By comparison, our LP/LA algorithm makes no such assumptions, and can be applied to any arbitrary spectrum. Moreover, we experimentally demonstrate that one can design a CWBG with a simpler one-layer waveguide structure, fewer fabrication steps, deeper and narrower notches, and better spectral precision. This makes CWBG promising for various applications, especially in astrophysical observations.

Table 4.1: Comparison between the theoretical simulations and experimental results for our first generation CWBG. Our goals were to reach spectral precision ($\lambda_{\text{target}} - \lambda_{\text{experiment}}$) better than ± 0.1 nm, 3dB bandwidths (FWHM) of about 0.3 nm, and suppression ratios larger than 15 dB. All these technical requirements were achieved experimentally.

Channel Number	λ_{target} (nm)	$\lambda_{\text{experiment}}$ (nm)	$\lambda_{\text{target}} - \lambda_{\text{experiment}}$	Notch Depth (dB)
1	1532.000	1531.940	0.060	22.2
2	1533.000	1533.000	0.000	16.4
3	1535.000	1534.932	0.068	26.4
4	1536.000	1535.988	0.012	24.9
5	1537.000	1536.972	0.028	15.1
6	1538.000	1537.912	0.088	19.3
7	1540.000	1539.920	0.080	18.9
8	1541.000	1540.936	0.064	16.9
9	1542.000	1542.024	-0.024	17.5
10	1544.000	1543.960	0.040	18.7
11	1545.000	1544.940	0.060	18.5
12	1546.000	1546.004	-0.004	17.5
13	1547.000	1546.932	0.068	33.6
14	1548.000	1547.944	0.056	24.0
15	1549.000	1548.964	0.036	16.0
16	1550.000	1549.936	0.064	19.4
17	1554.000	1553.972	0.028	20.0
18	1556.000	1555.932	0.068	19.5
19	1557.000	1556.968	0.032	18.8
20	1558.000	1557.924	0.076	16.7

Table 4.2: Major parameters of the fabricated first generation CWBG device.

Parameter	Value
Overall CWBG Length(L)	$2cm$
Length of Each Segment in LP/LA Before Discretization (Δ)	$10\mu m$
Number of Segments in LP/LA	2000
Length of Each Discretized Segment (ΔL)	$100nm$
Number of Discretized Segments	$200,000$
Maximum Effective Index Variation	± 0.0064
Si_3N_4 Core Width Range	$800nm - 1.6\mu m$
Si_3N_4 Core Thickness	$100nm$
SiO_2 Cladding Thickness	$5\mu m$ top and $5\mu m$ under
Number of Spectral Notches	20
Suppression Ratios	$15dB - 33dB$
$3dB$ Bandwidth	$0.3 - 0.4nm$
Spectral Precision	$\pm 0.1nm$

4.5.2 Second Generation: 47-Notch CWBG

Based on the first generation of CWBG, we designed and fabricated the second generation of CWBG, which has 47 notches between 1510 nm and 1610 nm. Fig. 4.10 shows the experimental transmission spectrum of these notches, and Table 4.3 and Table 4.4 give a detailed comparison between theoretical and experimental spectral positions. Fig. 4.11 gives the effective index variation of this grating. And the major parameters of this CWBG device are listed in Table 4.5. Again, even though the effective index seems chaotic, its transmission spectrum regenerates these notches very precisely. High spectral precision is achieved again.

It is noted that there is a big absorption dip at the wavelength of 1500 nm. It is caused by the O-H and Si-H bonds introduced in the nano-fabrication process. In the next chapter, we will provide solutions to remove this big absorption dip.

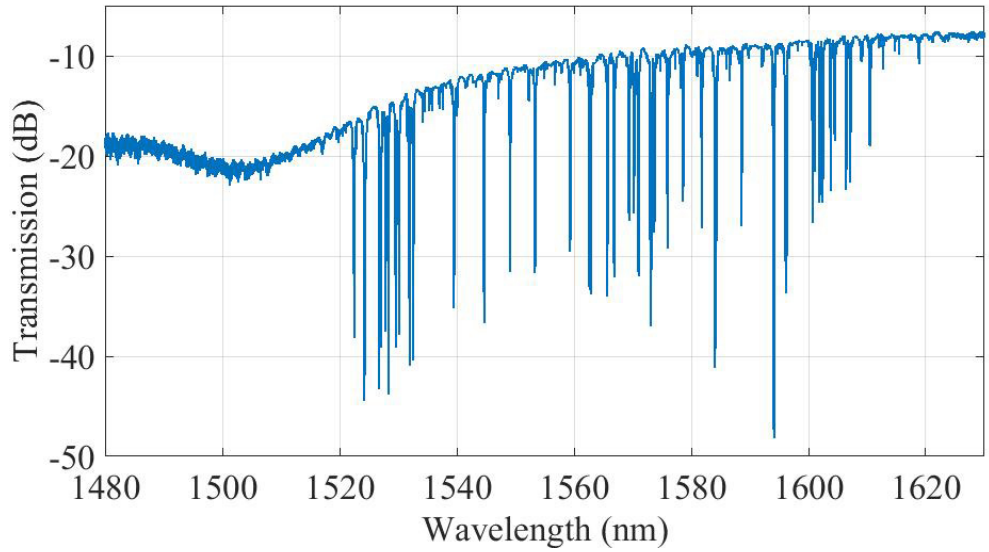

Figure 4.10: Experimental Transmission Spectrum of a fabricated CWBG device, showing the removal of 47 prescribed narrow spectral lines simultaneously. See Table 4.3 and Table 4.4 for detailed comparisons between the target wavelengths and the experimental wavelengths. There is a big absorption dip at around 1500 nm, which will be discussed and solved in the next chapter. The major parameters of this CWBG device are listed in Table 4.5.

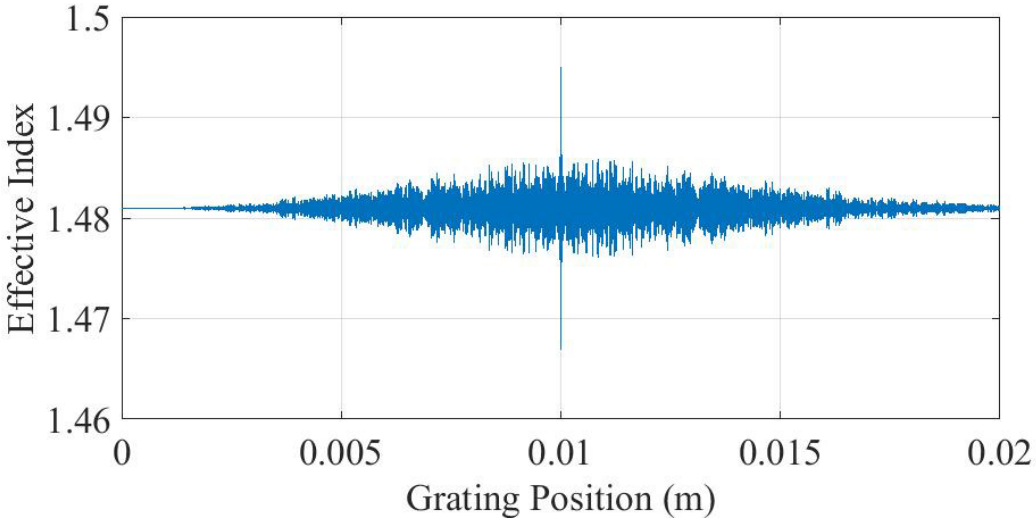

Figure 4.11: The effective index variation along the grating whose spectrum is shown in Fig. 4.10. The effective index is calculated from the Layer Peeling algorithm, and is varying in an aperiodic way.

Table 4.3: Comparison between the theoretical and experimental spectral positions for our second generation CWBG. Please note the high spectral precision ($\lambda_{\text{target}} - \lambda_{\text{experiment}}$) achieved with this grating.

Channel Number	λ_{target} (nm)	$\lambda_{\text{experiment}}$ (nm)	$\lambda_{\text{target}} - \lambda_{\text{experiment}}$ (nm)
1	1522.583	1522.636	-0.05299996
2	1524.335073	1524.34	-0.004927216
3	1524.508938	1524.516	-0.007062489
4	1526.973989	1526.98	-0.006011064
5	1527.229549	1527.216	0.013549136
6	1528.03365	1528.056	-0.022350308
7	1528.506779	1528.5	0.006778841
8	1529.77144	1529.764	0.007440011
9	1530.344737	1530.352	-0.00726343
10	1532.163461	1532.156	0.007460633
11	1532.767226	1532.808	-0.040773633
12	1539.755617	1539.728	0.027617164
13	1544.878152	1544.86	0.018151894
14	1549.336459	1549.316	0.020458622
15	1553.5831	1553.56	0.023099804
16	1559.573625	1559.532	0.04162514
17	1562.889052	1562.86	0.029052179
18	1563.078723	1563.06	0.01872279
19	1565.931494	1565.896	0.035494459
20	1567.082087	1567.04	0.042086657
21	1569.619122	1569.572	0.047121507
22	1570.466736	1570.396	0.070735852
23	1571.238082	1571.204	0.034082046
24	1573.316937	1573.228	0.088936685
25	1573.434433	1573.364	0.070433439

Table 4.4: Continued with the last table.

Channel Number	λ_{target} (nm)	$\lambda_{\text{experiment}}$ (nm)	$\lambda_{\text{target}} - \lambda_{\text{experiment}}$
26	1573.928986	1573.888	0.040986226
27	1576.215317	1576.18	0.0353169
28	1578.830334	1578.816	0.014333793
29	1582.048926	1582.016	0.032925987
30	1584.286887	1584.24	0.046886847
31	1584.403431	1584.368	0.035431439
32	1584.553016	1584.56	-0.006983958
33	1588.816606	1588.804	0.012605702
34	1594.269731	1594.24	0.029730975
35	1594.365328	1594.36	0.005328009
36	1596.300787	1596.304	-0.003212903
37	1596.484269	1596.508	-0.023731344
38	1600.981519	1600.992	-0.010481202
39	1601.261073	1601.272	-0.010926527
40	1602.139824	1602.16	-0.020176494
41	1602.668845	1602.676	-0.007155454
42	1604.042243	1604.076	-0.033757417
43	1604.691331	1604.724	-0.032668787
44	1606.66421	1606.692	-0.027789744
45	1607.347481	1607.384	-0.036518508
46	1610.679	1610.732	-0.052999936

Table 4.5: Major parameters of the fabricated first generation CWBG device.

Parameter	Value
Overall CWBG Length(L)	$2cm$
Length of Each Segment in LP/LA Before Discretization (Δ)	$4\mu m$
Number of Segments in LP/LA	5000
Length of Each Discretized Segment (ΔL)	$100nm$
Number of Discretized Segments	$200,000$
Maximum Effective Index Variation	± 0.014
Si_3N_4 Core Width Range	$400nm - 2\mu m$
Si_3N_4 Core Thickness	$100nm$
SiO_2 Cladding Thickness	$5\mu m$ top and $5\mu m$ under
Number of Spectral Notches	46
Suppression Ratios	$10dB - 39dB$
$3dB$ Bandwidth	$0.3 - 0.4nm$
Spectral Precision	$\pm 0.1nm$

Chapter 5: Discussions & Further Improvements

5.1 Fully-tunable CWBG

In the previous section, although a powerful CWBG has been experimentally fabricated to remove 20 prescribed spectral dips, there is still a critical problem which remains unanswered: what if those spectral notches are not exactly in their desired locations in the spectrum? How about those dips are all shifted to the left or to the right in the spectrum? This can be a serious problem, as the theoretical index used in the simulation may not be exactly the same as the real index of the CWBG materials. As a very simple example, if we want to design a spectral dip which is centered at 1550.00 nm, in practice the notch may be centered at 1546.55 nm.

To solve this problem, a method which can fully adjust the positions of the spectral notches is found. The basic principle behind this method is this: if the real index of the CWBG is larger than the theoretical index of the CWBG used in the design, then the spectral locations of the real notches will be on the longer-wavelength side of the original desired positions, i.e. they will be red-shifted in practice. So, if we want the real notches be in the right place, we need to increase the theoretical index correspondingly.

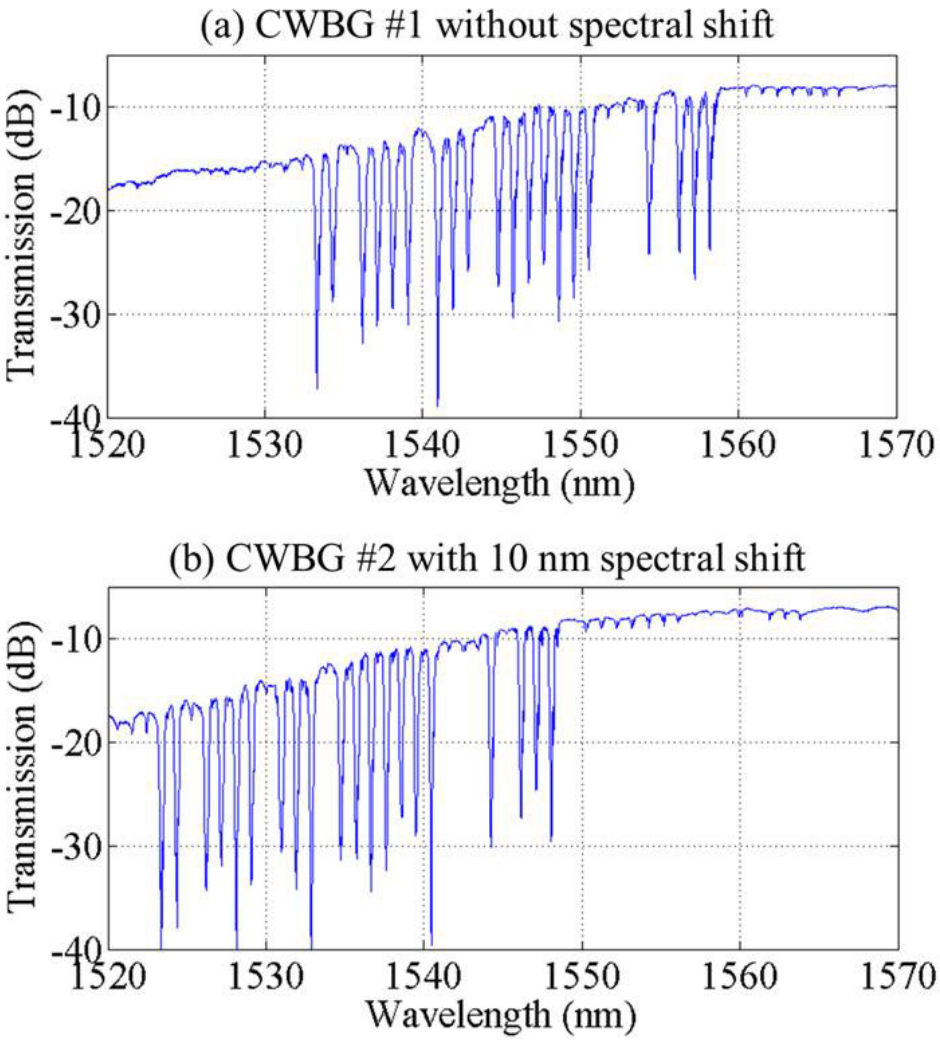

Figure 5.1: Demonstration of a fully-tunable CWBG (a) Originally fabricated CWBG whose spectral notches are not shifted. (b) A second CWBG with modified parameters, whose spectral notches are all shifted 10 nm to lower wavelength.

Experiment is performed to verify this idea, and it proves to be a successful solution. Two CWBGs (CWBG_1 and CWBG_2) are fabricated both with 20 spectral notches. Every parameter is set to be equal for these two CWBGs, but the theoretical index of CWBG1 is set to be 0.01 smaller than the index of CWBG_2. As the theoretical index of CWBG_2 is higher than that of CWBG_1, the notches of CWBG_2 should be shifted 10 nm left with respect to CWBG_1. This theoretical

prediction is fully verified by the experimental results, as shown in Fig. 5.1.

Therefore, the spectrum of the CWBG can be fully tuned, just by changing a parameter in the algorithm. The fabrication process will always remain the same and straightforward. Using the same principle, separations of the neighboring notches can also be tuned precisely, also simply by adjusting the designed notch position accordingly.

5.2 Annealing

As shown in the last chapter, there is a very obvious absorption dip in the transmission spectrum of our 47-notch grating. This absorption dip is indicated by the arrow in Fig. 5.2 (a), and it appears clearly at the wavelength of 1500 nm. Several papers [31] [32] have already discussed the reason behind this phenomenon. It is basically associated with H in SiO_2 and Si_3N_4 layers, because hydrogen is one of the major elements in both the PECVD process and the LPCVD process.

To solve this problem of absorption at 1500 nm, we tried a thermal annealing process at the temperature of 1200 C. The spectrum of the 47-notch grating sample was measured before and after 0.5 hour, 1.5 hours, and 3.5 hours of annealing process, and the experimental results are compared in Fig. 5.2. It is clear that a 1.5 hour annealing process at 1200 C is able to remove the absorption completely.

There is also another absorption dip at around the wavelength of $1.4\mu m$, also caused by H in SiO_2 and Si_3N_4 layers. Although it is not discussed in this thesis right now, we are also in the process of removing that absorption dip using the annealing process. Hopefully we can provide satisfactory and reliable results in the near future.

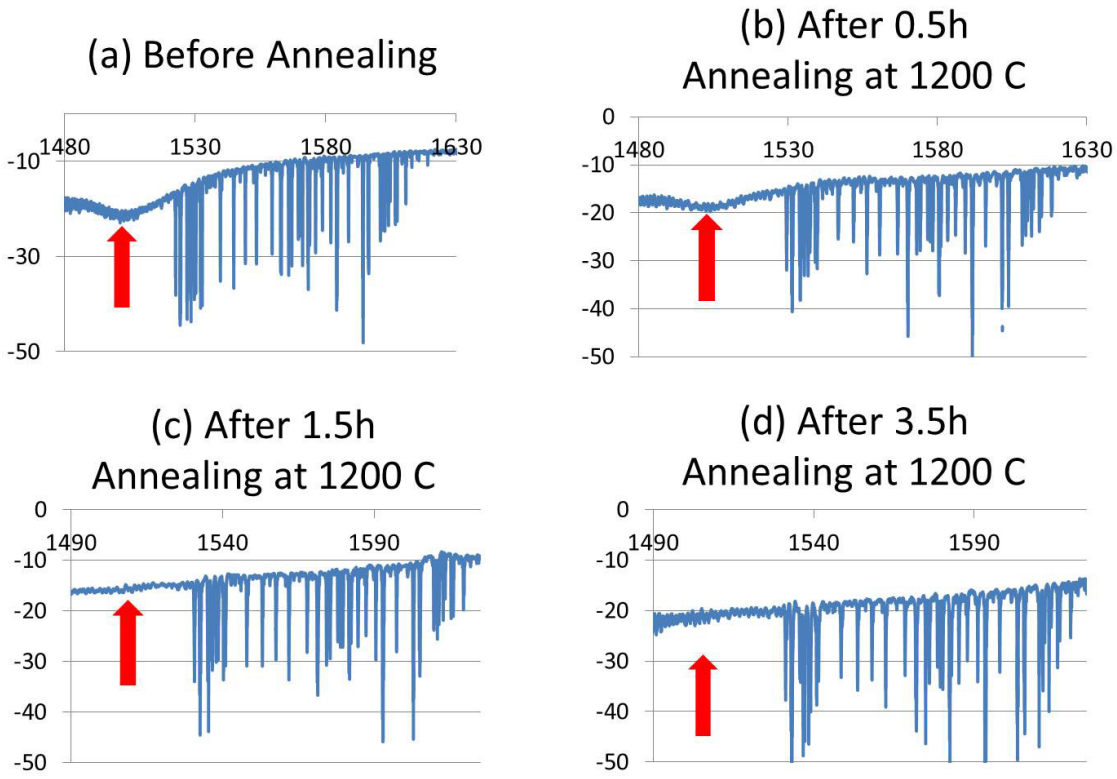

Figure 5.2: Thermal annealing at 1200 C has been used to remove the absorption dip at 1500 nm. (a) Before annealing, the absorption dip was very clear. (b) After 0.5 h annealing at 1200 C, the absorption dip was less obvious. (c) After 1.5 h annealing at 1200 C, the absorption dip was gone. (d) After 3.5 h annealing at 1200 C, the spectrum was the same as 1.5 hour annealing.

5.3 Some Further Improvement & Future Work

Although the current experimental results are really promising, there are still many improvements which can be investigated more or done in the future.

1. Although a CWBG with 20 dips has been demonstrated, the depths or the suppression ratios of these dips are not exactly the same. Some are deeper at around 25 dB, but some are shallower at around 15-17 dB. In the original design, they are all supposed to have the same suppression ratio. Therefore, more effort (such as patterning using a better 100 kV EBL system) is needed to make sure that all spectral notches have the same depths and bandwidths as in the design.

2. As can be seen from all the previous figures of CWBG, the side band is not super smooth. In theory it should be a very plain and smooth spectrum without any side-lobes, but in practise there is still some very narrow side-lobes which are around 1 dB deep. There could be caused by insufficient resolution of our current e-beam lithography system in writing very small waveguide width steps (4 nm for the most recent CWBG design). In order to solve this, a more precise e-beam lithography with 100 kV acceleration voltage may be required.

   To explain it in more details, presently I am using a 30 kV e-beam lithography machine from Raith to write the CWBG, whose best feature size is just about 20-30 nm, assuming the focus, stigma, aperature, etc are all perfectly adjusted.

Ideally, the minimum feature size should be 5 nm or even less. Thus I am actually challenging the capability of Raith machine, and every lithography is 'try my best'. The good news is that UMD just acquired a new 100 kV EBL system, so we should definitely try writing the same CWBG patterns using the new EBL system with higher resolution.

3. The propagation loss of the CWBG is around 2 - 3 dB/cm, which is a problem for the application of astrophysics. The overall loss should be minimized as small as possible. Every photon counts importantly in the field of astrophysics. Some of the loss may be from the Si-N bond and N-H bond [32] and [31]. In order to decrease the overall propagation loss or radiation loss of the CWBG, a good way to start here is to perform some thermal annealing process for the fabricated waveguide coupler, for a few hours.

4. For future applications, the CWBG may need to be connected with photonic lanterns, which has 20 or even more output single-mode fibers. The coupling can be a problem. Therefore, it may be useful for us to try fabricating waveguide lantern, which can be fabricated on the same chip with our CWBG and AWG. Thus everything is integrated on one single chip, eliminating the problem of coupling and connection. Similar waveguide lanterns have been realized in [33] and [34].

Chapter 6: Conclusions

In the first part of the proposal, the world's first CWBG is demonstrated both theoretically and experimentally. The CWBG is able to get rid of multiple randomly-distributed wavelengths in the spectrum. It is fabricated using silica-on-silicon technology with the help of e-beam lithography. The whole process is designed to be very straightforward and easy to follow, but it produces one of the most powerful integrated optical filters.

To realize such a CWBG, a LP/LA algorithm is used at first for calculating the grating profile, or the effective index variation along the grating. Then the effective index is converted into a detailed shape/structure of a waveguide grating. The thickness of the waveguide grating is a constant, but the width varies in an aperiodic way. With the help of Matlab script control, about 200'000 small segments are assembled together to form the final shape of CWBG, whose overall length is about 2 cm. After this, a 3D simulation is performed using FIMMWAVE / FIMMPROP, to check if the reconstructed spectrum agrees with the target spectrum or not. If everything is fine, the profile of CWBG is exported from FIMMWAVE / FIMMPROP to a GDSII file for e-beam lithography directly. High coupling fiber-to-waveguide couplers are also added to both sides of the CWBG. Finally, the spectrum of the

CWBG is measured with a broadband lightsource, a fiber rotator and an Optical Spectral Analyzer (OSA). Fully tunablility of the CWBG is also demonstrated, so the spectral locations of the real dips can appear precisely at their desired positions in the spectrum.

The future improvements will involve realization of 50 and 100 random spectral notches, better accuracy ($\pm$ 0.1 nm) of the spectral position for each notch, and further reduction of the propagation loss. Integration of CWBG with AWG and integrated waveguide lanterns will also be realized.

Part II

Fiber-to-Waveguide Coupler With Ultra High Coupling Efficiency

Chapter 7: Introduction

Si_3N_4/SiO_2 waveguides on silicon find applications in communication, signal processing, optical sensors, narrow-band filters, photonic band gap engineering, on-chip optical frequency comb generation, short pulse generation and photonic integrated circuits for optical interconnects [35] [36] [37] [38] [39] [40] [41]. Compared with Silicon-on-Insulator (SOI) technology which absorbs light below the wavelength of 1.1 μm, Si_3N_4/SiO_2 waveguide has the advantage of a larger transparent spectrum and ultra-low propagation loss [42] [43]. The index contrast between Si_3N_4 and SiO_2, although not as high as that in the SOI waveguides, is still large enough to realize reasonably confined waveguides for integration. As for any integration platform, one of the key issues is how to couple light efficiently from an optical fiber into a planar waveguide.

Generally speaking, there are three major approaches for achieving a high coupling efficiency between an optical fiber and a Si_3N_4/SiO_2 waveguide. The first approach utilizes the grating coupler (GC), where the light is launched from an optical fiber into a GC at an oblique angle [44]. A large number of studies have been focused on improving the coupling efficiencies by using a GC [45] [46] [47]. One drawback of the GCs is that these devices are not usually broadband, because the

phase matching condition can only be met near the central wavelength. Moreover, since a GC typically couples the light from a single-mode optical fiber to a multi-mode waveguide, a subsequent mode-converter is necessary for bringing the light back to a single-mode confined waveguide. It is worth noting that the state-of-the-art GC has recently demonstrated a coupling loss of 0.62 dB with a grating width of 15 μm. This grating width needs to be tapered down with an appropriate taper and this leads to extra loss [48].

The second popular approach to achieving a high coupling efficiency between an optical fiber and a Si_3N_4/SiO_2 waveguide is to use a taper at both ends of the waveguide [49]. The taper-based couplers are inherently more broadband than the GC-based couplers, but in most cases,it requires a precise end-facet cleaving process to achieve a high coupling efficiency. Finally, the third approach of coupling relies on the concept of evanescent-field coupling, where efficient coupling is realized between an overlap region between a single-sided conical tapered fiber and a tapered Si_3N_4/SiO_2 waveguide [50]. Although the results are promising, it is hard to apply this technique for coupling to multiple devices or for large scale integration applications.

In this part of the thesis, we demonstrate a fiber-to-waveguide coupler implemented on the Si_3N_4/SiO_2 waveguides on silicon substrate using Si_3N_4 as the core material and SiO_2 as the cladding material. This coupler features ultra high coupling efficiency (98 % in theory and 96 % in experiment) for a ultra-broadband transmission spectrum, ease of cleaving and large alignment tolerances. The approach introduced here is also applicable for multi-device operations. In Chapter 8,

we first present a theoretical analysis of the coupling efficiencies for different waveguide parameters (i.e. thickness of layers, waveguide width, etc). Then, in Chapter 9 the couplers are fabricated and the coupling efficiencies and the alignment tolerances are characterized experimentally. In Chapter 10, we discuss further improvements and potential applications suitable for the waveguide coupler. Finally, in Chapter 11, we conclude and briefly discuss future work.

Chapter 8: Design & Simulation

8.1 Waveguide Coupler Design

Fig. 8.1 shows our proposed geometry of the waveguide coupler. The waveguide coupler, which has Si_3N_4 as the core layer and SiO_2 as both the top and bottom cladding layers, is implemented on the Si_3N_4/SiO_2 waveguides on silicon substrate to obtain a larger spectral transparency window. Compared with the SOI platform which absorbs light below 1.1 μm, a Si_3N_4/SiO_2 waveguide is transparent for both the visible and the near-infrared spectra. Having such a large spectral operation range is of particular interest in many areas, such as sensors and astronomy applications [9] [8].

As shown in Fig. 8.1, the whole waveguide coupler is composed of three parts. Part I is a loosely-confined straight waveguide whose mode profile is optimized for the maximum coupling with the fiber. As will be shown later, the geometry of the Part I waveguide is investigated such that it could realize a ultra-broadband coupling efficiency over a wide spectrum. There is also another benefit of putting the Part I straight waveguides on both ends of the coupler. The advantage is the ease of end-facet cleaving process, which tends to be tedious and tricky. Because of the Part I straight waveguides, the cleaving position is not that important for

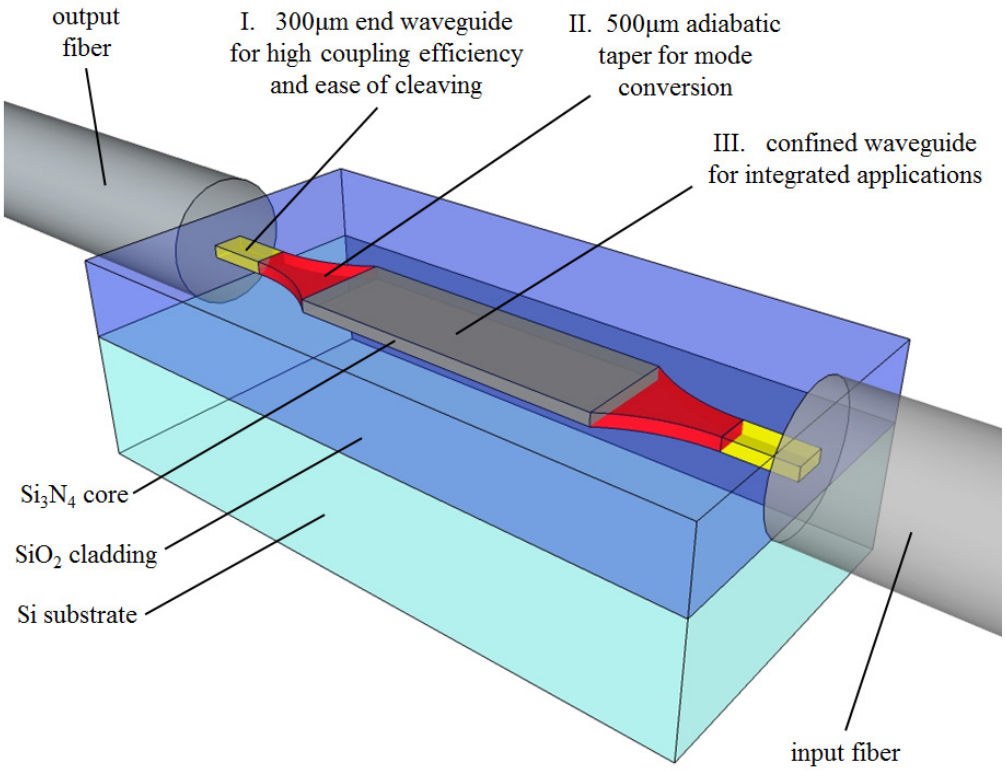

Figure 8.1: Diagram of the Si_3N_4/SiO_2 waveguide coupler which is composed of three parts. Part I is a straight waveguide with a loosely-confined mode for ultra-broadband high coupling efficiency and insensitivity to cleaving position. Part II is an adiabatic mode-converter which converts the loosely-confined mode to a more-confined mode. Part III is the central areas where the mode is more confined. Depending on future applications, specific structures can be written on Part III. As a proof of demonstration for the coupling efficiency, in this paper Part III is written as a straight waveguide with a more confined mode.

realizing the high coupling efficiency. The coupling efficiency will be decent as long as the cleaving takes place within the Part I straight waveguide.

Following Part I of the waveguide, Part II is an adiabatic waveguide mode-converter which transforms the loosely-confined mode in Part I to the more-confined mode in Part III. The length of Part II is selected to be about 500 - 1000 μm so the mode conversion happens gradually without noticeable radiation loss. Besides, the length of both Part I and Part II are chosen not to be very long, so the propagation loss of Part I and Part II is still small. Considering a length of 300 μm for Part I and a length of 500 μm for Part II, and a typical propagation loss of < 2 dB/cm, the overall propagation loss of Part I plus Part II will be < 0.16 dB, which is tolerable for most applications. Finally, Part III of the waveguide coupler is the region where the optical mode is more confined. Various structures, such as waveguide Bragg gratings (WBG), ring resonators, arrayed waveguide gratings (AWG), etc, can be fabricated in this region to fulfil many different purposes.

Before moving on to the simulations, please let me compare and analyze the three coupling techniques (butt-coupling, coupling from GC, and evanescent-field coupling) here briefly again. The waveguide coupler analyzed in this thesis is designed to be butt-coupled with the optical fiber. Compared with other coupling techniques such as GC or evanescent-field coupling, it is easy to align the fiber to achieve a high butt-coupling efficiency. In addition, using butt-coupling technique, it is also possible to couple to several devices simultaneously. Unlike evanescent-field coupling [50], butt-coupling has the benefit of larger fiber-to-waveguide alignment tolerances. And compared to GC, the butt-coupling approach has a better wave-

length insensitivity. We note that the alignment tolerances of butt-coupling can be comparable to that of GC. For most butt-coupled waveguide couplers with nano-sized tapers at the end, the cleaving has to occur exactly in the end of the taper, with a precision of $\pm$ 10 μm. As a comparison, in our design the Part I waveguide has a relatively long length (500 μm) during the fabrication, so the silicon chip can be cleaved anywhere in Part I of waveguide, within say $\pm$ 200 μm.

8.2 Simulation

For both the design and the simulation, an optical simulation software FIMMWAVE/-FIMMPROP from Photon Design Ltd, is used for obtaining the mode profiles and the coupling efficiencies [51]. The coupling efficiency is calculated by performing the integrals of the field overlap between the fiber mode and the waveguide mode. FIMMPROP also allows the export of a GDSII pattern of the whole waveguide coupler for the subsequent nano-fabrication. In order to get a high coupling efficiency, a high numerical aperture (NA) UHNA3 fiber with a small mode size of 4.1 μm at the wavelength of 1550 nm is used for the butt-coupling with the waveguide coupler. The use of a high NA UHNA3 fiber is not a problem since a low splicing loss of $\sim$ 0.1 dB with a typical single-mode fiber (i.e. SMF28) can be realized easily [52] [53]. So although in this paper the waveguide coupler is designed to be coupled with the UHNA3 fiber, the same type of coupler will also be compatible with a SMF28 fiber provided it is fusion spliced properly with an UHNA3 fiber.

A thorough and precise simulation is required when optimizing the dimensions of the Si_3N_4 waveguide coupler. In the first step, we try to make the whole coupler design as simple as possible, so a standard single mode fiber (SMF28) and a 1-layer Si_3N_4 waveguide with a rectangular cross-section are chosen in the simulation. Here, the wavelength used is 1550 nm, and the fiber is butt-coupled to the cleaved end of the Si_3N_4 waveguide coupler. In the first step, a commercial optical design software (FIMMWAVE / FIMMPROP) is used for the modeling [51]. A complex Finite Difference Method (FDM) mode solver is used for finding the modes in the Si_3N_4

waveguide, and a complete field overlap integral method is used for obtaining the coupling efficiency at the interface between the fiber and the waveguide. Finally, to guarantee the reliability of the calculated coupling efficiency, the size of the computation grid, which determines how precisely the waveguide cross-setion is sampled in the simulation, is selected carefully. As is well known, the simulation will be imprecise when the size of the computation grid is too large, and will be very time-consuming when the computation grid is too small. The size of the computation grid is chosen in such a way that even if we decrease it further more, the coupling efficiency still remains the same. In this case, the results of the whole simulation have converged and are therefore reliable.

8.2.1 Some Tricks and Discussions about FimmWave/FimmProp

Before moving on to the simulation results, there are two small but very important "rules" that should always be observed in the simulation. These are such seemingly minor things that sometimes people just forgot to check them.

8.2.1.1 Guarantee Sufficient Simulation Region

The first "rule" is: always make sure that the mode field intensity approaches zero at the boundary of the simulation region. If the mode field does not go to zero at the boundary, then it indicates the simulation region is just not big enough and we are losing some of the mode information. In this case, any results obtained from an insufficient simulation region will be unreliable.

Suppose we know the current simulation region is too small to wholly cover the mode field, we just need to increase the region (that means to increase the SiO_2 cladding region in the following example). More importantly, it also tells us what should we actually fabricate in the real experiment. Fig. 8.2 and Fig. 8.3 shows a very good example of judging the appropriate simulation region.

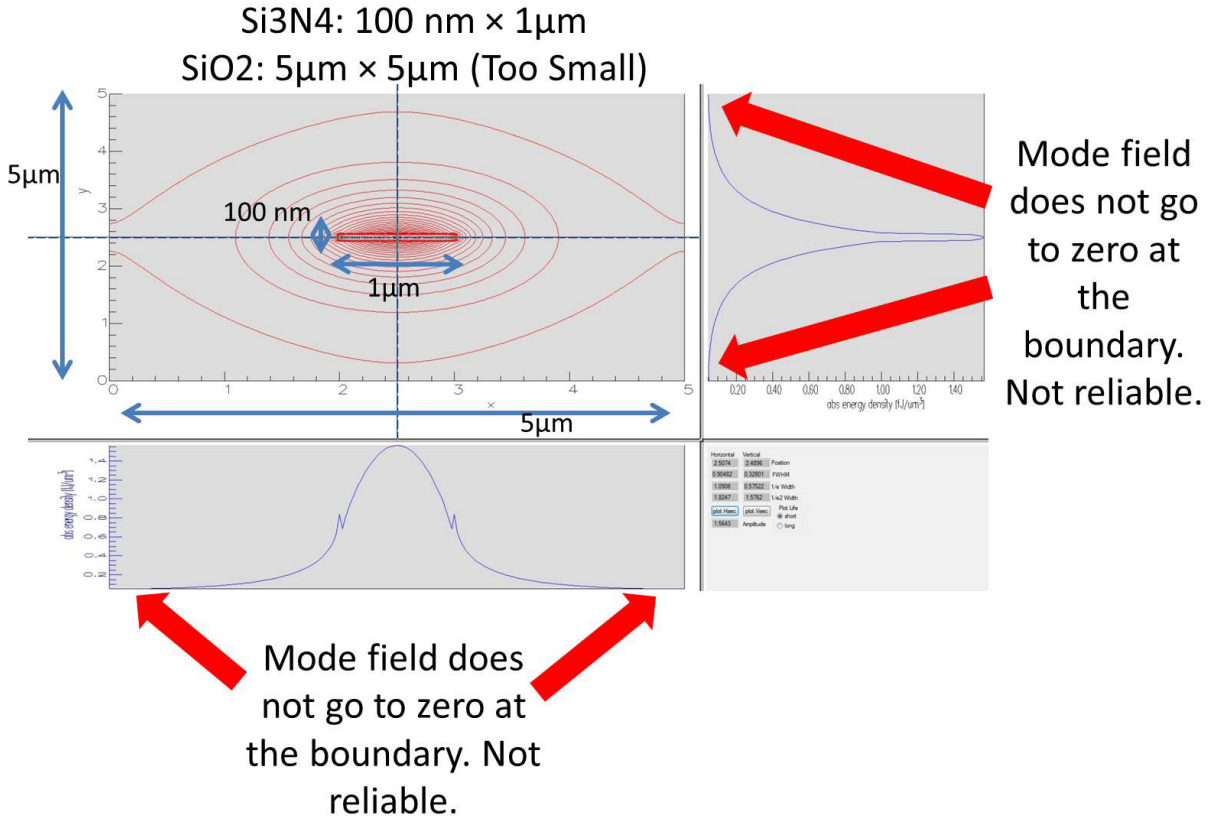

Figure 8.2: Simulation of a $100nm$ thick, $1\mu m$ wide Si_3N_4 waveguide. The SiO_2 cladding region surrounding the Si_3N_4 core is set to be $5\mu m$ by $5\mu m$ here. The field intensities do not approach zero at the boundary, so the results are not reliable. We need to consider a larger SiO_2 cladding region in both our theory and experiment.

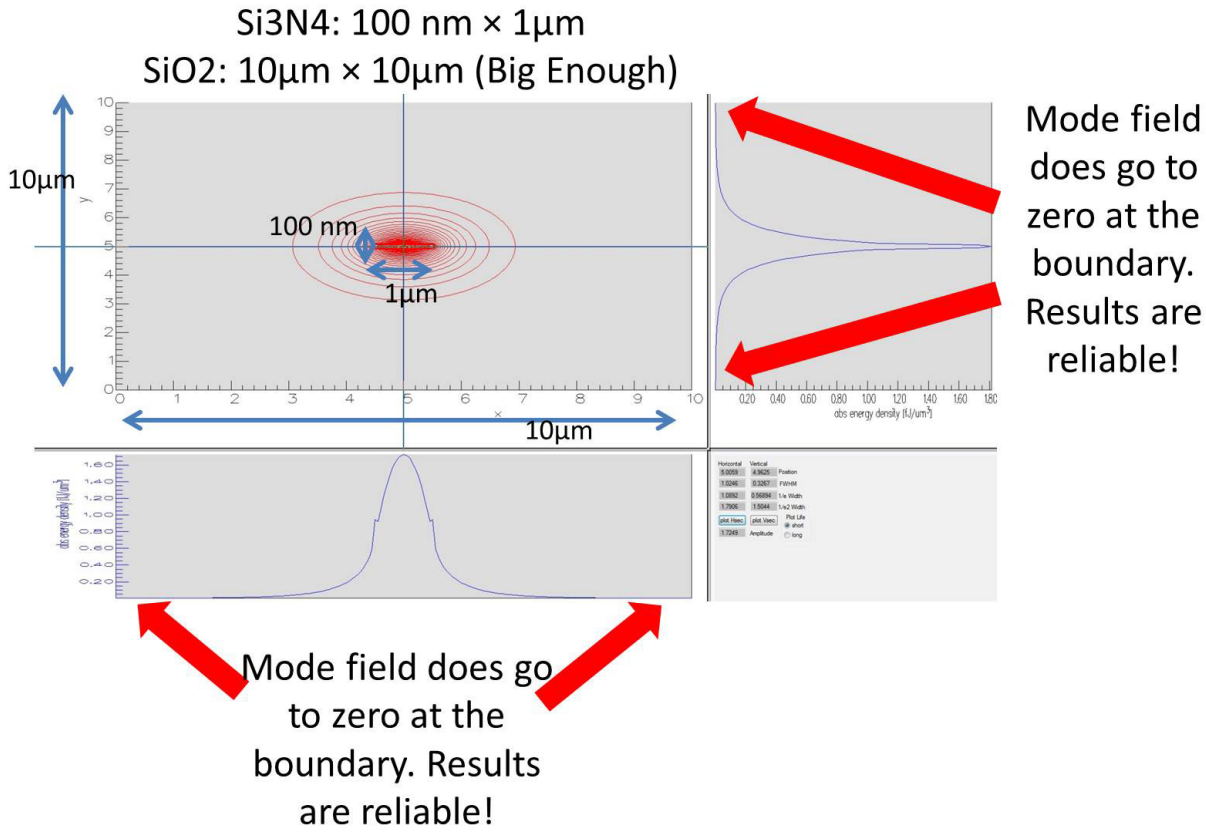

Figure 8.3: Simulation of a $100nm$ thick, $1\mu m$ wide Si_3N_4 waveguide. The SiO_2 cladding region surrounding the Si_3N_4 core is set to be $10\mu m$ by $10\mu m$ here. The field intensities approach zero at the boundary, so the results are reliable. This indicates that a $10\mu m$ SiO_2 cladding region is sufficient in both our theory and experiment.

8.2.1.2 Guarantee Sufficient Simulation Grids n_x and n_y

This trick applies to the Finite Difference Method, where the whole simulation region was divided into a large number of grids vertically and horizontally. At this moment, let us use n_x and n_y to represent the number of grids in the x and y directions.

The choice of n_x and n_y is quite important. If they are too small, then the simulation results will not be reliable enough. For example, let us assume a simple simulation for a $100nm$ thick, $1\mu m$ wide Si_3N_4 waveguide, which is covered by $10\mu m$ by $10\mu m$ SiO_2 cladding. If $n_x = 100$ and $n_y = 100$, then the simulated parameters (e.g. the effective index, FWHM) are just not precise enough. A good judgement here is to just take a look at the 3D view of the field intensity. As shown in Fig. 8.4, the simulated field is not smooth at all.

As a comparison, in Fig. 8.5, if we set $n_x = 500$ and $n_y = 500$, the field becomes quite smooth. The effective index calculated using $n_x = 500$ and $n_y = 500$ should be more accurate than the effective index calculated using $n_x = 100$ and $n_y = 100$. For accuracy, it is recommended that n_x and n_y shouldn't be too small.

It is also worth noting that if n_x and n_y are too large, then the simulation will take a long time to run. In practise, n_x and n_y could be adjusted to be between 200 and 500, depending on the requirements between speed and precision.

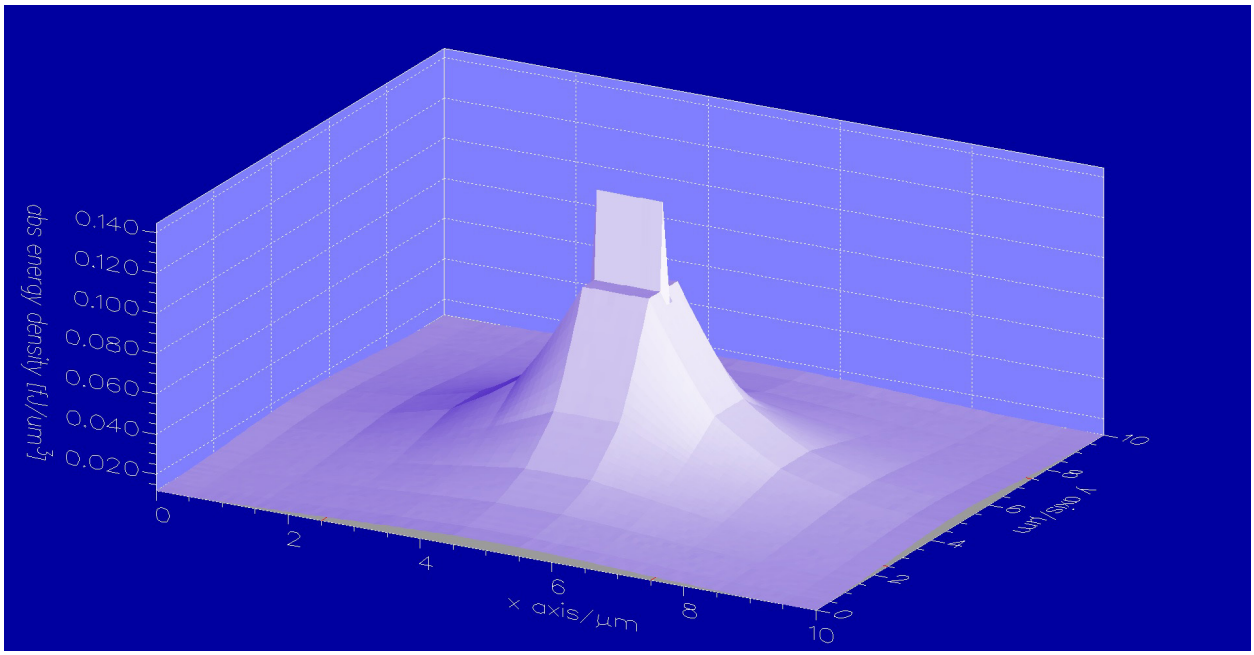

Figure 8.4: Simulation of a $100nm$ thick, $1\mu m$ wide Si_3N_4 waveguide surrounded by $10\mu m$ by $10\mu m$ SiO_2 cladding. If $n_x = 100$ and $n_y = 100$, the field profile is not smooth, and the simulated data may not be accurate.

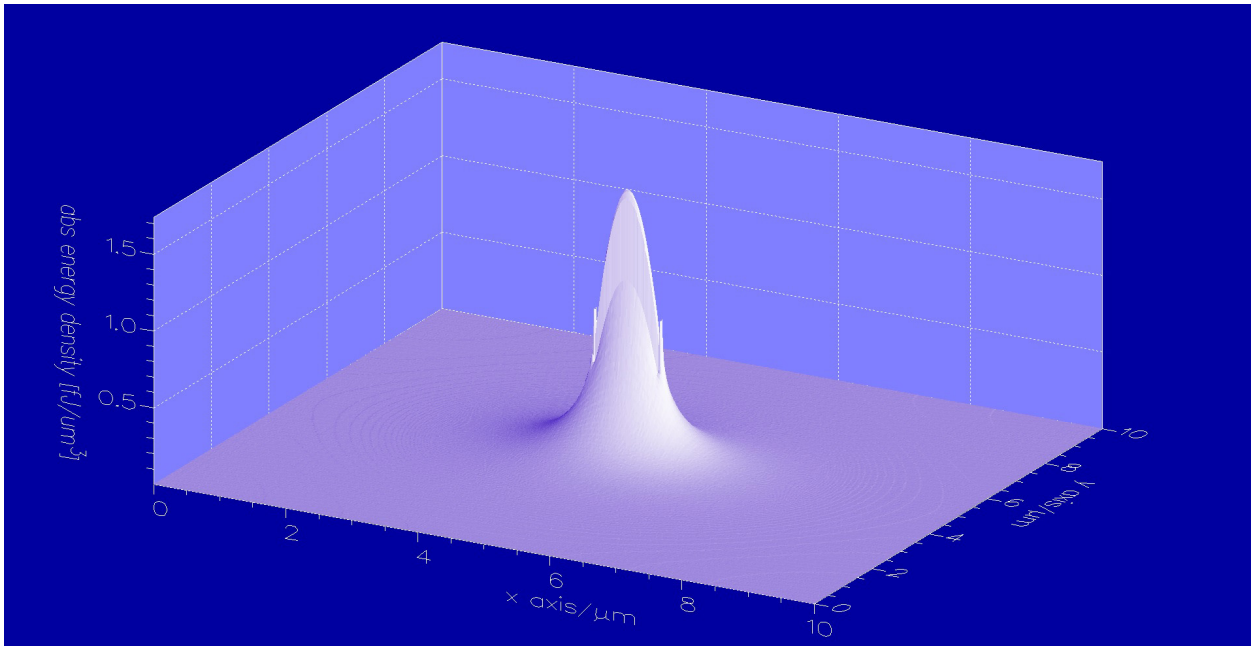

Figure 8.5: Simulation of a $100nm$ thick, $1\mu m$ wide Si_3N_4 waveguide surrounded by $10\mu m$ by $10\mu m$ SiO_2 cladding. If $n_x = 500$ and $n_y = 500$, the field profile is smooth enough, and the simulation can be trusted. However, n_x and n_y shouldn't be too larger, for the run-time of the simulation will be too long.

8.2.2 Simulation Results

8.2.2.1 Simulation Results: Coupling Efficiency with SMF28 Fibers

In order to optimize the coupling efficiency, the thickness and the width of the Si_3N_4 waveguide are varied, and the corresponding coupling efficiency to SMF28 is plotted, as shown in Fig. 8.6. In the simulation, the index of the core and cladding of SMF28 is 1.4682 and 1.4615, giving a numerical aperture (NA) of 0.14, and the MFD of SMF28 is set to be 10.4 μm at 1.55 μm. An interesting observation is made here. The maximum coupling efficiency between a SMF28 and a Si_3N_4 waveguide is almost constant ($\sim$84%, or -0.8 dB), independent of the thickness of the Si_3N_4 waveguide from 50 to 100, 200 or 300 nm. However, when the thickness of the Si_3N_4 waveguide is smaller, the maximum coupling occurs at a larger waveguide width. For a 50 nm thick Si_3N_4 waveguide, the best coupling happens at a width of about 1.2 μm. On the other hand, for a 300 nm thick Si_3N_4 waveguide, the optimum coupling efficiency occurs at a width of about 200 nm. Based on these plots, we find that a reasonable thickness of the Si_3N_4 waveguide is 100 nm (not too thin in order to minimize possible unevenness in the layer thickness), and decent coupling can be achieved if the width of the waveguide is between 500 nm and 600 nm. The MFD of the mode is 3.96 μm in the x direction and 3.52 μm in the y direction, for a 100 nm $\times$ 500 nm Si_3N_4 waveguide. This mode profile allows a good coupling efficiency, but it is not a well-confined waveguide mode. As a contrast, a reasonably confined waveguide mode occurs when the geometry of the Si_3N_4 waveguide is 100 nm $\times$

1.25 μm, with a MFD of 1.75 μm in the x direction and 1.37 μm in the y direction. Therefore, for future integration purpose, a simple tapered mode converter can be added to convert a 100 nm $\times$ 500 nm Si_3N_4 waveguide to a 100 nm $\times$ 1.25 μm Si_3N_4 waveguide, therefore producing a more confined mode. This type of taper is easy to pattern, since the minimum scale is 500 nm.

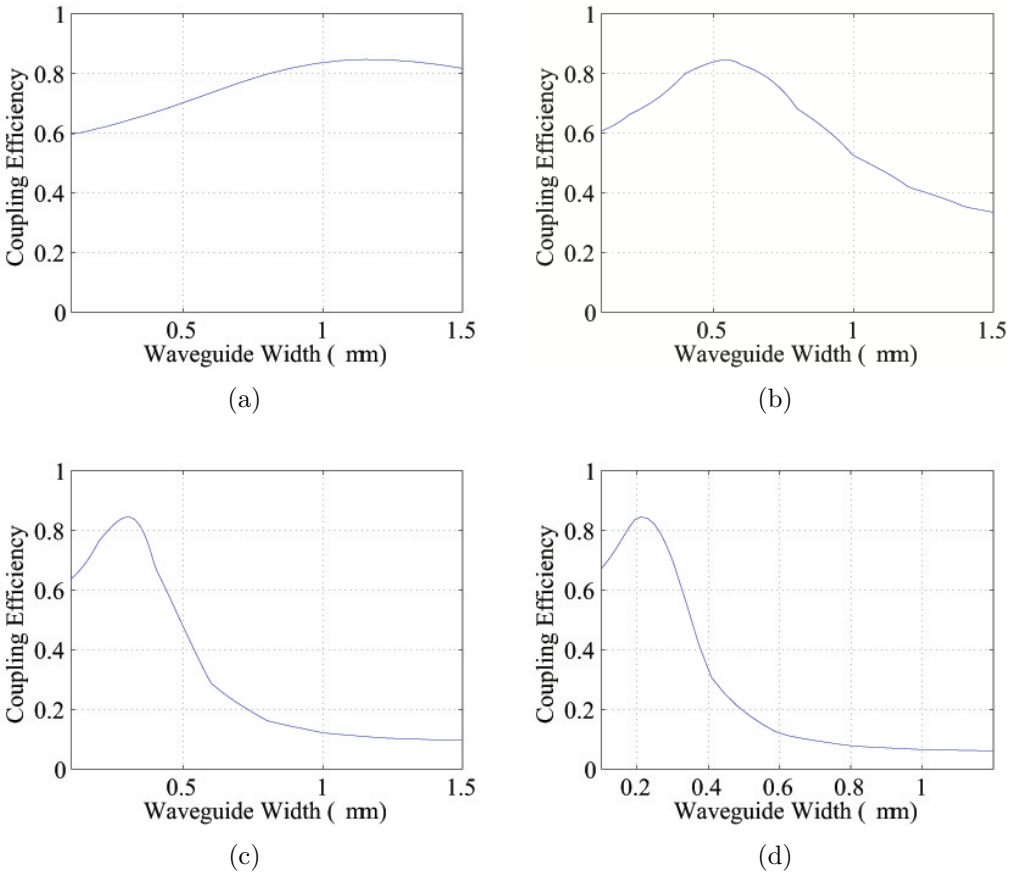

Figure 8.6: Theoretically expected coupling efficiency between SMF28 and Si_3N_4 waveguide (a) Si_3N_4 thickness is 50nm. (b) Si_3N_4 thickness is 100nm. (c) Si_3N_4 thickness is 200nm. (d) Si_3N_4 thickness is 300nm.

8.2.2.2 Simulation Results: Coupling Efficiency with SM1500G80 Fibers

To further investigate the coupling capability of the Si_3N_4 waveguide couplers, we try to change the type of fiber from SMF28 to Thorlabs SM1500G80, which has a smaller MFD of 6.4 μm. The index of the fiber core and cladding is 1.45636 and 1.44399 respectively, giving a NA of 0.19. Fig. 8.7 shows the coupling efficiency between the SM1500G80 fiber and the Si_3N_4 waveguide of different dimensions. The maximum efficiency in this case is $\sim$ 94 %, or -0.27 dB. This is by far the best coupling efficiency proposed using Si_3N_4-core waveguide in the silica-on-silicon planar waveguide technology. At the maximum coupling, a MFD of 2.31 μm in the x-direction and a MFD of 2.11 μm in the y-direction are extracted, for a 100 nm $\times$ 700 nm Si_3N_4 waveguide. To show it more clearly, the mode profiles of both 100 nm $\times$ 700 nm Si_3N_4 waveguide and SM1500G80 fiber are shown in Fig. 8.8. Similarly, for future integration applications, the addition of a tapered mode converter which changes the waveguide dimension from 100 nm $\times$ 700 nm to 100 nm $\times$ 1.25 μm will be sufficient. In this case, both high coupling efficiency and better mode confinement can be realized on a small chip. Moreover, another insightful observation is made. From Fig. 1 and Fig. 2, when the thickness of the Si_3N_4 waveguide is the same, the maximum coupling with SM1500G80 occurs at a larger waveguide width than with SMF28. For instance, for a 50 nm thick Si_3N_4 waveguide, the best coupling happens at a waveguide width of $\sim$ 1.2 μm for SMF28 fiber, but at $\sim$ 1.75 μm for SM1500G80 fiber. This observation can be easily understood by

realizing that the best coupling is reached when the MFD of the fiber is most similar to the MFD of the waveguide. Since the MFD of SM1500G80 is smaller than that of SMF28, SM1500G80 will require a smaller waveguide mode than SMF28 for the ideal coupling. A smaller waveguide mode represents a more confined mode, which means for a certain Si_3N_4 waveguide thickness, the width of the waveguide needs to be larger in order to trap more light inside the waveguide core region. Therefore, this leads to a larger Si_3N_4 waveguide width for maximum coupling in the case of SM1500G80 as compared to SMF28. Finally, it is worth noting that such Si_3N_4 waveguide couplers are very broadband for maintaining high coupling efficiencies. For example, for the coupling between SM1500G80 fibers and 100 nm $\times$ 700 nm Si_3N_4 waveguide couplers, simulation shows that a coupling efficiency above 90 % can be obtained over a wavelength range of 200 nm.

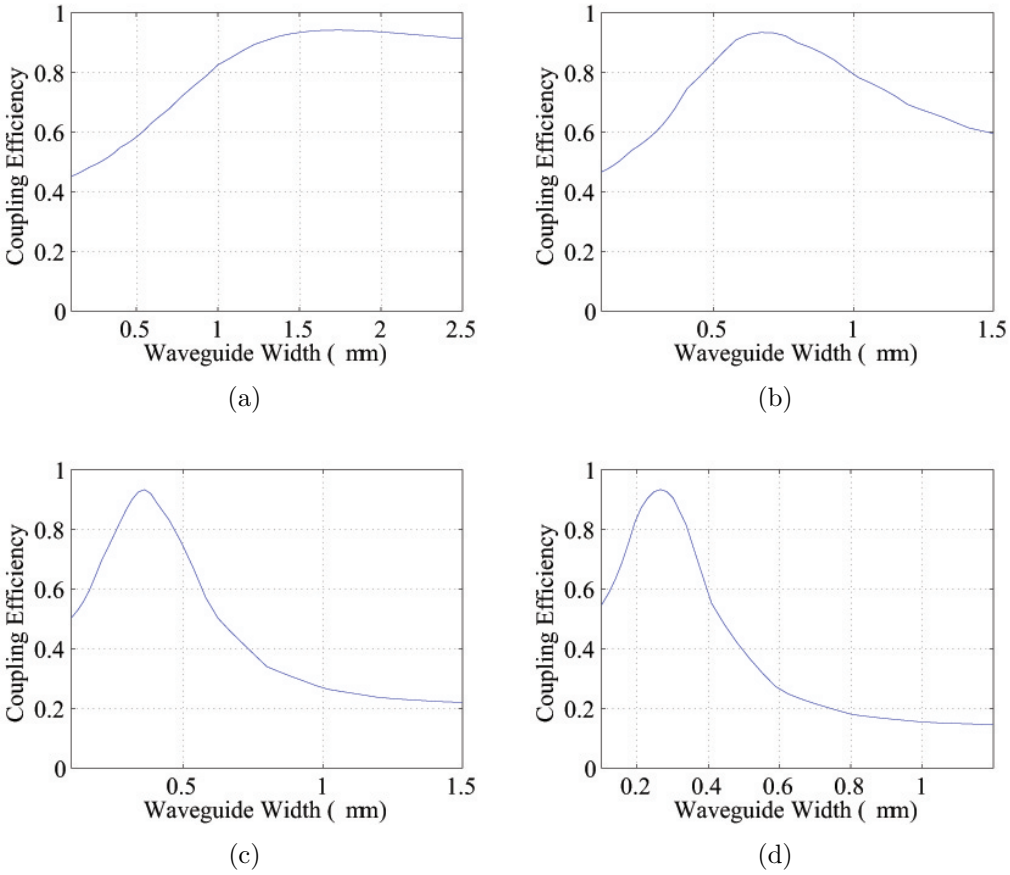

Figure 8.7: Theoretically expected coupling eficiency between SM1500G80 and Si_3N_4 waveguide (a) Si_3N_4 thickness is 50nm. (b) Si_3N_4 thickness is 100nm. (c) Si_3N_4 thickness is 200nm. (d) Si_3N_4 thickness is 300nm.

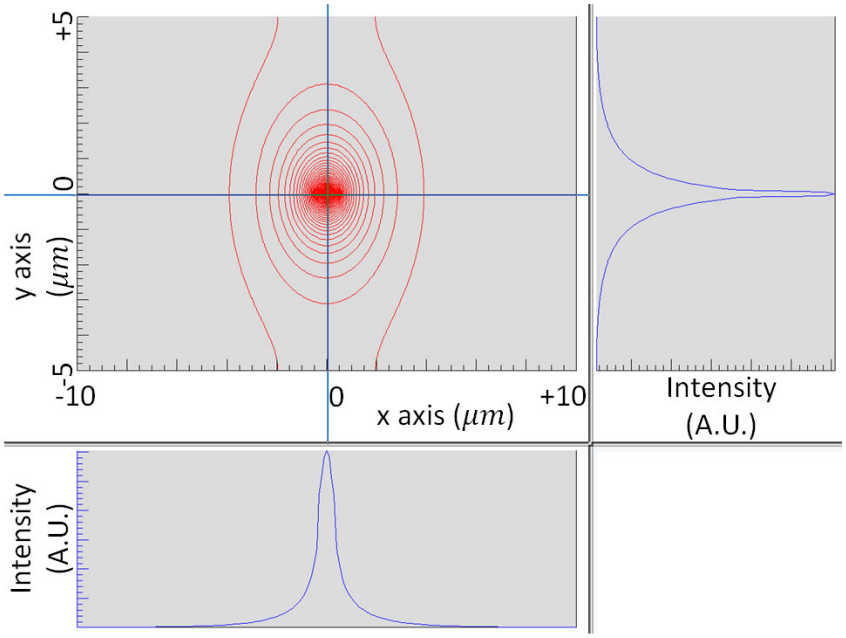

(a)

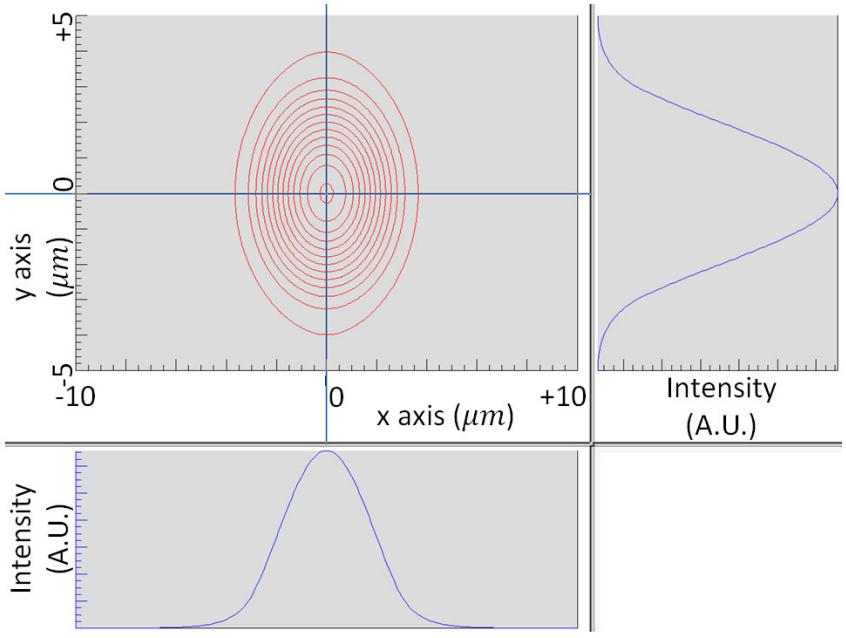

(b)

Figure 8.8: Theoretically expected mode profile of 100 nm × 700 nm Si_3N_4 waveguide and SM1500G80 fiber (a) 100 nm × 700 nm Si_3N_4 waveguide. (b) SM1500G80 fiber.

8.2.2.3 Simulation Results: Coupling Efficiency with UHNA3 Fibers

Fig. 8.9 shows the theoretical coupling efficiency between the UHNA3 fiber and the Si_3N_4/SiO_2 waveguide with different waveguide width/thickness geometries. The mode studied here is the fundamental TE mode of the Si_3N_4/SiO_2 waveguide, with a smaller mode size, a higher effective index and a lower propagation loss comparing with other leaky modes. The thicknesses of both top and bottom claddings are both 5 μm in the simulations and in the subsequent experiments. A 5 μm top and bottom cladding is thick enough to isolate the mode from being absorbed by the silicon substrate.

In this simulation, three different Si_3N_4 core thicknesses, 100 nm, 200 nm, and 300 nm, are studied, and for each thickness the coupling efficiency is plotted by varying the Si_3N_4 core width. According to the simulation result, a ultra-high theoretical coupling efficiency of 98 % is obtainable between the UHNA3 fiber and the Si_3N_4/SiO_2 waveguide for all three thicknesses of 100 nm, 200 nm and 300 nm, although the maximum coupling efficiency happens at different waveguide widths. Table 8.1 lists the maximum theoretical coupling efficiency achievable and the corresponding optimum waveguide geometries. If the Si_3N_4 core thickness is 100 nm, the width of the Si_3N_4 core needs to be about 900 nm to get 98 % coupling efficiency. If the thickness is 200 nm and 300 nm, the optimum Si_3N_4 core width becomes 450 nm and 330 nm, respectively. It is found that the maximum theoretical coupling efficiency is predicted to be a constant value as long as the fiber type and the waveguide core/cladding materials are as stated. In future work, we will present more details

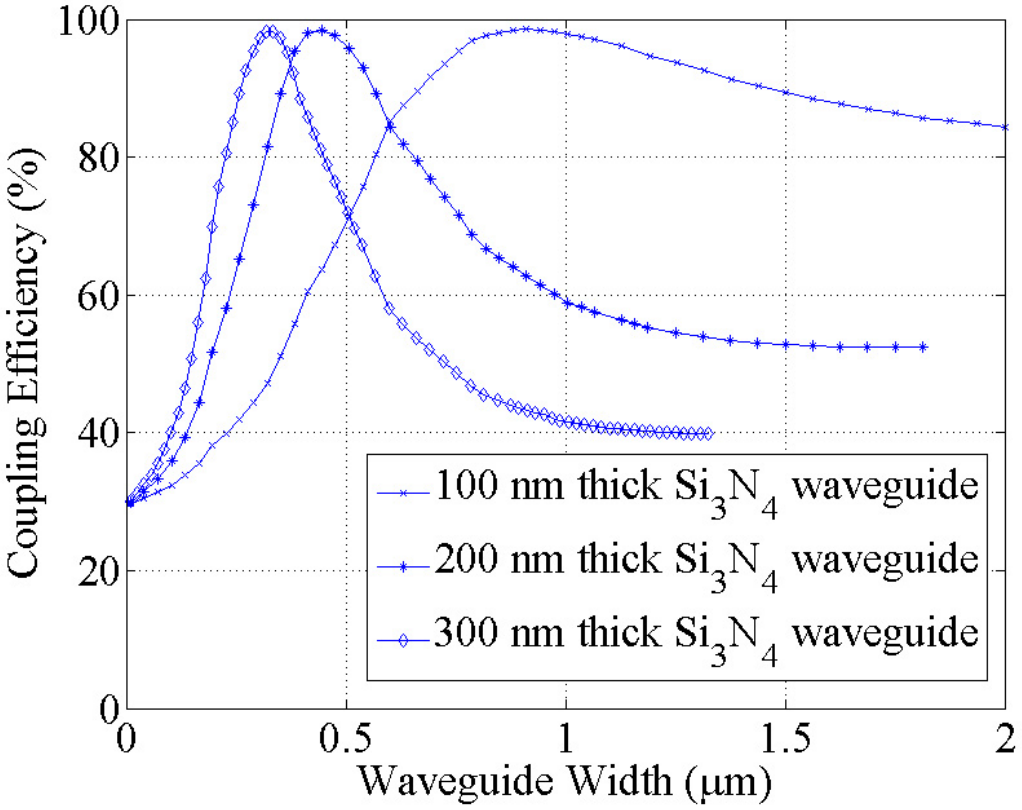

Figure 8.9: Theoretical coupling efficiency versus the tip width of the waveguide between the UHNA3 fiber and the Si_3N_4/SiO_2 waveguide for three thickness: 100 nm, 200 nm and 300 nm, at the wavelength of 1550 nm. Although the thickness and the tip width can vary, the maximum coupling efficiency is predicted to be a constant as long as the fiber type and the waveguide materials are fixed. In this case, the fiber is UHNA3 and the waveguide is Si_3N_4/SiO_2, and the maximum theoretical coupling efficiency is 98 %.

on why the maximum theoretical coupling efficiency is a constant value, and we will consider different fibers and different waveguides.

Table 8.1: Maximum theoretical coupling efficiencies at 1550 nm and the corresponding Si_3N_4 thicknesses/tip widths

Si_3N_4 Thickness	Si_3N_4 Tip Width	Maximum Theoretical Coupling Efficiency
100 nm	900 nm	98.4 %
200 nm	450 nm	98.3 %
300 nm	330 nm	98.4 %

To verify the wavelength sensitivity of the coupling efficiency, a plot of the theoretical coupling efficiency as a function of wavelength for these three optimum waveguide geometries, 100 nm × 900 nm, 200 nm × 450 nm, and 300nm × 330 nm, is given in Fig. 8.10. As shown before, these three waveguide geometries all give a 98 % theoretical coupling efficiency at the central wavelength of 1550 nm, but their wavelength sensitivities are not the same. The geometry of 100 nm × 900 nm gives the best wavelength insensitivity, and the coupling efficiency is always higher than 70 % even over a wavelength range of 1 to 2 μm. This is because the mode of 100 nm × 900 nm Si_3N_4 waveguide is more loosely confined compared to the other two geometries. This geometry has a high aspect-ratio (width / thickness) waveguide geometry with a low confinement factor. The mode field is mostly out of the core region for the 100 nm × 900 nm waveguide, and therefore the mode field diameter does not depend sensitively on wavelength. On the other hand, the wavelength sensitivities of the 200 nm × 450 nm and the 300nm × 330 nm waveguides are similar but are not as good as for the 100 nm × 900 nm waveguide. This is because the mode for the 200 nm × 450 nm and the 300nm × 330 nm geometries is more

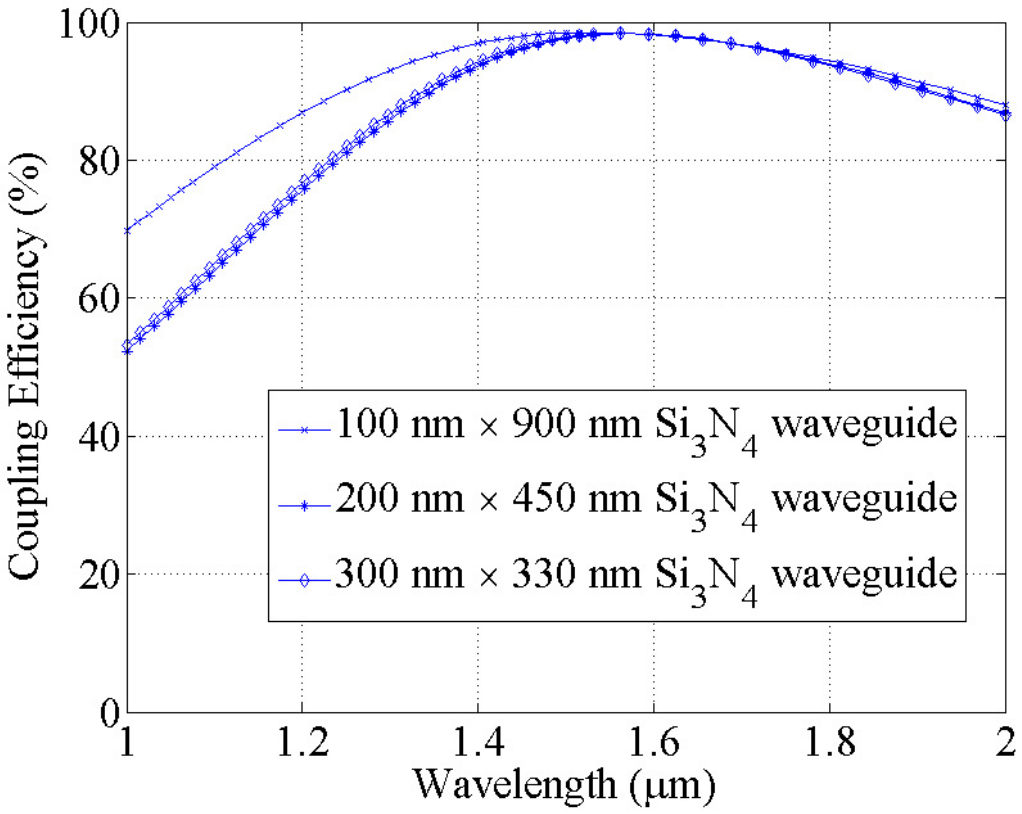

Figure 8.10: Theoretical coupling efficiency as a function of wavelength between the UHNA3 fiber and the Si_3N_4/SiO_2 waveguide of three optimum geometries in Table 8.1: 100 nm × 900 nm, 200 nm × 450 nm, and 300 nm × 330 nm. These three geometries all give a theoretical coupling efficiencies of 98 % at the wavelength of 1550 nm. The coupling efficiency is least wavelength-sensitive for 100 nm thick, 900 nm wide Si_3N_4 waveguide.

confined.

Finally, another important feature to consider is the alignment tolerances between the fiber and the waveguide. It is defined as the 3-dB width (FWHM) in a plot of the coupling efficiency versus the displacement in the x- and y- direction. This parameter indicates whether the coupling efficiency will drop substantially or not when the center of the fiber is moved horizontally or vertically with respect to the waveguide coupler. A large alignment tolerance means that even if the position of the fiber changes by a few microns, a good coupling efficiency ($<$ 3 dB change) can still be maintained. Fig. 8.11 shows the theoretical alignment tolerances between the UHNA3 fiber and the Si_3N_4/SiO_2 waveguide. It is found that the theoretical alignment tolerances are almost the same for all the three waveguide geometries, with 3.6 μm in the horizontal direction and 3.5 μm in the vertical direction.

As a proof-of-concept demonstration, we have fabricated and studied the 100 nm $\times$ 900 nm Si_3N_4 waveguide. This waveguide is expected to give a high coupling efficiency over a broad spectral range (Fig. 8.10). Moreover, according to Bowers et al. [42], a thinner Si_3N_4 with a high aspect-ratio is expected to give a smaller propagation loss.

(a)

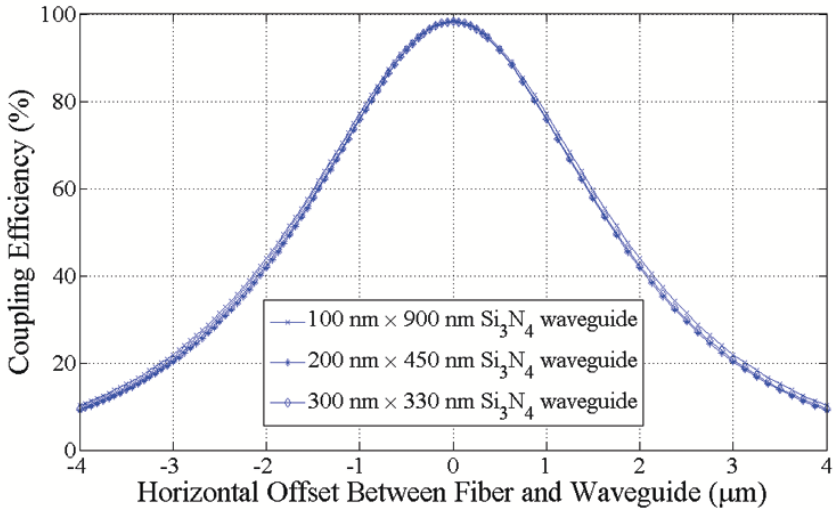

(b)

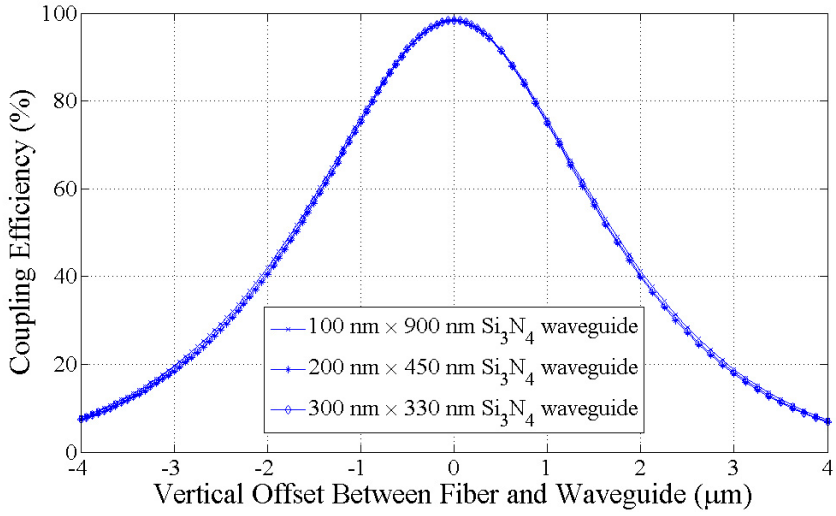

Figure 8.11: Theoretical 3-dB width (FWHM) alignment tolerances between the UHNA3 fiber and the Si_3N_4/SiO_2 waveguide of three different geometries: 100 nm × 900 nm, 200 nm × 450 nm, and 300 nm × 330 nm. It is defined as the 3-dB width in the plot of the coupling efficiency versus offset. The theoretical alignment tolerances are 3.6 μm horizontally and 3.5 μm vertically for all three waveguide geometries. (a) horizontal alignment tolerance. (b) vertical alignment tolerance.

Chapter 9: Fabrication & Experimental Results

9.1 Fabrication and Experimental Set-up

The fabrication starts with a silicon wafer with a 5 μm thermal SiO_2 layer on top. A 100 nm thick Si_3N_4 layer is then deposited using low-pressure chemical vapor deposition (LPCVD). The shape of the waveguide coupler is defined by electron-beam (e-beam) lithography. Following this, a 10 nm thick chromium hard mask is deposited by e-beam deposition followed by a lift-off process. Then reactive-ion etching (RIE) is performed and the chromium mask is removed, followed by another 5 μm SiO_2 layer deposited by plasma-enhanced chemical vapor deposition (PECVD) as the upper cladding layer. Finally, the thickness of the whole sample is polished down from the backside from 500 μm originally to about 100 μm, using a lapping jig. The waveguide coupler is then cleaved in the middle of Part I waveguide with a good cleaving position tolerance of $\pm$ 200 μm, or better. The whole fabrication process requires only one lithography step and one etching step.

It is noted that there are two extra benefits brought by this waveguide coupler design. First, since the width of the Part I high coupling efficiency waveguide is 900 nm, the pattern can be easily done by deep-UV lithography which would lead to higher yield as compared to e-beam lithography. Secondly, since the cleaving

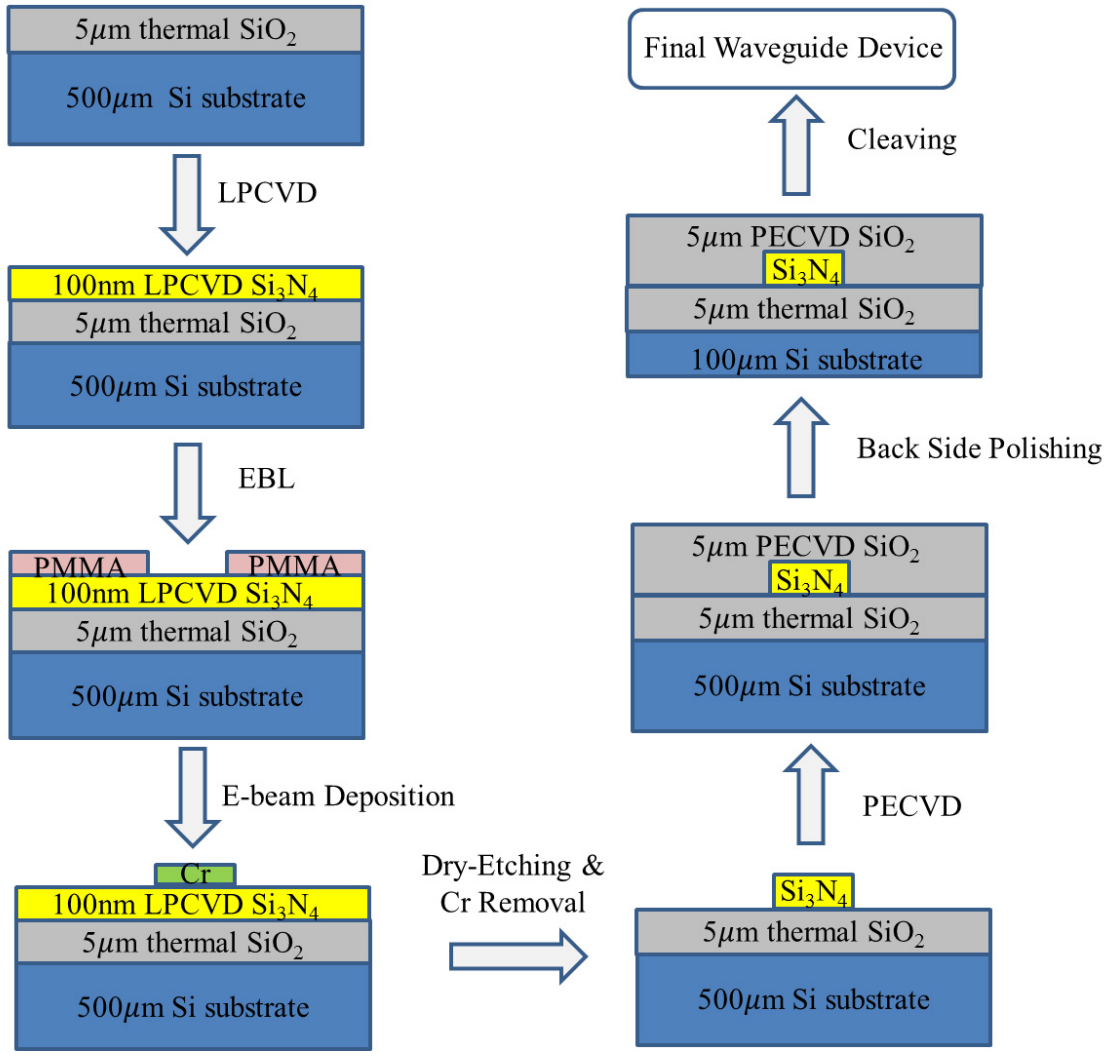

Figure 9.1: Fabrication procedures of the Si_3N_4/SiO_2 waveguide coupler with waveguide core thickness of 100 nm. The end-facet cleaving process does not need high position accuracy, thanks to the addition of the Part I waveguide on both sides of the waveguide.

Figure 9.2: Experimental set-up for the waveguide performance measurement, showing two XYZ stages which hold input and output fibers, two microscope cameras for fiber/waveguide alignment and a waveguide sample mounted in the middle.

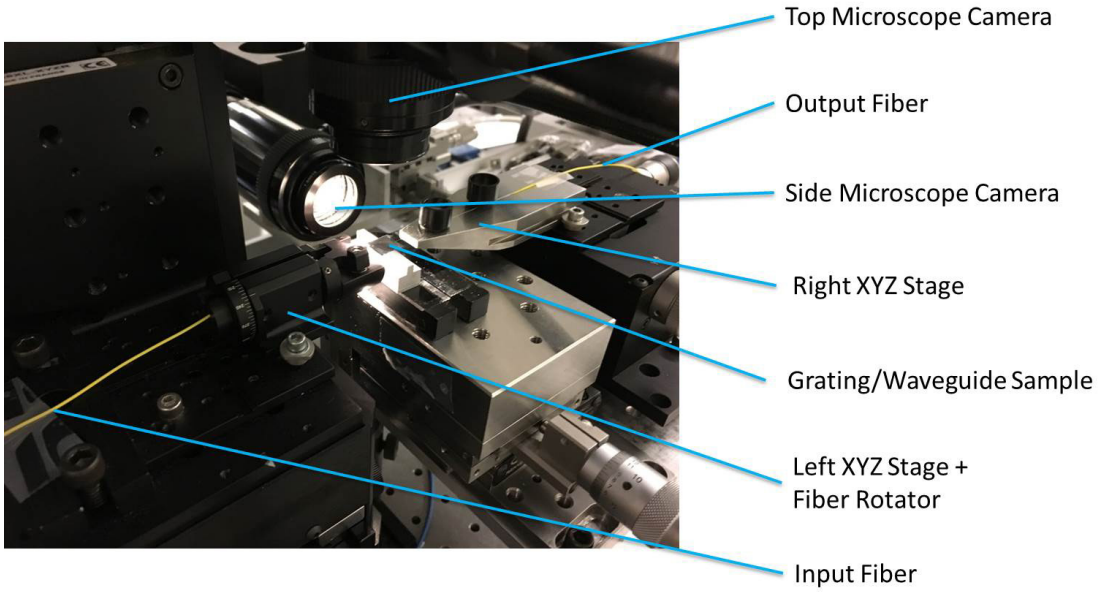

tolerance is high, the cleaving can take place almost anywhere in Part I of the waveguide. A direct cleaving process without any back-side polishing is also possible, which will save time and reduce the complexity of the fabrication process. A 500 μm thick waveguide sample is also much more robust than the 100 μm waveguide sample obtained after back-side polishing. In our experiment, we have demonstrated not only cleaving after back-side polishing of a 100 μm thick sample, but also direct cleaving of the sample with a 500 μm thickness.

Fig. 9.2 shows the experimental set-up for the waveguide performance measurement. The characterization set-up utilizes two XYZ translation stages, each holding a fiber for butt-coupling on both sides of the waveguide coupler. Two measurement methods are used. In the first method, a Superluminescent Diode (SLD) broadband light source (Thorlabs S5FC1550P-A2) is used as the light source, and a

3-paddle fiber polarization controller (PC) is used to control the polarization of the input light to the TE mode. As shown in the previous part, a theoretical coupling efficiency of 98 % is expected at the wavelength of 1550 nm. Similarly, an output fiber is butt-coupled to the other side of the waveguide coupler for maximum power output. Finally, an Optical Spectral Analyzer (OSA) is used to record the transmission spectrum of the waveguide coupler. In the second measurement method, a tunable laser and a power meter are used instead of the SLD broadband light source and the OSA. Both set-ups give the same results for the coupling efficiency.

To measure the coupling efficiency of the waveguide coupler, the throughput of two perfectly cleaved and aligned fibers (without the waveguide coupler in the middle) is measured, which represents the reference level for the fiber-to-fiber transmission. Then the Si_3N_4/SiO_2 waveguide coupler is positioned between the two fibers, and the light is coupled into and out of the Si_3N_4/SiO_2 waveguide coupler by carefully adjusting the input and output fibers for maximum transmission. The difference between the fiber-to-fiber transmission and the fiber-waveguide-fiber transmission includes the coupling losses from both facets plus the propagation loss. To find out the coupling efficiency, waveguide couplers with different lengths of 5 mm, 10 mm, and 15 mm are fabricated and cleaved. The transmission difference allows the extraction of both the propagation loss and the coupling efficiency. An index-matching gel is used to eliminate unwanted reflections and to remove any small air gaps between the cleaved fiber facet and the cleaved waveguide facet. The described insertion loss measurement approach is widely used in the field [54–56].

9.2 Experimental Results

9.2.1 Coupling Efficiency with SMF28 Fibers

The propagation loss and the coupling efficiency is obtained by plotting the transmissions of various Si_3N_4 waveguides versus their lengths (5 mm, 10 mm or 15 mm), and then by making a least-squared linear fit to the experimental points. The slope of the linear fit denotes the propagation loss, and the intercept equals 2 $\times$ the coupling loss. In order to study the coupling efficiencies between Si_3N_4 waveguides and SMF28 fibers, Si_3N_4 waveguides with a fixed thickness of 100 nm and three different widths (400 nm, 500 nm and 600 nm) are fabricated and tested, as shown in Fig. 9.3. These coupling efficiencies were measured at the wavelength of 1500 nm. These waveguide widths of 400 nm, 500 nm and 600 nm are chosen near the peak of the coupling efficiency curve in Fig. 8.6(b), which is simulated by fixing the waveguide thickness to be 100 nm and varying the waveguide width. The coupling efficiencies are extracted as -1.685 dB (68%), -0.747 dB (84%) and -0.81 dB (83%) for 100 nm $\times$ 400nm, 100 nm $\times$ 500nm and 100 nm $\times$ 600nm Si_3N_4 waveguides respectively. The comparison between the simulation and the experimental data is shown in Fig. 9.3(d), which plots the fitted average coupling efficiency versus the waveguide width, when its thickness is 100 nm. Although the coupling efficiency between the Si_3N_4 waveguide and the SMF28 fiber is good, further improvements, such as using the wafer-to-wafer bonding technique to transfer a thermally-grown SiO_2 as the top cladding layer, can be applied to substantially

minimize the propagation loss [43]. Compared with PECVD SiO_2 (which is generally deposited at 300 °C), thermal SiO_2 has better quality (less chamber contamination and higher temperature growth). Post annealing process at $\sim$ 1100 °C may also be beneficial, as it decreases the concentration of N-H bonds in the film caused during the PECVD process [57]. Finally, the average coupling efficiencies are also shown in Table 9.1, together with the 68 % confidence intervals, which show the region where the real coupling efficiencies will most likely lie.

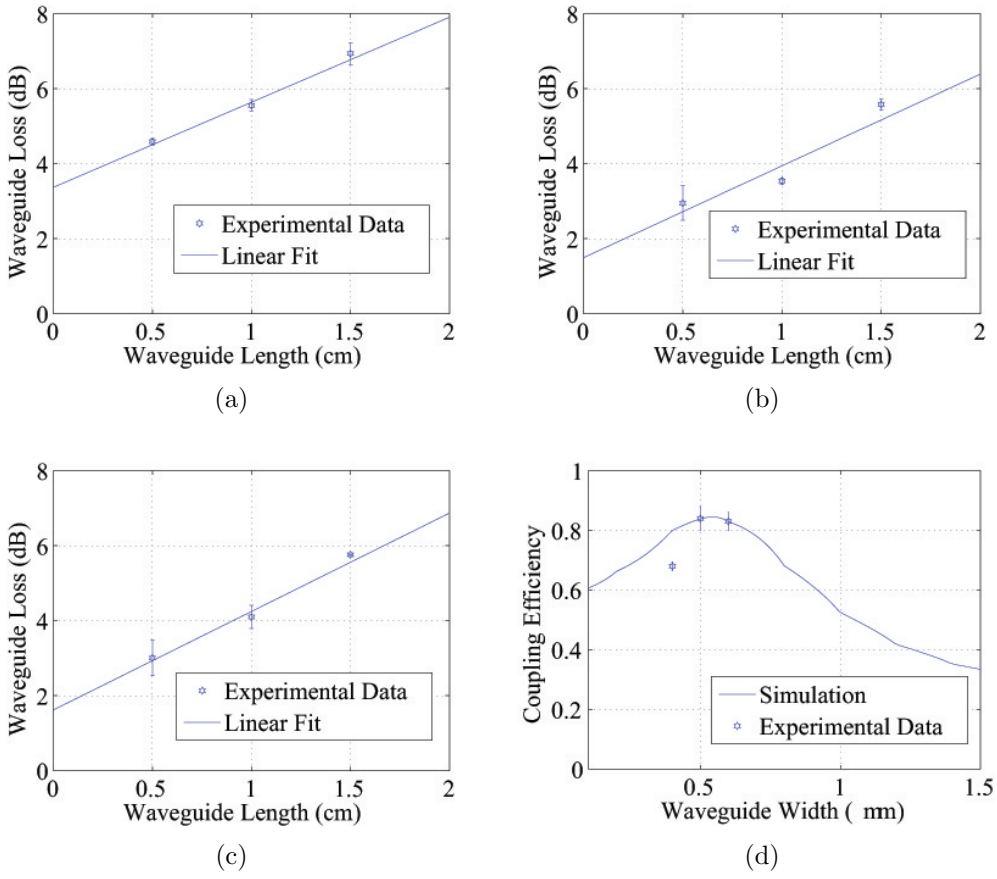

Figure 9.3: Coupling efficiencies between 100 nm thick Si_3N_4 waveguides and SMF28 fibers, measured at the wavelength of 1550 nm. (a) width of Si_3N_4 is 400nm. (b) width of Si_3N_4 is 500nm. (c) width of Si_3N_4 is 600nm. (d) comparison between the simulation and the experimental coupling efficiencies.

Table 9.1: Average coupling efficiencies between 100 nm thick Si_3N_4 waveguides and SMF28 fibers, measured at the wavelength of 1550 nm

Waveguide dimension	Average coupling efficiency
100 nm × 400nm	(68 ± 1.5) %
100 nm × 500nm	(84 ± 4) %
100 nm × 600nm	(83 ± 3) %

9.2.2 Coupling Efficiency with SM1500G80 Fibers

Similarly, to examine the coupling efficiencies between Si_3N_4 waveguides and SM1500G80 fibers, Si_3N_4 waveguides with a fixed thickness of 100 nm and three different widths (600 nm, 700 nm and 800 nm) are fabricated and tested, as shown in Fig. 9.4. These coupling efficiencies were measured at the wavelength of 1500 nm. The coupling efficiencies are found to be -0.5465 dB (88%), -0.3688 dB (92%) and -0.702 dB (85%), and the comparison between the simulation and the experimental data is also shown in Fig. 9.4(d). The propagation losses in both experiments are found to be about 2-3 dB/cm. These losses are not only caused by the scattering loss from the surface roughness, but also due to the absorption losses due to H in Si_3N_4 and in SiO_2 [31] [32]. In a future paper, we will present our effort to significantly reduce these propagation losses using high temperature thermal annealing process. Moreover, Table 9.3 shows the average coupling efficiencies with 68 % confidence intervals as well. These are by far the highest coupling efficiencies obtained for Si_3N_4-core waveguide on the silica-on-silicon platform. At the same time, it is demonstrated both theoretically and experimentally that high coupling efficiency can be achieved with a relatively simple design.

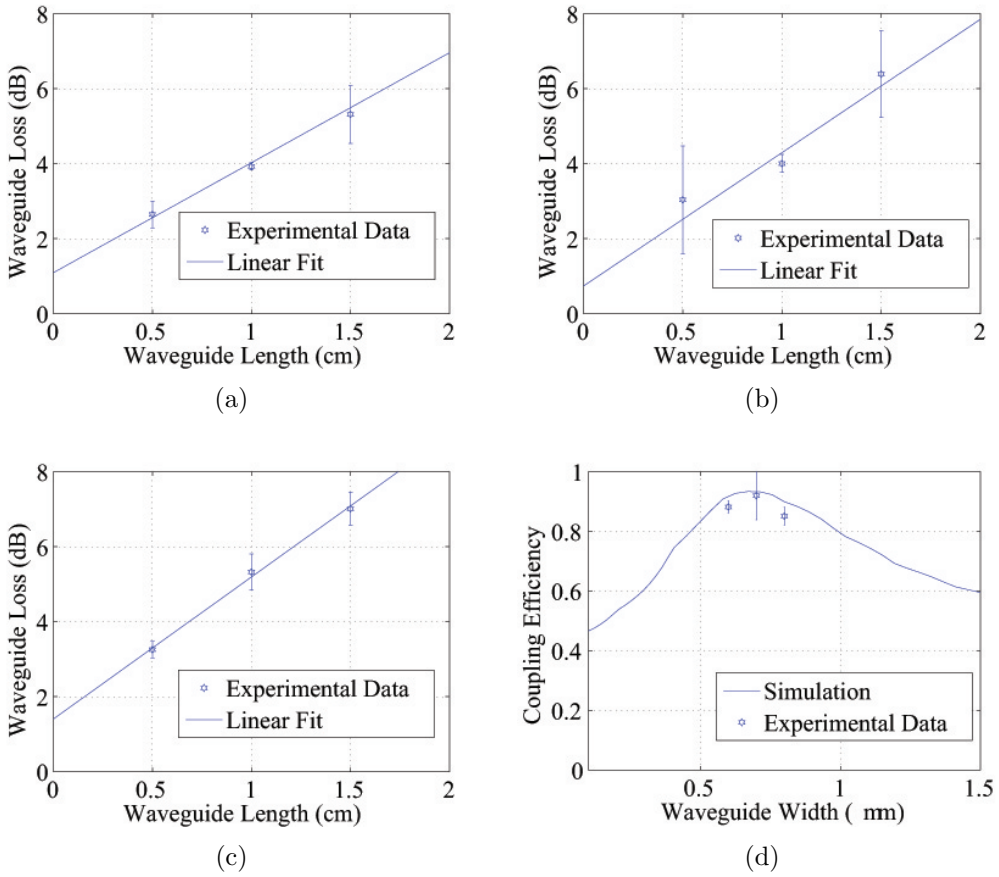

Figure 9.4: Coupling efficiencies between 100 nm thick Si_3N_4 waveguides and SM1500G80 fibers, measured at the wavelength of 1550 nm. (a) width of Si_3N_4 is 600nm. (b) width of Si_3N_4 is 700nm. (c) width of Si_3N_4 is 800nm. (d) comparison between the simulation and the experimental coupling efficiencies.

Table 9.2: Average coupling efficiencies between 100 nm thick Si_3N_4 waveguides and SM1500G80 fibers, measured at the wavelength of 1550 nm

Waveguide dimension	Average coupling efficiency
100 nm × 600nm	(88 ± 2) %
100 nm × 700nm	(92 ± 8) %
100 nm × 800nm	(85 ± 3) %

9.2.3 Coupling Efficiency with UHNA3 Fibers

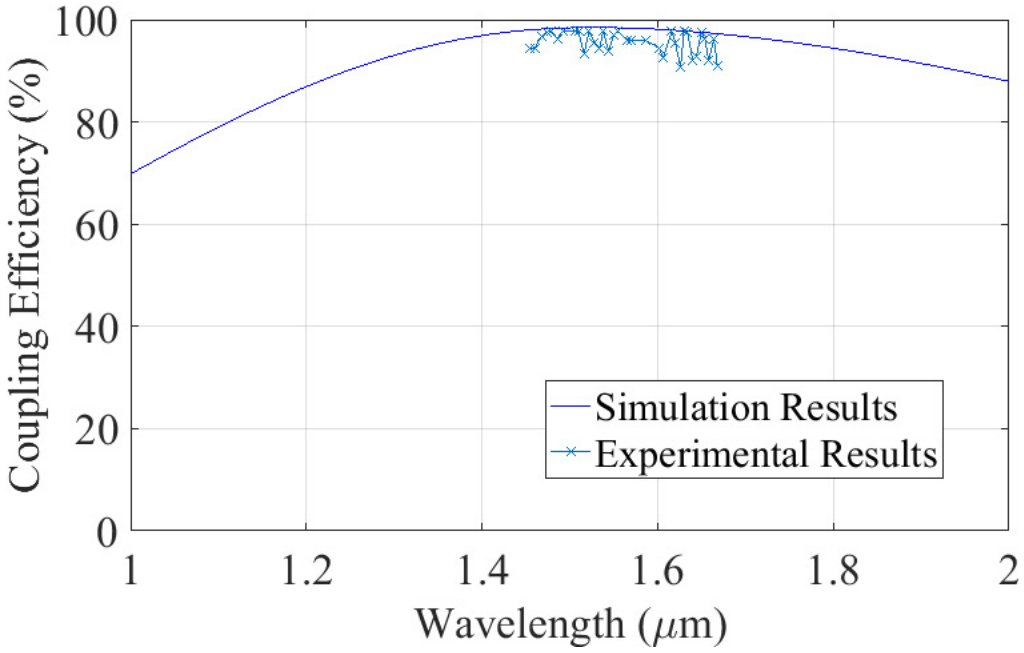

Figure 9.5: Theoretical and experimental coupling efficiency as a function of wavelength between the UHNA3 fiber and the 100 nm × 900 nm Si_3N_4 waveguide, which describes how much light is coupled from the UHNA3 fiber to the 100 nm × 900 nm Si_3N_4 waveguide. The experimental coupling efficiency at 1550 nm is 96 %, and is > 90 % for the entire spectrum from 1450 nm to 1650 nm.

Fig. 9.5 shows the experimental coupling efficiency as a function of wavelength between the UHNA3 fiber and the 100 nm thick × 900 nm wide Si_3N_4 waveguide. The wavelength dependence of the coupler is measured from 1450 nm to 1650 nm. The experimental coupling efficiency is 96 % at the central design wavelength of 1550 nm, and is > 90 % for the entire spectral range from 1450 nm to 1650 nm. These results nicely agree with the simulation data. The wobble in the measured coupling efficiency is due to the fact that UHNA3 fiber is not a pure Polarization-Maintaining (PM) fiber, so although the fiber is tuned to a pure TE mode at one

wavelength, at other wavelengths there will be some amount of TM mode that will appear. A further discussion about the coupling efficiency versus both TE and TM modes will be given in the next section.

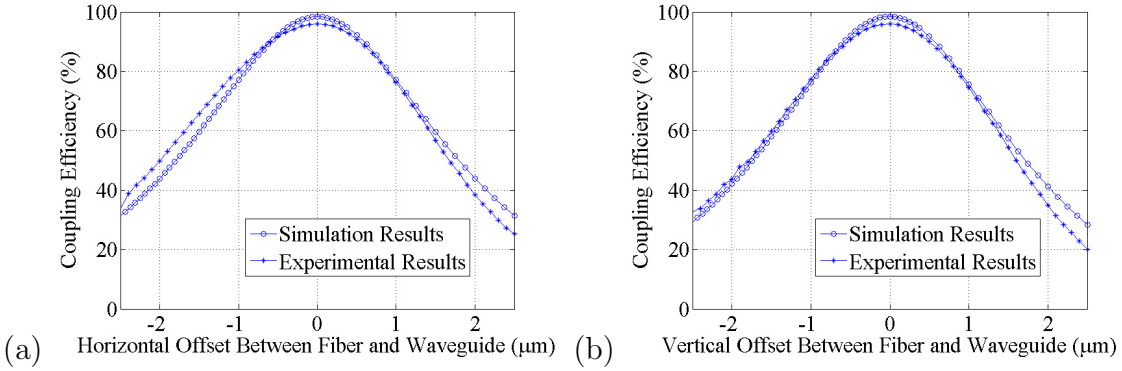

Figure 9.6: Theoretical and experimental 3-dB width (FWHM) alignment tolerance between the UHNA3 fiber and the 100 nm × 900 nm Si_3N_4 waveguide. (a) horizontal alignment tolerance. (b) vertical alignment tolerance.

Table 9.3: Theoretical and experimental alignment tolerances between the UHNA3 fiber and the 100 nm × 900 nm Si_3N_4/SiO_2 waveguide

	Simulation Data	Experimental Data
Horizontal Direction	3.6 μm	3.8 μm
Vertical Direction	3.5 μm	3.6 μm

We also obtained the alignment tolerances between the fiber and the waveguide coupler. We first optimized the coupling for maximum transmission and then offset the fiber position both horizontally and vertically. Fig. 9.6 shows the theoretical and experimental coupling efficiency versus the offset, and Table. 9.3 lists the experimental alignment tolerances both in the horizontal and the vertical direction. The experimental alignment tolerances are 3.8 μm horizontally and 3.6 μm vertically,

agreeing well with the theoretical values of 3.6 μm and 3.5 μm respectively.

Chapter 10: Discussions & Further Improvements

10.1 Coupling Efficiency vs Polarization

In many applications, the waveguide device mainly operates in the fundamental TE mode, which has the highest effective index, the smallest mode size suitable for integration and also the lowest propagation loss. However, sometimes an integrated waveguide device needs to work specifically in the TM mode, or in both the TE and the TM modes. In these cases, a polarization-insensitive coupling efficiency is desired.

Table 10.1: Mode sizes ($\frac{1}{e^2}$ intensity width) of both TE and TM modes for three Si_3N_4/SiO_2 waveguide geometries

	TE Mode at 1550 nm		TM Mode at 1550 nm	
	horizontal	vertical	horizontal	vertical
100 nm × 900 nm	1.89 μm	1.67 μm	5.71 μm	4.55 μm
200 nm × 450 nm	1.56 μm	1.46 μm	2.75 μm	2.71 μm
300 nm × 330 nm	1.71 μm	1.66 μm	1.66 μm	1.70 μm

Fig. 10.1 gives the comparison between the TE mode and the TM mode for the theoretical coupling efficiency, for the Si_3N_4/SiO_2 waveguide for the three dif-

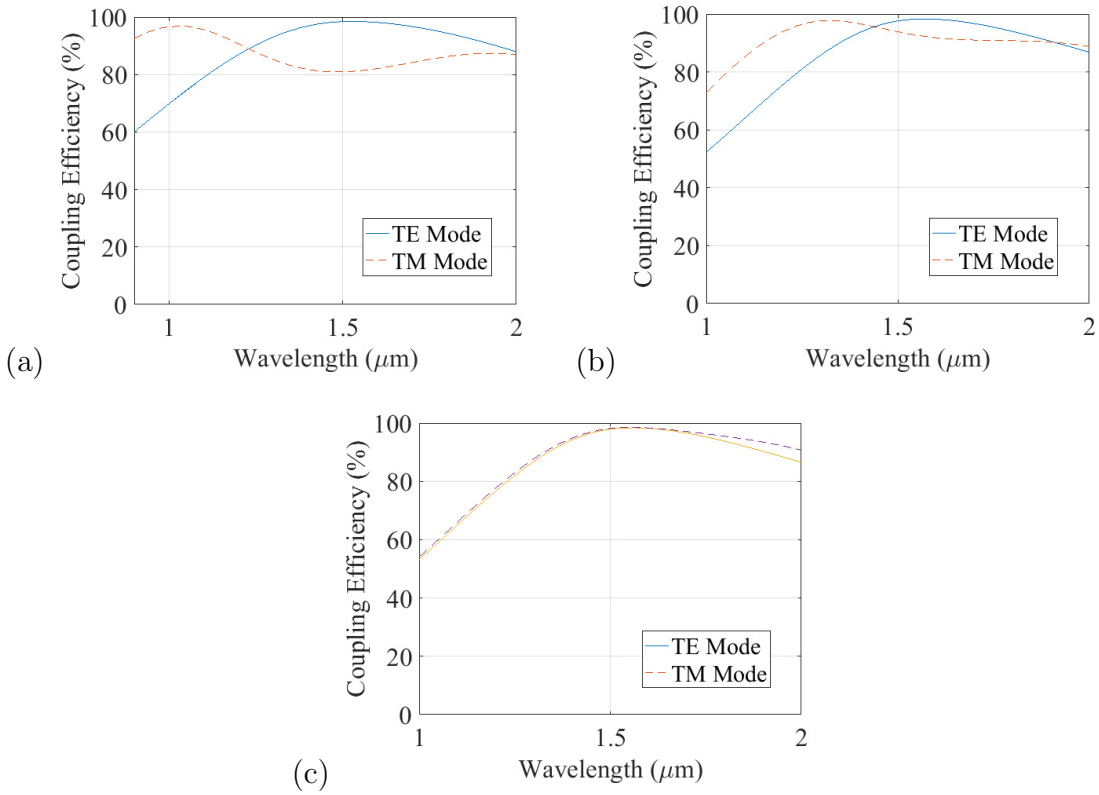

Figure 10.1: Theoretical coupling efficiency versus the operating wavelength between the UHNA3 fiber and the Si_3N_4/SiO_2 waveguide for both the TE mode and the TM mode. (a) 100 nm $\times$ 900 nm Si_3N_4 waveguide. (b) 200 nm $\times$ 450 nm Si_3N_4 waveguide. (c) 300 nm $\times$ 330 nm Si_3N_4 waveguide.

ferent geometries: 100 nm × 900 nm, 200 nm × 450 nm, and 300 nm × 330 nm. The difference of the coupling efficiency between the TE mode and the TM mode is obvious for the 100 nm × 900 nm Si_3N_4 waveguide, and their performance are very similar for the Si_3N_4 with 300 nm × 330 nm geometry. The reason for this behavior lies in the aspect-ratio of the waveguide geometry, which is defined as the ratio of the waveguide width divided by the waveguide thickness. Waveguides with aspect-ratios close to unity have square-like cross-sections. It means that the TE mode has a similar mode profile as the TM mode, just with a 90 degree rotational difference. Therefore, a 300 nm × 330 nm Si_3N_4 waveguide is preferred if polarization insensitivity is the priority, and a 100 nm × 900 nm Si_3N_4 waveguide is more desirable if wavelength insensitivity is desired for the fundamental TE mode. Table 10.1 lists the mode sizes for the three waveguide geometries both horizontally and vertically. The polarization-insensitive operation of the waveguide coupler will be studied in future work.

10.2 Applications

The waveguide coupler described here exhibits important properties, such as ease of cleaving, high coupling efficiency and ultra-broadband wavelength insensitivity, which make it attractive for a number of applications, including integrated optical filters, Wavelength-Division Multiplexing (WDM) systems, quantum information processing, and other optical network applications. In one of our recent work, the waveguide coupler with a thickness of 100 nm is used in a Complex Waveguide

Bragg Grating (CWBG) as a complex optical filter, which removes as many as 20 randomly-distributed spectral lines in the transmission spectrum [10]. According to the theoretical algorithm, the CWBG has a Si_3N_4 layer with a constant thickness of 100 nm everywhere, and it works on the TE mode for a broad spectrum between 1500 nm and 1550 nm. All these requirements make the 100 nm thick Si_3N_4 waveguide coupler an ideal coupler for the CWBG. In our design, the CWBG utilizes two 100 nm thick Si_3N_4 waveguide on both ends for maximum coupling efficiency, and has an aperiodic complex waveguide grating structure written on Part III according to Fig. 8.1.

Another potential application of the waveguide coupler is for Arrayed Waveguide Gratings (AWG). An AWG is used as an optical (de)multiplexers in wavelength division multiplexed (WDM) systems. Designed to operate over a broad-band spectrum, the input of the AWG is generally an optical fiber containing light of different wavelengths, and at its output the wavelengths are dispersed and come out from different output channels. In a recent paper, an AWG has been realized on the silica-on-silicon platform with 50 nm thick Si_3N_4 waveguide, with the benefit of ultra low propagation loss [58]. The coupling efficiency of the AWG, however, was not optimized fully at 1550 nm. The design and concept of the wavelength-insensitive high coupling efficiency couplers described in this paper could be easily added to the AWGs for better throughput. As a proof of demonstration, we have also successfully combined the same type of coupler presented in this paper with a new type of AWG, which is specifically designed for astronomical observations [59].

Chapter 11: Conclusions

In this paper, the concept of a fiber-to-waveguide coupler based on a Si_3N_4/SiO_2 waveguide is theoretically presented and experimentally analyzed. The waveguide coupler features a high coupling efficiency of 98 % in theory and 96 % in our experiment performed at a wavelength of 1550 nm, and $>$ 90 % experimental coupling efficiency in the spectral range from 1450 nm to 1650 nm. It also features ease of end-facet cleaving position accuracy and large fiber-to-waveguide alignment tolerances both vertically and horizontally. The horizontal and vertical alignment tolerances are 3.8 μm and 3.6 μm experimentally, compared to the theoretical values of 3.6 μm and 3.5 μm respectively. This type of waveguide coupler is particularly useful in applications such as integrated optical filters, WDM systems, quantum information processing. All the experimental results agrees well with the theoretical values. While this paper focuses on the coupling mechanism implemented using the Si_3N_4/SiO_2 waveguide, the good agreement between the measured and predicted values suggests that the same concept and approach can be applied to other platforms, material systems, and fiber types. Future work will include a detailed study of the polarization-insensitive waveguide couplers, high coupling efficiency to other types of single-mode fibers, and a scattering loss optimization of the adiabatic

mode-converter.

11.1 Publications

Journal Papers

• **Tiecheng Zhu**, Yiwen Hu, Pradip Gatkine, Sylvain Veilleux, Joss Bland-Hawthorn, and Mario Dagenais. "Arbitrary on-chip optical filter using complex waveguide Bragg gratings." Applied Physics Letters 108, no. 10 (2016): 101104.

• **Tiecheng Zhu**, Yi-Wen Hu, Pradip Gatkine, Sylvain Veilleux, Joss Bland-Hawthorn, and Mario Dagenais. "Ultra-broadband High Coupling Efficiency Fiber-to-Waveguide Coupler Using Si3N4/SiO2 Waveguides On Silicon." IEEE Photonics Journal, vol. 8, no. 5, pp. 1-12, Oct. 2016.

• Pradip Gatkine, Sylvain Veilleux, Yiwen Hu, **Tiecheng Zhu**, Yang Meng, Joss Bland-Hawthorn, and Mario Dagenais. "Development of high resolution arrayed waveguide grating spectrometers for astronomical applications: first results." arXiv preprint arXiv:1606.02730 (2016).

Conference Papers

• (**Invited**) **Tiecheng Zhu**, Sylvain Veilleux, and Mario Dagenais, "Si3N4/SiO2 on Si Nanophotonics for Arbitrary Optical Filters and High Efficiency Couplers." Optical Society of America (OSA) Photonics North, 2016

• **Tiecheng Zhu**, Sylvain Veilleux, Joss Bland-Hawthorn, and Mario Dagenais. "Ultra-broadband High Coupling Efficiency Using a Si 3 N 4/SiO

2 waveguide on silicon." Photonics Society Summer Topical Meeting Series (SUM), 2016 IEEE, pp. 92-93. IEEE, 2016.

• **Tiecheng Zhu,** Sylvain Veilleux, Joss Bland-Hawthorn, and Mario Dagenais. "Complex Waveguide Bragg Gratings For arbitrary spectral filtering." Photonics Society Summer Topical Meeting Series (SUM), 2016 IEEE, pp. 211-212. IEEE, 2016.

• (**Invite**) **Tiecheng Zhu**, Sylvain Veilleux, Joss Bland-Hawthorn, and Mario Dagenais. "Ultra high coupling efficiency from a single mode fiber to a high index contrast on-chip waveguide and complex waveguide Bragg gratings for spectral filtering." 2015 IEEE Summer Topicals Meeting Series (SUM), pp. 19-20. IEEE, 2015.

11.2 Appendix A

In this part of the thesis, I will show my Matlab programs used for Layer Peeling/Adding algorithm. In this example, I showed the detailed steps on designing a 20-notch filter.

11.2.1 Main Matlab Program for Layer Peeling/Adding algorithm

```
% This is the main program for the LP/LA algorithm

% Input: a target reflectivity spectrum (it can be converted
    from either a reflection or a transmission spectrum)
% Output: rho/q/effective_index (these three parameters are
    convertible to each other) of the corresponding grating

% In this example, I will demonstrate the LP/LA for the
    synthesis of a grating with 20 prescribed random notches.

% Meanings of All These Various Parameters
% n_0 (no unit): the average effective index (for example,
    n_0 is calculated from FimmWave using a 100nm * 1um
    waveguide)
% lambda_center (unit: m): the central wavelength used in
    the algorithm, which is set to be 1550 nm (1550e-9 m) in
    our case.
% Lambda (unit: m): period of the grating
% delta_omega (unit: m^-1): wavelength detuning range of the
    spectrum used for the algorithm. If we want to filter
    between 1500 nm and 1600 nm, then delta_omega has to
    cover at least from 1500 nm to 1600 nm.
% delta_z: length of each discretized segment of the grating
% M: number of wavelengths sampled in the whole spectrum
    range (Note: M>= N)
% N: number of discretized segments in the grating
% L: overall length of the grating (for example, delta_z =
    10 um, N = 2500, then L = 2500 * 10um = 2.5 cm)
% Hann_length: the number of points chosen for the Hanning
    window function (the Hanning window is multiplied to the
    impulse function to force it
% become zero beyong certain ranges)
```

```
% layer_array: the array of grating layers seen from delta_z
    , used for plotting the results later
% N_divided: we divide each delta_z into even smaller pieces
    , and each piece will have its a constant effective index
    , in this case, N_divided = 100;
% min_layer_with_const_n_eff: the length of the minimum
    segment with a constant, in this case,
    min_layer_with_const_n_eff = 100 nm
% layer_array_new: the new array of grating layers

% delta_interval: wavelength detuning separation between two
     neighboring wavelengths
% delta: detuning of all the wavelengths
% delta_center: wavenumber of the central wavelength
% lambda: all the wavelengths
% Note: the LP/LA operates in both time domain and frequency
     domain, so delta (which is the
% wavelength detuning) should be a equal-distance, not
    lambda (wavelength).

% polarization: 'TE' or 'TM', not actually used in this
    example, because we are manually entering the effective
    index of the mode
% lambda_min: minimum wavelength
% lambda_max: maximum wavelength
% lambda_dip: positions of these 20 randomly-distributed
    notches
% T_amp_dB: oroginal suppression ratios of these 20 notches,
     note that this value can be enhanced by the trick in the
     algorithm
% dip_width: oroginal 3-dB width of these 20 notches, note
    that this value can be enhanced by the trick in the
    algorithm



%%
% clear all the parameters and the command window
clear;
clc;

% Set the parameters of the LP/LA
% For different applications, these parameters will need to
    be adjusted and optimized correspondingly
```

```
n_0 =  1.454287  ;
lambda_center = 1550e-9;
Lambda = lambda_center / 2 / n_0 ;
delta_omega = 1e5 * pi;
delta_z = pi / delta_omega; % Very important relation
   according to Fourier Transform

N = 2500;
L = delta_z * N;
M =  4 * N;
Hann_length = N;

layer_array = (delta_z:delta_z:L);
N_divided = 100;
min_layer_with_const_n_eff = delta_z / N_divided;
layer_array_new = (min_layer_with_const_n_eff:
   min_layer_with_const_n_eff:L);

delta_interval = delta_omega / (M - 1);
delta = (- delta_omega / 2 : delta_interval : delta_omega /
   2);
delta_center = 2*pi * n_0 / lambda_center;
lambda = 2*pi * n_0 ./ (delta + delta_center);
polarization = 'TE';

lambda_min = min(lambda);
lambda_max = max(lambda);
lambda_dip = [1532 1533 1535 1536 1537 1538 1540 1541 1542
   1544 ...
              1545 1546 1547 1548 1549 1550 1554 1556 1557
                 1558]*1e-9;
T_amp_dB = 30 * ones(1, length(lambda_dip));
dip_width = 0.08e-9 * ones(1, length(lambda_dip));



%%
% first, we get the lambda and delta for all the wavelengths
    correctly
% In the derivation of our LP/LA algorithm, wavelength
   detuning is an equal-distance array. On the other hand,
   lambda
% is not an equal-distance array (although neighboring
   separation is more or less the same).
```

```
% Otherwise the results will be wrong!!
[ lambda_1, delta_1, r_target ] = Spectrum_Initialize(n_0,
    lambda_min, lambda_max, M, lambda_dip, T_amp_dB,
    dip_width);

% Discrete Fourier Transform and Hanning Window Procese
% To get a realiable spectrum for a physically-achievable
    grating
h = fftshift( fft( ifftshift(r_target) ) ) / M;
[ h_hann_and_shifted ] = Hann_and_Shift_Even_h( h,
    Hann_length );
r_initial = fftshift( ifft(ifftshift(h_hann_and_shifted)) )
    * M;


% Layer Peeling Algorithm
[ rho, q ] = Layer_Peeling( length(lambda), N, r_initial,
    delta, delta_z );

% If we want even higher suppression ratios, we may just
    increase q and rho proportionally to get larger
    suppression ratios
% Note the spectral positions of these notches are still the
    same, great!!
rho = rho * 5;
q = q * 5;

% Layer Adding Algorithm
[ r_reconstructed ] = Layer_Adding( length(lambda), N, rho,
    delta, delta_z );



%%
% Plot some of the results for verification

% Plot the absolute value of q
subplot(4,1,1);
plot(layer_array, abs(q) );
grid on;
xlabel('Grating Position');
ylabel('Abs of q ');

% Plot the angle of q / Pi
subplot(4,1,2);
```

```
plot(layer_array, angle(q)/pi );
grid on;
xlabel('Grating Position');
ylabel('Angle of q / pi');

% Plot the target transmission spectrum
subplot(4,1,3);
plot(lambda, 10*log10( (1-(abs(r_target)).^2) ) );
xlabel('Wavelength / nm');
ylabel('abs(R_target)');
grid on;
axis([1530e-9 1560e-9 -80    10]);

% Plot the reconstructed spectrum
subplot(4,1,4);
plot(lambda, 10*log10( (1-(abs(r_reconstructed)).^2)) );
xlabel('Wavelength / nm');
ylabel('R layer adding');
axis([1530e-9 1560e-9 -80    10]);
grid on;



%%

% Up to now, we have obtained values for rho and q
% Next, we will calculate the effective index distribution

% Some more explanation: for each delta_z (10 um in this
    example), there
% will be a constant rho and a constant q (rho and q
    proportional to one another).
% But each delta_z will a sinusoidally-varying effective
    index variation, and the intensity of this variation is q
    .
% This is why previously we divide each delta_z into another
     100 smaller
% pieces (100 nm each), and each small piece has its own
    constant effective index.

% The effective index will be written into a .txt file shown
     below, which
% can be used for further index-mapping and fabrication
    purposes
```

```
delta_n_ac = zeros(1,N);
delta_n_dc = zeros(1,N);
theta_n = zeros(1,N);
n_actual = zeros(1,length(layer_array_new));
index_file = fopen('index_file.txt','w');

for i1 = 1: N
    delta_n_ac(i1) = lambda_center * abs(q(i1)) / pi;
    theta_n(i1) = angle(q(i1)) - pi/2;;
    for i2 = 1: N_divided
        z = layer_array_new( (i1 - 1)*N_divided + i2 );
        n_actual((i1 - 1)*N_divided + i2) = n_0 + delta_n_ac
            (i1) * cos( 2*pi / Lambda * z + theta_n(i1) );
        fprintf(index_file,'%20.12f        %20.6f\n',[
            min_layer_with_const_n_eff  n_actual((i1 - 1)*
            N_divided + i2)]);
    end
end
fclose(index_file);
```

11.2.2 Matlab Function for Spectrum Initialization

Next, let me show the program used for generating the initial target spectrum. In this example, a spectrum is generated with 20 notches. This part of the program will need high customization if the user is handling different applications.

```
% This is the function for spectrum initialization
% This part should be highly customized for different
    applications
% In this example, we put 20 notches in the spectrum, and
    generate a target reflectivity spectrum

% Meanings of All These Various Parameters
% n_0 (no unit): the average effective index (for example,
    n_0 is calculated from FimmWave using a 100nm * 1um
    waveguide)
% M: number of wavelengths sampled in the whole spectrum
    range
% lambda_min: minimum wavelength
% lambda_max: maximum wavelength
% delta_min: minimum wavelength detuning (this corresponds
    to lambda_max)
% delta_max: maximum wavelength detuning (this corresponds
    to lambda_min)

% delta_shift: shift of actual wavelength detuning (because
    in Discrete Fourier Transform, delta is from [-x, x]
    centered at 0)
% lambda_dip: positions of these 20 randomly-distributed
    notches
% T_amp_dB: oroginal suppression ratios of these 20 notches,
     note that this value can be enhanced by the trick in the
     algorithm
% dip_width: oroginal 3-dB width of these 20 notches, note
    that this value can be enhanced by the trick in the
    algorithm

% delta_interval: wavelength detuning separation between two
     neighboring wavelengths
% delta_omega (unit: m^-1): wavelength detuning range of the
     spectrum used for the algorithm. If we want to filter
    between 1500 nm and 1600 nm, then delta_omega has to
    cover at least from 1500 nm to 1600 nm.
% delta: detuning of all the wavelengths
% lambda: all the wavelengths
```

```
% T_amp: transmission values in percentage
% R_amp: reflection values in percentage
% no_lambda_dip: number of notches, in this case,
    no_lambda_dip = 20
% R_total: overall reflection spectrum
% r_target: overall reflectivity spectrum



function [ lambda, delta,r_target ] = Spectrum_Initialize(
    n_0, lambda_min, lambda_max, M, lambda_dip , T_amp_dB,
    dip_width)

% Note that r_target, lambda, delta is revers displayed from
     1600nm to 1500nm

delta_min = 2*pi * n_0 / lambda_max;
delta_max = 2*pi * n_0/ lambda_min;
delta_shift = (delta_min + delta_max ) / 2;
delta_omega = delta_max - delta_min;
delta_interval = delta_omega / (M - 1);
delta = [- delta_omega / 2 : delta_interval : delta_omega /
    2];
lambda = 2*pi * n_0 ./ (delta + delta_shift);

T_amp = 10.^-(T_amp_dB / 10);
R_amp = 1 - T_amp;
no_lambda_dip = length(lambda_dip);
R_total = zeros(1,M);


for n = 1:no_lambda_dip
     R(n,:) = R_amp(n) ./ cosh( (2*(lambda - lambda_dip(n) )
         / dip_width(n)).^4 );
%      R(n,:) = R_amp(n) * exp( -2 * ( 2 * (lambda -
    lambda_dip(n) ) /  dip_width(n) ).^20 );
     R_total = R_total + R(n,:);
end

r_target = R_total.^0.5;

end
```

11.2.3 Matlab Function for Obtaining a Realizable Spectrum

```
% This is the function for achieving a realizable spectrum

% A realization spectrum has the following property: its
    impulse response
% h(t) will always be zero if t <= 0. h(t) is non-zero only
    when t > 0.
% The reason is for a physically-realiable grating, the
% impulse hasn't seen the grating yet when t <= 0.

% Meanings of All These Various Parameters
% h: original impulse response, which needs to be treated
% Hann_length: size of the Hanning window
% Hann_array: the hanning window
% h_length: number of samples in the original impulse
    response
% Hann_length_half: half of the Hann_length
% h_length_half: half of the h_length
% length_shift: difference between Hann_length_half and
    h_length_half
% h_hann_and_shifted: realizable impulse response, which
    starts only at t > 0


function [ h_hann_and_shifted ] = Hann_and_Shift_Even_h( h,
    Hann_length )

%Now use the Hanning window
Hann_array = hann(Hann_length);
h_length = length(h);

Hann_length_half = Hann_length /2;
h_length_half = h_length /2;
length_shift = (h_length - Hann_length)/2;
h_hann_and_shifted= zeros(1,h_length);

for j1 = 1:Hann_length
    h_hann_and_shifted(j1 + h_length_half ) = Hann_array(j1)
        * h(j1 + length_shift ) ;
end

end
```

11.2.4 Matlab Function for the Layer Peeling Step

```
% This is the function for Layer Peeling
% It calculates rho and q for all discretized segments in
    the grating

% Meanings of All These Various Parameters
% rho (no unit): complex reflection coefficient
% q (unit: m^-1): complex coupling coefficient
% M: number of wavelengths sampled in the whole spectrum
    range (Note: M >= N)
% N: number of discretized segments in the grating
% r_initial: intitial target reflectivity spectrum which is
    realizable
% delta: detuning of all the wavelengths
% delta_z: length of each discretized segment of the grating
% r: in the iterative for-loop, r repeseent the reflectivity
    spectrum seen from the current layer
% r_new: in the iterative for-loop, r_new repeseent the
    reflectivity spectrum seen from the next layer


function [ rho, q ] = Layer_Peeling( M, N, r_initial, delta,
    delta_z )

    rho = zeros(1,N);
    q = zeros(1,N);
    r = zeros(1,M);
    r_new = zeros(1,M);

    r = r_initial;

    %calculate the complex coupling coefficient
    for n = 1:N
        rho(n) = mean( r );
        r_new = exp(-i*2*(delta)*delta_z) .* ( r - rho(n) )
            ./ ( 1 - rho(n)' * r );
        q(n) = - 1/delta_z*atanh( abs(rho(n)) ) * ( rho(n) )
            ' / abs(rho(n)) ;
        r = r_new;
    end
end
```

11.2.5 Matlab Function for the Layer Adding Step

```
% This is the function for Layer Adding
% It calculates the reconstructued spectrum from the values
    of rho (which are equavilent to the effective index)

% Meanings of All These Various Parameters
% rho (no unit): complex reflection coefficient
% M: number of wavelengths sampled in the whole spectrum
    range (Note: M>= N)
% N: number of discretized segments in the grating
% delta: detuning of all the wavelengths
% delta_z: length of each discretized segment of the grating
% r: in the iterative for-loop, r repeseent the reflectivity
     spectrum seen from the (i+1)th layer
% r_new: in the iterative for-loop, r_new repeseent the
    reflectivity spectrum seen from the ith layer

% Layer Adding operates from the last layer of the grating
    to the first
% layer of the grating, which is why we call it "Adding".
% The reflection spectrum seen from the last layer is
    basically zero for
% all wavelengths, because all the output light will be
    transmitted without any
% reflection after the whole grating.



function [ r_reconstructed ] = Layer_Adding( M, N, rho,
    delta, delta_z )

    r = zeros(1,M);
    r_new = zeros(1,M);
    for j1 = 1: N
        %the starting layer j2
        j2 = N + 2 - j1;
        r_new = ( r + exp(-i*2*(delta)*delta_z) * rho(j2 -
            1) )./(exp(-i*2*(delta)*delta_z) + r * (rho(j2 -
            1))');
        r = r_new;
    end
    r_reconstructed = r_new;
end
```

Bibliography

[1] Kenneth O Hill, B Malo, F Bilodeau, DC Johnson, and J Albert. Bragg gratings fabricated in monomode photosensitive optical fiber by uv exposure through a phase mask. *Applied Physics Letters*, 62(10):1035–1037, 1993.

[2] Andreas Othonos. Fiber bragg gratings. *Review of Scientific Instruments*, 68(12):4309–4341, 1997.

[3] Raman Kashyap. *Fiber bragg gratings*. Academic press, 1999.

[4] Andreas Othonos and Kyriacos Kalli. *Fiber Bragg gratings: fundamentals and applications in telecommunications and sensing*. Artech House, 1999.

[5] Thomas Edward Murphy, Jeffrey Todd Hastings, and Henry I Smith. Fabrication and characterization of narrow-band Bragg-reflection filters in silicon-on-insulator ridge waveguides. *Journal of Lightwave Technology*, 19(12):1938, 2001.

[6] Graham D Marshall, Martin Ams, and Michael J Withford. Direct laser written waveguide-bragg gratings in bulk fused silica. *Optics Letters*, 31(18):2690–2691, 2006.

[7] Xu Wang, Wei Shi, Han Yun, Samantha Grist, Nicolas AF Jaeger, and Lukas Chrostowski. Narrow-band waveguide bragg gratings on soi wafers with cmos-compatible fabrication process. *Optics Express*, 20(14):15547–15558, 2012.

[8] J Bland-Hawthorn, A Buryak, and K Kolossovski. Optimization algorithm for ultrabroadband multichannel aperiodic fiber Bragg grating filters. *JOSA A*, 25(1):153–158, 2008.

[9] P Rousselot, C Lidman, J-G Cuby, G Moreels, and G Monnet. Night-sky spectral atlas of OH emission lines in the near-infrared. *Astronomy and Astrophysics*, 354:1134–1150, 2000.

[10] Tiecheng Zhu, Yiwen Hu, Pradip Gatkine, Sylvain Veilleux, Joss Bland-Hawthorn, and Mario Dagenais. Arbitrary on-chip optical filter using complex waveguide bragg gratings. *Applied Physics Letters*, 108(10):101104, 2016.

[11] Bruno Badoil, Fabien Lemarchand, Michel Cathelinaud, and Michel Lequime. Interest of broadband optical monitoring for thin-film filter manufacturing. *Applied Optics*, 46(20):4294–4303, 2007.

[12] J Bland-Hawthorn, SC Ellis, SG Leon-Saval, R Haynes, MM Roth, H-G Löhmannsröben, AJ Horton, J-G Cuby, Tim A Birks, JS Lawrence, et al. A complex multi-notch astronomical filter to suppress the bright infrared sky. *Nature Communications*, 2:581, 2011.

[13] SC Ellis, J Bland-Hawthorn, J Lawrence, AJ Horton, C Trinh, SG Leon-Saval, K Shortridge, J Bryant, S Case, M Colless, et al. Suppression of the near-infrared OH night-sky lines with fibre Bragg gratings–first results. *Monthly Notices of the Royal Astronomical Society*, 425(3):1682–1695, 2012.

[14] Christopher Q Trinh, Simon C Ellis, Joss Bland-Hawthorn, Anthony J Horton, Jon S Lawrence, and Sergio G Leon-Saval. The nature of the near-infrared interline sky background using fibre Bragg grating OH suppression. *Monthly Notices of the Royal Astronomical Society*, 432(4):3262–3277, 2013.

[15] Christopher Q Trinh, Simon C Ellis, Joss Bland-Hawthorn, Jon S Lawrence, Anthony J Horton, Sergio G Leon-Saval, Keith Shortridge, Julia Bryant, Scott Case, Matthew Colless, et al. GNOSIS: the first instrument to use fiber Bragg gratings for OH suppression. *The Astronomical Journal*, 145(2):51, 2013.

[16] Günter Steinmeyer. A review of ultrafast optics and optoelectronics. *Journal of Optics A: Pure and Applied Optics*, 5(1):R1, 2003.

[17] Ian W Frank, Yinan Zhang, and Marko Loncar. Nearly arbitrary on-chip optical filters for ultrafast pulse shaping. *Optics Express*, 22(19):22403–22410, 2014.

[18] Thomas F Krauss. Why do we need slow light? *Nature Photonics*, 2(8):448–450, 2008.

[19] Johannes Skaar, Ligang Wang, and Turan Erdogan. On the synthesis of fiber bragg gratings by layer peeling. *Quantum Electronics, IEEE Journal of*, 37(2):165–173, 2001.

[20] Ricardo Feced, Michalis N Zervas, and Miguel A Muriel. An efficient inverse scattering algorithm for the design of nonuniform fiber bragg gratings. *Quantum Electronics, IEEE Journal of*, 35(8):1105–1115, 1999.

[21] A Buryak, J Bland-Hawthorn, and V Steblina. Comparison of inverse scattering algorithms for designing ultrabroadband fibre bragg gratings. *Optics Express*, 17(3):1995–2004, 2009.

[22] Marie Verbist, Dries Van Thourhout, and Wim Bogaerts. Weak gratings in silicon-on-insulator for spectral filters based on volume holography. *Optics Letters*, 38(3):386–388, 2013.

[23] Marie Verbist, Wim Bogaerts, and Dries Van Thourhout. Design of weak 1-D Bragg grating filters in SOI waveguides using Volume Holography techniques. *Journal of Lightwave Technology*, 32(10):1915–1920, 2014.

[24] Johannes Skaar. *Synthesis and characterization of fiber Bragg gratings*. Citeseer, 2000.

[25] Turan Erdogan. Fiber grating spectra. *Journal of lightwave technology*, 15(8):1277–1294, 1997.

[26] Leon Poladian. Resonance mode expansions and exact solutions for nonuniform gratings. *Physical Review E*, 54(3):2963, 1996.

[27] Allan W Snyder and John Love. *Optical waveguide theory*. Springer Science & Business Media, 2012.

[28] Amnon Yariv and Pochi Yeh. *Photonics: optical electronics in modern communications (the oxford series in electrical and computer engineering)*. Oxford University Press, Inc., 2006.

[29] Johannes Skaar and Ole Henrik Waagaard. Design and characterization of finite-length fiber gratings. *IEEE Journal of Quantum Electronics*, 39(10):1238–1245, 2003.

[30] Geoffrey A Cranch and Gordon MH Flockhart. Tools for synthesising and characterising Bragg grating structures in optical fibres and waveguides. *Journal of Modern Optics*, 59(6):493–526, 2012.

[31] Charles H Henry, RF Kazarinov, HJ Lee, KJ Orlowsky, and LE Katz. Low loss Si_3N_4-SiO_2 optical waveguides on Si. *Applied Optics*, 26(13):2621–2624, 1987.

[32] G Grand, JP Jadot, H Denis, S Valette, A Fournier, and AM Grouillet. Low-loss PECVD silica channel waveguides for optical communications. *Electronics Letters*, 26(25):2135–2137, 1990.

[33] RR Thomson, Tim A Birks, SG Leon-Saval, AK Kar, and J Bland-Hawthorn. Ultrafast laser inscription of an integrated photonic lantern. *Optics Express*, 19(6):5698–5705, 2011.

[34] Izabela Spaleniak, Simon Gross, Nemanja Jovanovic, Robert J Williams, Jon S Lawrence, Michael J Ireland, and Michael J Withford. Multiband processing of multimode light: combining 3D photonic lanterns with waveguide Bragg gratings. *Laser & Photonics Reviews*, 8(1):L1–L5, 2014.

[35] Martijn JR Heck, Jared F Bauters, Michael L Davenport, Daryl T Spencer, and John E Bowers. Ultra-low loss waveguide platform and its integration with silicon photonics. *Laser & Photonics Reviews*, 8(5):667–686, 2014.

[36] David J Moss, Roberto Morandotti, Alexander L Gaeta, and Michal Lipson. New cmos-compatible platforms based on silicon nitride and hydex for nonlinear optics. *Nature Photonics*, 7(8):597–607, 2013.

[37] Hongchen Yu, Minghua Chen, Qiang Guo, Marcel Hoekman, Hongwei Chen, Arne Leinse, Rene G Heideman, Richard Mateman, Sigang Yang, and Shizhong Xie. Si 3 n 4-based integrated optical analog signal processor and its application in rf photonic frontend. *Photonics Journal, IEEE*, 7(5):1–9, 2015.

[38] Leimeng Zhuang, David Marpaung, Maurizio Burla, Willem Beeker, Arne Leinse, and Chris Roeloffzen. Low-loss, high-index-contrast si 3 n 4/sio 2 optical waveguides for optical delay lines in microwave photonics signal processing. *Optics Express*, 19(23):23162–23170, 2011.

[39] Vittorio MN Passaro, Mario La Notte, Benedetto Troia, Lorenzo Passaquindici, Francesco De Leonardis, and Giovanni Giannoccaro. Photonic structures based on slot waveguides for nanosensors: State of the art and future developments. *Int. J. Res. Rev. Appl. Sci*, 11(3):402–418, 2012.

[40] Günay Yurtsever, Boris Považay, Aneesh Alex, Behrooz Zabihian, Wolfgang Drexler, and Roel Baets. Photonic integrated mach-zehnder interferometer with an on-chip reference arm for optical coherence tomography. *Biomedical Optics Express*, 5(4):1050–1061, 2014.

[41] Jörn P Epping, Tim Hellwig, Marcel Hoekman, Richard Mateman, Arne Leinse, René G Heideman, Albert van Rees, Peter JM van der Slot, Chris J Lee, Carsten Fallnich, et al. On-chip visible-to-infrared supercontinuum generation with more than 495 thz spectral bandwidth. *Optics Express*, 23(15):19596–19604, 2015.

[42] Jared F Bauters, Martijn JR Heck, Demis John, Daoxin Dai, Ming-Chun Tien, Jonathon S Barton, Arne Leinse, René G Heideman, Daniel J Blumenthal, and John E Bowers. Ultra-low-loss high-aspect-ratio Si_3N_4 waveguides. *Optics Express*, 19(4):3163–3174, 2011.

[43] Jared F Bauters, Martijn JR Heck, Demis D John, Jonathon S Barton, Christiaan M Bruinink, Arne Leinse, René G Heideman, Daniel J Blumenthal, and John E Bowers. Planar waveguides with less than 0.1 db/m propagation loss fabricated with wafer bonding. *Optics Express*, 19(24):24090–24101, 2011.

[44] Christopher R Doerr, Long Chen, Young-Kai Chen, and Larry L Buhl. Wide bandwidth silicon nitride grating coupler. *IEEE Photonics Technology Letters*, 22(19):1461–1463, 2010.

[45] AZ Subramanian, Pieter Neutens, Ashim Dhakal, Roelof Jansen, Tom Claes, Xavier Rottenberg, Frédéric Peyskens, Shankar Selvaraja, Philippe Helin, Bert Dubois, et al. Low-loss singlemode PECVD silicon nitride photonic wire waveguides for 532–900 nm wavelength window fabricated within a CMOS pilot line. *Photonics Journal, IEEE*, 5(6):2202809–2202809, 2013.

[46] Huijuan Zhang, Chao Li, Xiaoguang Tu, Junfeng Song, Haifeng Zhou, Xianshu Luo, Ying Huang, Mingbin Yu, and GQ Lo. Efficient silicon nitride grating coupler with distributed Bragg reflectors. *Optics Express*, 22(18):21800–21805, 2014.

[47] Wesley D Sacher, Ying Huang, Liang Ding, Benjamin JF Taylor, Hasitha Jayatilleka, Guo-Qiang Lo, and Joyce KS Poon. Wide bandwidth and high coupling efficiency Si_3N_4-on-SOI dual-level grating coupler. *Optics Express*, 22(9):10938–10947, 2014.

[48] Wissem Sfar Zaoui, Andreas Kunze, Wolfgang Vogel, Manfred Berroth, Jörg Butschke, Florian Letzkus, and Joachim Burghartz. Bridging the gap between optical fibers and silicon photonic integrated circuits. *Optics Express*, 22(2):1277–1286, 2014.

[49] SH Tao, Junfeng Song, Qing Fang, Mingbin Yu, Guoqiang Lo, and Dimlee Kwong. Improving coupling efficiency of fiber-waveguide coupling with a double-tip coupler. *Optics Express*, 16(25):20803–20808, 2008.

[50] TG Tiecke, KP Nayak, JD Thompson, T Peyronel, NP de Leon, V Vuletić, and MD Lukin. Efficient fiber-optical interface for nanophotonic devices. *Optica*, 2(2):70–75, 2015.

[51] *FIMMWAVE/FIMMPROP by Photon Design Ltd., http://www.photond.com.*

[52] Application note nuapp-3: Uhna fiber efficient coupling to silicon waveguides. *Nufern Inc http://www.nufern.com/pam/optical_fibers/984/UHNA3/.*

[53] T Shoji, T Tsuchizawa, T Watanabe, K Yamada, and H Morita. Low loss mode size converter from 0.3 μm square si wire waveguides to singlemode fibres. *Electronics Letters*, 38(25):1669–1670, 2002.

[54] Jaime Cardenas, Carl B Poitras, Kevin Luke, Lian-Wee Luo, Paul Adrian Morton, and Michal Lipson. High coupling efficiency etched facet tapers in silicon waveguides. *IEEE Photonics Technol. Lett*, 26(23):2380–2382, 2014.

[55] Victor Nguyen, Trisha Montalbo, Christina Manolatou, Anu Agarwal, Chingyin Hong, John Yasaitis, LC Kimerling, and Jurgen Michel. Silicon-based highly-efficient fiber-to-waveguide coupler for high index contrast systems. *Applied Physics Letters*, 88(8):081112, 2006.

[56] Long Chen, Christopher R Doerr, Young-Kai Chen, and Tsung-Yang Liow. Low-Loss and Broadband Cantilever Couplers Between Standard Cleaved Fibers and High-Index-Contrast Si N or Si Waveguides. *Photonics Technology Letters, IEEE*, 22(23):1744–1746, 2010.

[57] F Ay and A Aydinli. Comparative investigation of hydrogen bonding in silicon based PECVD grown dielectrics for optical waveguides. *Optical Materials*, 26(1):33–46, 2004.

[58] Daoxin Dai, Zhi Wang, Jared F Bauters, M-C Tien, Martijn JR Heck, Daniel J Blumenthal, and John E Bowers. Low-loss Si_3N_4 arrayed-waveguide grating (de) multiplexer using nano-core optical waveguides. *Optics Express*, 19(15):14130–14136, 2011.

[59] Pradip Gatkine, Sylvain Veilleux, Yiwen Hu, Tiecheng Zhu, Yang Meng, Joss Bland-Hawthorn, and Mario Dagenais. Development of high-resolution arrayed waveguide grating spectrometers for astronomical applications: first results, 2016.